

STUDIES OF ARTERIAL BRANCHING  
IN MODELS USING FLOW  
BIREFRINGENCE

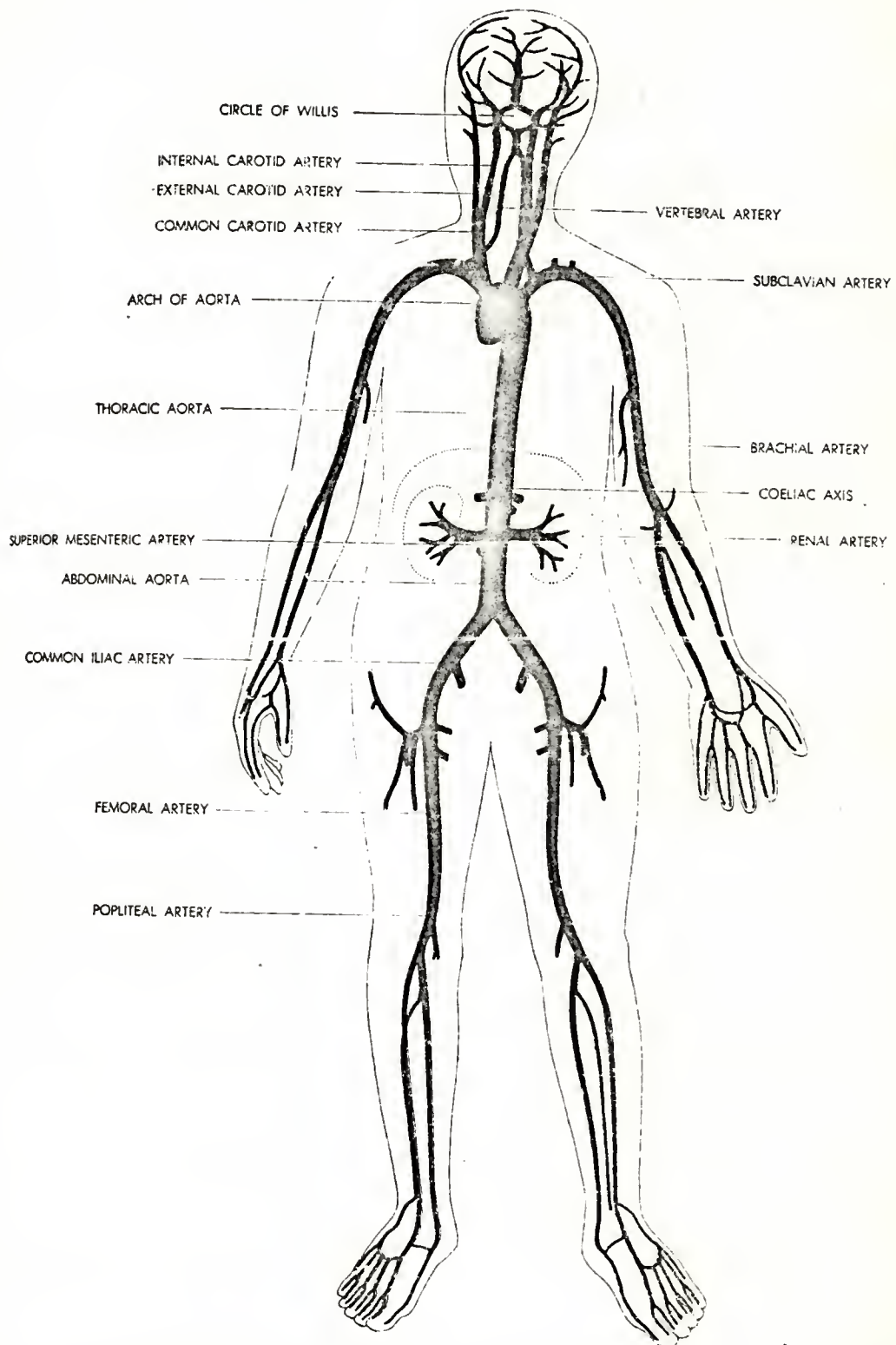
By

WILLIAM JOSEPH CROWE, JR.

A DISSERTATION PRESENTED TO THE GRADUATE COUNCIL OF  
THE UNIVERSITY OF FLORIDA  
IN PARTIAL FULFILLMENT OF THE REQUIREMENTS FOR THE  
DEGREE OF DOCTOR OF PHILOSOPHY

UNIVERSITY OF FLORIDA

1969



Reprinted with permission. Copyright (c) 1961  
by Scientific American, Inc. All rights reserved.

Copyright by  
William Joseph Crowe, Jr.  
1969

*To my lovely wife Doreen  
whose enthusiasm is matched  
only by her imagination*

## ACKNOWLEDGMENTS

Inevitably, in any work such as this there are those people who through their continuing support make it both possible and meaningful. It is a pleasure to acknowledge my indebtedness to them.

I should like to express my genuine appreciation to Dr. R. W. Fahien, who provided much of my fundamental training and introduced me to the field of biomedical engineering, and to Dr. L. J. Krovetz, who provided most of the training, support and facilities for this project.

The logistic support of Dr. G. L. Schiebler has been invaluable.

Technical assistance provided by Mr. Horace Brown was the major reason why the experiments proceeded smoothly.

Thanks are also extended to Dr. Michael DeBakey and Scientific American, Inc. for permission to use their figure as a frontispiece.

Grateful appreciation is extended to the Chemical Engineering Department and National Science Foundation for the opportunities to pursue this work under first an Engineering College Fellowship and later a National Science Foundation Traineeship.

The Departments of Medical Illustrations and Photography deserve much credit for their prompt and courteous service of high quality.

Finally, I should like to thank Mrs. Lawrence Herrin for her careful checking and typing of this manuscript.

## TABLE OF CONTENTS

	<i>Page</i>
ACKNOWLEDGMENTS . . . . .	iv
LIST OF TABLES . . . . .	vii
LIST OF FIGURES . . . . .	viii
LIST OF SYMBOLS . . . . .	xi
ABSTRACT. . . . .	xvii
 SECTION	
I. INTRODUCTION . . . . .	1
A. Problem Statement . . . . .	3
B. Prior Branching Studies. . . . .	5
II. THEORETICAL CONSIDERATIONS . . . . .	13
A. Fundamental Equations . . . . .	13
B. Flow Birefringence . . . . .	23
III. EXPERIMENTAL EQUIPMENT . . . . .	34
A. The Fluid-Perfusion System . . . . .	34
B. The Flow Test Sections . . . . .	38
C. The Optical System . . . . .	43
IV. EXPERIMENTAL TECHNIQUE . . . . .	45
A. Preparation and Storage of the Dye Suspension . . . . .	45
B. Determination of Fluid Physical Properties . . . . .	46
C. Flow Regulation and Collection . . . . .	47
D. Photography. . . . .	49

<i>SECTION</i>	<i>Page</i>
V. THE ANALYSIS OF FLOW-PATTERN PHOTOGRAPHS AND EXPERIMENTAL RESULTS. . . . .	51
A. Isochromatic Shear-Stress Calibration for Laminar Tube Flow . . . . .	52
B. Steady-Flow Experiments . . . . .	67
C. Pulsatile-Flow Experiments. . . . .	104
VI. CONCLUSIONS AND RECOMMENDATIONS . . . . .	111
APPENDICES. . . . .	116
A. THE STEWART-HAMILTON TECHNIQUE. . . . .	117
B. APPARENT-VISCOSITY AND REYNOLDS-NUMBER DATA FOR 1.4% MILLING-YELLOW DYE . . . . .	126
C. PHOTOGRAPHIC DATA . . . . .	127
BIBLIOGRAPHY. . . . .	128
BIOGRAPHICAL SKETCH . . . . .	133

# LIST OF TABLES

<i>Table</i>	<i>Page</i>
1. FLOW TEST SECTIONS. . . . .	41
2. LIGHT-PATH LENGTH AND AVERAGE SHEAR STRESS ALONG THIS PATH AS DIMENSIONLESS FUNCTIONS OF FRACTIONAL DISPLACEMENT IN THE FLUID MEDIUM. . . . .	66
3. APPARENT-VISCOSITY AND REYNOLDS-NUMBER DATA FOR 1.4% MILLING-YELLOW DYE . . . . .	126
4. PHOTOGRAPHIC DATA . . . . .	127

## LIST OF FIGURES

Figure	Page
1. Dye-streamline experiment (Evans Blue in water) by Krovetz for steady flow through a glass branch. . . . .	10
2. Dye-streamline experiment (Evans Blue in water) by Krovetz for steady flow through a plastic branch molded from a dog's artery. . . . .	11
3. Schematic diagram of the experimental setup . . . . .	35
4. Flow wave generated by the rotary bellows pump used for pulsatile-flow experiments . . . . .	39
5. Photograph of the flow test sections. . . . .	42
6. Apparent viscosity and Reynolds number as functions of flow rate for 1.4% Milling-Yellow dye. . . . .	48
7. Isochromatic-band distribution for fully developed laminar flow through a circular tube (I.D. = 3.00 mm) . .	54
8. Schematic cross section of a circular tube, illustrating the refraction of a typical light ray passing from the fluid to the observer. . . . .	56
9. Schematic flow cross section, illustrating a typical light path along which the average shear stress is required . . . . .	63
10. Isochromatic-band distribution for steady flow past a cardiac catheter (O.D. = 1.67 mm) inserted axially into a circular tube (I.D. = 3.00 mm) . . . . .	70
11. Isochromatic-band distribution for steady flow past a beveled needle (O.D. = 0.92 mm) inserted radially through the wall of a circular tube (I.D. = 3.00 mm). . .	75
12. Isochromatic-band distribution for steady flow through a 30° branch of circular cross section (area ratio = 1.0). . . . .	77
13. Flow ratio versus upstream Reynolds number, with area ratio as a parameter, for 30° branches of circular cross section . . . . .	79

<i>Figure</i>	<i>Page</i>
14. <i>Flow ratio versus upstream Reynolds number for Milling-Yellow dye and water in a 30° branch of circular cross section (area ratio = 1.0). . . . .</i>	82
15. <i>Branch entrance lengths versus downstream Reynolds number for steady flow through a 30° branch of circular cross section (area ratio = 1.0). . . . .</i>	86
16. <i>Isochromatic-band distribution for steady flow through a 30° branch of rectangular cross section (area ratio = 1.0). . . . .</i>	89
17. <i>Flow ratio versus upstream Reynolds number for 30° branches of circular and rectangular cross section (area ratios = 1.0). . . . .</i>	90
18. <i>Isochromatic-band distribution for steady flow through a 60° branch of circular cross section (area ratio = 1.0) .</i>	92
19. <i>Branch entrance lengths versus downstream Reynolds number for steady flow through a 60° branch of circular cross section (area ratio = 1.0). . . . .</i>	93
20. <i>Isochromatic-band distribution for steady flow through a 90° branch of circular cross section (area ratio = 1.0) .</i>	95
21. <i>Branch entrance lengths versus downstream Reynolds number for steady flow through a 90° branch of circular cross section (area ratio = 1.0) . . . . .</i>	97
22. <i>Isochromatic-band distribution for steady unseparated flow through a <math>\pm 45^\circ</math> wye branch of circular cross section (area ratio = 1.0). . . . .</i>	99
23. <i>Isochromatic-band distribution for steady separated flow through a <math>\pm 45^\circ</math> wye branch of circular cross section (area ratio = 1.0). . . . .</i>	100
24. <i>Flow ratio versus upstream Reynolds number, with branching angle as a parameter, for branches of circular cross section (area ratios = 1.0) . . . . .</i>	101
25. <i>Branch entrance lengths versus flow-pulse phase angle (time), with area ratio as a parameter, for pulsatile flow through 30° branches of circular cross section . . . .</i>	107

<i>Figure</i>	<i>Page</i>
26. <i>Branch entrance lengths versus flow-pulse phase angle (time), with branching angle as a parameter, for pulsatile flow through branches of circular cross section (area ratios = 1.0). . . . .</i>	<i>108</i>
27. <i>Branch entrance lengths versus flow-pulse phase angle (time), with internal geometry and type of branch as parameters, for pulsatile flow through branches having an area ratio of unity . . . . .</i>	<i>109</i>
28. <i>The Stewart-Hamilton experiment, illustrating a typical indicator-dilution curve . . . . .</i>	<i>118</i>

## LIST OF SYMBOLS

- A* identifies the main downstream stem of a branch  
denotes the arbitrary position of an isochromatic band seen in a flow photograph  
indicator injection site  
mass of indicator injected, (mg)
- A<sub>A</sub>* cross-sectional area of the flowing stream in the main downstream stem A
- A<sub>B</sub>* cross-sectional area of the flowing stream in the side arm B
- a* perpendicular displacement of the light path in the fluid from the center of the tube  
amplitude of the component vibration parallel to the optic axis of the fluid.
- a<sub>max</sub>* maximum value of the perpendicular displacement *a*, (*a<sub>max</sub>* = *R*)
- B* the side arm of a branch  
the point on the outer surface of the circular tube where the observed light ray emerges
- b* lateral displacement of an isochromatic band in the flow photograph, (*b* = *a**n<sub>3</sub>*/*n<sub>1</sub>*)  
amplitude of the component vibration perpendicular to the optic axis of the fluid
- b<sub>max</sub>* maximum value of the band displacement *b*, (*b<sub>max</sub>* = *Rn<sub>3</sub>*/*n<sub>1</sub>*)
- C* the point on the inner surface of the circular tube where the observed light ray emerges from the fluid

$C'$	position of point $C$ after rotation
$C_i$	mass concentration of indicator at point $i$ , (mg/l)
$D$	inside diameter of a circular tube the point on the inner surface of the circular tube where the observed light ray enters the fluid
$D'$	position of point $D$ after rotation
$e$	subscript denoting the entrance to a branch
$F$	arbitrary function of integration
$F_{body}$	total body force acting on the macroscopic branching-flow system
$F_{drag}$	total drag force acting on the macroscopic branching-flow system
$G$	arbitrary function of integration
$\underline{g}$	vector sum of body forces per unit mass of fluid
$i$	subscript denoting an arbitrary downstream point subscript denoting an arbitrary inlet to the macroscopic branching-flow system
$j$	subscript denoting an arbitrary outlet from the macroscopic branching-flow system
$K$	diameter ratio for a circular tube, defined as (outside diameter/inside diameter)
$L$	length of the circular tube
$L_E$	entrance length
$\ell$	length of the light path in the fluid
$M$	total mass contained within the macroscopic branching-flow system

$N$	an arbitrary integer order of an isochromatic band
$N_1$	normal to the surface of the tube at point B
$N_2$	normal to the surface of the tube at point C
$\underline{n}$	outwardly directed unit vector normal to the surface of the macroscopic branching-flow system
$n_1$	index of refraction of medium 1 (air)
$n_2$	index of refraction of medium 2 (glass or Plexiglas)
$n_3$	index of refraction of medium 3 (Milling-Yellow dye)
$n_x$	index of refraction for the component vibration parallel to the optic axis of the fluid
$n_y$	index of refraction for the component vibration perpendicular to the optic axis of the fluid
$O$	coordinate origin
$P$	pressure of the fluid at any point
$\underline{P}$	total momentum of the macroscopic branching-flow system
$Q$	volumetric flow rate
$Q_A$	volumetric flow rate at the injection site A, (1/sec)
$Q_i$	volumetric flow rate at the sampling site $i$ , (1/sec)
$R$	inside radius of the circular tube
$R_e$	Reynolds number based on apparent viscosity and tube diameter, ( $R_e = D\bar{v}\rho/\mu$ )
$r$	radial coordinate
$\vec{r}$	position vector denoting the center of the light path in the fluid

$S$	denotes the surface of the macroscopic branching-flow system
$T$	period of vibration for the incident light beam
$t$	time
$t'$	defined as $t + \frac{T\epsilon}{2\pi}$
$t_s$	sampling time
$V$	denotes the volume occupied by the macroscopic branching-flow system
$\underline{v}$	fluid velocity at any point
$\underline{v}_s$	velocity of the moving surface of the macroscopic branching-flow system at any point
$v$	magnitude of the fluid velocity $\underline{v}$
$v_r$	radial component of the fluid velocity $\underline{v}$
$v_\theta$	angular component of the fluid velocity $\underline{v}$
$v_z$	axial component of the fluid velocity $\underline{v}$
$\bar{v}$	cross-sectional average of $v$
$\overline{v^2}$	cross-sectional average of $v^2$
$w$	subscript denoting the inside wall of the tube
$x$	displacement of the component vibration parallel to the optic axis of the fluid at any time arbitrary coordinate perpendicular to the observer's external line of sight and passing through the center of the tube
$y$	displacement of the component vibration perpendicular to the optic axis of the fluid at any time arbitrary coordinate parallel to the observer's external line of sight and passing through the center of the tube

$y^*$  limit of integration, ( $y^* = (R^2 - a^2)^{\frac{1}{2}}$ )

$z$  axial coordinate

### Greek Symbols

$\alpha$  fractional displacement of the light path in the fluid from the center of the tube, ( $\alpha = a/a_{\max} = a/R$ )

$\beta$  fractional displacement of the isochromatic band in the flow photograph, ( $\beta = b/b_{\max} = a/R = \alpha$ )

$\Delta P$  pressure drop over the length  $L$  of the circular tube

$\delta$  path difference between the interfering vibrations in the fluid

$\epsilon$  angle of rotation between the abscissa describing the incident polarized light and the optic axis of the fluid

$\theta$  angular coordinate

$\theta_1$  angle between the light ray in medium 1 and the normal  $N_1$

$\theta_2$  angle between the light ray in medium 2 and the normal  $N_1$

$\theta_3$  angle between the light ray in medium 2 and the normal  $N_2$

$\theta_4$  angle between the light ray in medium 3 and the normal  $N_2$

$\Lambda$  difference operator meaning the sum over all outlet streams minus the sum over all inlet streams of the macroscopic branching-flow system

$\lambda$  wavelength of incident light (in vacuo)

$\lambda_x$  wavelength of the component vibration parallel to the optic axis of the fluid

$\lambda_y$  wavelength of the component vibration perpendicular to the optic axis of the fluid

$\mu_{app}$	apparent viscosity of the Milling-Yellow dye ( $\mu_{app} = \frac{\pi \Delta P R^4}{8 Q L}$ )
$\mu$	fluid viscosity ( $\mu = \mu_{app}$ for Milling-Yellow dye)
$\pi$	irrational number, 3.14159...
$\rho$	fluid density
$\Sigma$	summation over either inlet or outlet streams of the macroscopic branching-flow system
$\underline{\underline{\tau}}$	shear-stress tensor
$\tau_{rr}$	component of the shear-stress tensor $\underline{\underline{\tau}}$
$\tau_{zz}$	component of the shear-stress tensor $\underline{\underline{\tau}}$
$\tau_{rz}$	component of the shear-stress tensor $\underline{\underline{\tau}}$
$\tau$	magnitude of shear stress (at upstream positions, $\tau = \tau_{rz}$ )
$\tau_w$	wall stress, ( $\tau_w = - \left( \frac{\partial P}{\partial z} \right) \frac{R}{2}$ )
$\Phi$	dimensionless average shear stress, ( $\Phi = \tau(avg)/\tau_w$ )

#### Miscellaneous Symbols

<u>      </u>	underscore denotes a vector quantity
$\overline{\quad}$	overscore denotes an integral average over a cross section
$\overline{\quad}$	overscore also denotes a line segment
$\underline{\quad}$	denotes a tensor quantity
$\  \quad \ $	denotes a tensor quantity
(avg)	denotes an integral average along the light path
(up)	denotes the value at the upstream position
(down)	denotes the value at the downstream position

Abstract of Dissertation Presented to the Graduate Council  
in Partial Fulfillment of the Requirements for the Degree of  
Doctor of Philosophy

STUDIES OF ARTERIAL BRANCHING IN  
MODELS USING FLOW BIREFRINGENCE

By

William Joseph Crowe, Jr.

March, 1969

Chairman: Dr. R. W. Fahien  
Co-chairman: Dr. L. J. Krovetz  
Major Department: Chemical Engineering

The optical technique of flow birefringence (double refraction) has been used to investigate steady and pulsatile flows through drilled Plexiglas branches simulating those of the arterial system. This technique was also used to trace flow disturbances created by inserting needles and cardiac catheters radially and axially into a laminar flow through a circular tube.

The birefringent liquid used was a 1.4% aqueous suspension of the aniline dye Milling Yellow, and birefringence patterns were photographed on 16 mm motion-picture film. The experiments covered a Reynolds-number range from 0 to 250.

A scheme has been proposed for calibrating the isochromatic-band distribution obtained for steady laminar flow through a circular tube against the average shear stress along the light path through the fluid. The optical effects arising from curved boundaries and differences in refractive index have been included in this calibration.

Analysis of birefringence photographs has revealed that regions of flow stasis and boundary-layer separation occur along the outer walls of branches for upstream Reynolds numbers between 20 and 50, depending on the angle of branch. In addition, it has been shown that regions of locally increased shear, where stresses exceed the upstream wall stress, occur along the inner walls of branches if 1. the branching angle is greater than  $30^\circ$ , 2. the upstream Reynolds number is greater than 150 and 3. the downstream arms of the branch are of approximately the same diameter. Birefringence films for pulsatile flows have shown that these regions do not move with the incoming pulse but remain centered approximately one diameter downstream from the point of bifurcation.

It has been suggested that locally increased shearing stress on the arterial intima at sites of branching represents that physical mechanism for initiating wall trauma and atherosclerotic disease which is most closely supported by pathologic data.

Photographic evidence has been presented for the occurrence of spiral secondary flows in branches, and the importance of the resultant mixing effect has been discussed with respect to the Stewart-Hamilton technique for measuring cardiac output.

The propagation of flow disturbances has been characterized by defining branch entrance lengths in terms of distorted birefringence patterns. Entrance-length data and birefringence photographs have shown that as upstream Reynolds number increases, flow disturbances in branches are generated and propagated by the following three processes: 1. the readjustment of a laminar velocity profile, 2. the onset of boundary-

layer separation and 3. the onset of secondary flow.

Both Milling-Yellow dye and water have been used to study the flow-distribution characteristics of branches for steady flows in the Reynolds-number range from 0 to 2100. These experimental results have shown that upstream fluid momentum per unit volume is the principal dynamic variable affecting branching flow distributions and that area ratio is a much more significant geometric parameter than is branching angle.

It has also been shown that wall attachment occurs in branches to the extent that side-arm flow will exceed that in the main downstream stem providing that 1. the branching angle is less than  $60^\circ$ , 2. the upstream Reynolds number is below a certain value which is dependent on the fluid and 3. the diameter of the side arm is approximately equal to that of the main downstream stem.

## SECTION I

### INTRODUCTION

During the past twenty years, engineering research has undergone a transition characterized by continual erosion of once well-defined boundaries separating individual disciplines. One need look no farther than the modern electronics industry, with its increasing dependence on such fields as metallurgy, physical chemistry and chemical engineering, to appreciate this fact. What might be called the *interdisciplinary revolution* has grown both in scope and intensity, affecting not only engineering disciplines but also creating new interfaces with the life and social sciences.

Undoubtedly, several factors have contributed to this process but perhaps two of the most significant have been first, the development of new materials and devices having broad application (e.g., the high-speed electric computer and the laser) and second, the refinement of existing measuring instruments and techniques, coupled with the ever-present desire of researchers to extend known theoretical and experimental results to new areas of research.

The field of biomedical engineering has evolved as a direct consequence of this process and is now enjoying rapid growth both in this country and internationally. Significantly, this growth has occurred at both academic and industrial levels and is reflected by new curricula and publications in the field.

Among those topics receiving attention in the biomedical-engineering literature, none has received more than the cardiovascular system. This is not surprising when one considers that diseases of the circulation are among the most common yet-unsolved problems in medicine and that the circulatory system, featuring unsteady-state heat, mass and momentum transport within materials possessing non-Newtonian rheology and functioning under a closed-loop automatic control system, involves many of the most interesting and challenging engineering problems of the day.

The great majority of biomedical-engineering studies dealing with the cardiovascular system fall into one or both of the following categories: those presenting experimental data obtained from *in vivo*, *in vitro* or model experiments, and those proposing mathematical models and analogs to incorporate existing experimental data. The studies of McDonald, Taylor, Hardung, Womersley, Attinger, Bergel, Noordergraaf and Gessner are a few examples of these.

However, with some notable exceptions,<sup>13,14,16,22,42,47,48,49,50,54</sup> few studies have attempted to correlate either experimental data or theoretical predictions with abnormal clinical and pathological findings. That is to say, little attention has been given to providing physical bases or mechanisms for the formation of observed pathological phenomena, as opposed to providing models simply to explain observed experimental data. The recent work of Fry<sup>16</sup> demonstrating that excessive shearing stress causes wall-tissue erosion is a particularly significant step in

this direction.

The present work represents an attempt to further this approach by focusing attention on experiments with models simulating arterial branches and interpreting experimental results in the light of known findings from the medical literature. The approach here is then in contrast with an engineering-science approach to the problem, wherein one would be concerned with solving the equations of change for various types of fluids and wall conditions.

#### A. Problem Statement

The problem may be posed generally in two parts: First, in the flow range common to the arterial system in man, what physical phenomena may be attributed to the presence of a branch in the flowing stream? Second, what are the implications of these phenomena with respect to wall trauma and atherosclerotic disease, known to have a predilection for formation at such sites in the arterial system? More specifically, the present study seeks to investigate three major areas of branching dynamics under conditions of both steady and pulsatile flow by using the optical technique of flow birefringence. These three areas are: 1. the distribution of wall shearing stresses in branches insofar as determining whether local concentrations might occur which could damage the vessel wall, 2. branching-flow distributions as functions of branching angle and upstream Reynolds number and 3. convective-mixing effects at branches and the propagation of disturbances downstream as these relate

to suspended particles in the blood stream and to the Stewart-Hamilton indicator-dilution technique<sup>19,57</sup> for determining cardiac output.

With the exception of one wye branch, this study has been restricted to branches of the single-side-arm type fabricated from drilled or milled Plexiglas block. Though model branches of this type cannot imitate branches of the arterial tree in every detail, particularly their distensibility and wall characteristics, at least some indications of possible flow behavior in the arterial branches can be obtained in this way; and for those branches rigidly bound by surrounding tissue and muscle, such a model represents at least a good first approximation.

The approach here is primarily experimental and considers only mechanical interactions between the flowing stream and the branch. Though biochemical processes do serve a vital function in the cardiovascular system, there is no reason to suppose *a priori* that biochemical activity at a bifurcation would be any different from that occurring in unbranched arterial segments. On the other hand, there is every reason to suppose that flow behavior at two such sites would be different, perhaps even to the extent of either altering normal biochemical function resulting in the development of arterial disease, as Rodbard's work<sup>42</sup> suggests, or simply causing trauma to the vessel wall, such as that shown in Fry's work.<sup>16</sup> This point is further emphasized by the studies of Texon, Imparato, Helpert and Lord, who have shown experimentally<sup>22</sup>

49,50 that atherosclerosis can be produced artificially in dogs by altering blood-vessel geometry.

There are four important reasons why flow birefringence was chosen as the flow-visualization technique used in the present study:

1. Since flow birefringence is an optical technique, there is no need to introduce probes or other devices into the flow field thereby causing external disturbances.
2. It is possible to study flow behavior throughout the entire branch, not just along a single streamline as with the technique of dye injection.
3. Prior two-dimensional studies<sup>36,37,40,41</sup> have indicated that flow-birefringence patterns can be correlated with the shearing-stress distribution, so the possibility of obtaining shear-stress information in branches directly seemed fruitful.
4. It was felt that flow birefringence would provide a convenient way of tracing flow disturbances and entrance effects downstream.

As early as 1964, Wayland had suggested the possibility of using flow birefringence to study flow disturbances in branches,<sup>51</sup> though this was unknown to the author until recently. Fortunately, the present study has incorporated most of Wayland's suggestions.

#### B. Prior Branching Studies

Interest in the problem of branching flows is not new. In fact, problems of flow distribution have been of engineering concern since ancient times, and, today, relationships between vessel branching and flow

behavior are receiving considerable attention in connection with the design of fluid amplifiers and fluidic digital-logic devices.

On the other hand, physiologic interest in branching has arisen only within the last fifty years and has been sporadic. Recent studies,<sup>47,54</sup> demonstrating that atherosclerosis shows a predilection for formation at sites of branching and curvature in the arterial system, have increased the interest in branching. There now seems little doubt that problems associated with vessel branching on a small scale constitute significant research areas both in engineering and medicine.

Surprisingly little work, either theoretical or experimental, has been published on the branching problem. Poisson's work,<sup>39</sup> concerning reflected and refracted waves at a branch site, was among the earliest theoretical studies of branching. Poisson's results were later repeated by Lord Rayleigh<sup>46</sup> in his discussion of the propagation of sound through branched tubes.

The earliest physiologic interest in vessel branching appears to have been that of Moens<sup>34</sup> and Frank,<sup>15</sup> who were concerned with the propagation of pulsewaves through the arterial tree. Though Frank's study has often been cited, it apparently has never been criticized, which is surprising in view of the fact that it contains numerous mathematical errors. Frank did discuss the problem of a pulsewave encountering a bifurcation but only to the extent of repeating Poisson's formulations (incorrectly) as they appeared in Rayleigh's work.

More recent studies of branching have emphasized both theoretical and experimental approaches. Womersley's study<sup>56</sup> represents the most comprehensive theoretical attack on the problem of mathematically modeling pressure and flow relationships in the arterial tree. His proposed model was based on the linearized Navier-Stokes equations and the equations for an ideally elastic wall. Womersley also considered wave reflections at branches and investigated the frequency dependence of wave-reflection coefficients and input impedance.

Acrivos, Babcock and Pigford<sup>1</sup> considered the problem of flow into an idealized manifold consisting of uniformly spaced side ports of equal area. They proposed a simplified mathematical model based on friction factors and pressure-recovery coefficients and were able to show good agreement with their pressure and flow data for both blowing and sucking manifolds.

Knox<sup>24</sup> considered the more general problem of measuring pressure drops and flow distributions for branches of varying branch angle. He considered branches of the single-side-arm type and determined pressure recoveries at bifurcations. He defined a recovery length for branches as the distance downstream from the branch necessary for the pressure gradient to regain linearity, and his data showed that recovery lengths for the side arms were significantly greater than those for the main stems.

The technique of dye injection was used by Copher and Dick,<sup>11</sup> Hahn, Donald and Grier<sup>18</sup> and by Barnett and Cochrane<sup>5</sup> to study particle and flow distribution in glass models simulating venous flow. Distinct

flow channeling was noted in these experiments.

Helps and McDonald<sup>20,21</sup> investigated venous-flow patterns both *in vivo* and in a glass model and found that at Reynolds numbers less than 1000 injected dye formed a parabolic profile in the tributary, but at the junction circulating movement developed. Two sets of secondary flow were set up in each pipe half, and this persisted "for some distance down the parent trunk until a new parabola was formed across the single trunk".

McDonald<sup>33</sup> used the dye-injection method to show that marked disturbances were present at the aortic bifurcation in a rabbit at Reynolds numbers less than 1000. He reported that dye could be seen to impinge on the wall, and eddies were set up near the orifices of the two branches.

Krovetz<sup>25,27,28</sup> conducted similar studies using glass models and Silastic (silicone rubber) molds of dogs' arteries<sup>35</sup> to simulate arterial branching. He observed and photographed secondary flows which distributed dye particles across the cross section as if the flow were turbulent, even though the upstream flow was well within the laminar range. He found that dye particles were distributed unevenly between the downstream branches if the incoming dye front was laminar but were distributed evenly if the incoming front was turbulent. He also found that the critical upstream Reynolds number for the onset of secondary flow in branches ranged from 58 to 89% of the critical Reynolds

number for the onset of true turbulence in a straight tube.

Another study by Stehbens,<sup>45</sup> reporting a series of experiments on turbulence in glass models simulating arterial bifurcations and the curvature of the carotid artery, found critical Reynolds numbers ranging from 306 to 1473 "calculated for the lowest rate of flow at which turbulence could be induced in the models".

Typical experimental results obtained by Krovetz<sup>27</sup> are shown in Figures 1 and 2. Figure 1 shows a laminar dye front encountering a branch in a glass tube, and Figure 2 is the equivalent experiment for flow through a plastic mold of a dog's artery. In both cases, pronounced secondary flow occurs immediately distal to the bifurcation, and significant mixing occurs in this area. In the glass branch (Figure 1), this mixing proceeds downstream approximately five diameters before any dye enters the side arm; and in the mold (Figure 2), no dye at all enters the upper downstream branch, indicating a definite channeling effect similar to that observed by Barnett and Cochrane.<sup>5</sup> These figures also show that most of the mixing activity occurs near the inner walls of the branches (the medial-crotch region) and that little, if any, mixing occurs near the outer walls in the immediate region of the branches.

Other studies by Attinger<sup>3</sup> and by Fox and Hugh<sup>14</sup> have confirmed that the regions along the outer walls in branches represent areas of boundary-layer separation and local stasis. Attinger used suspended dust particles to trace flow disturbances in branch models for Reynolds

## REYNOLDS NUMBER 1440

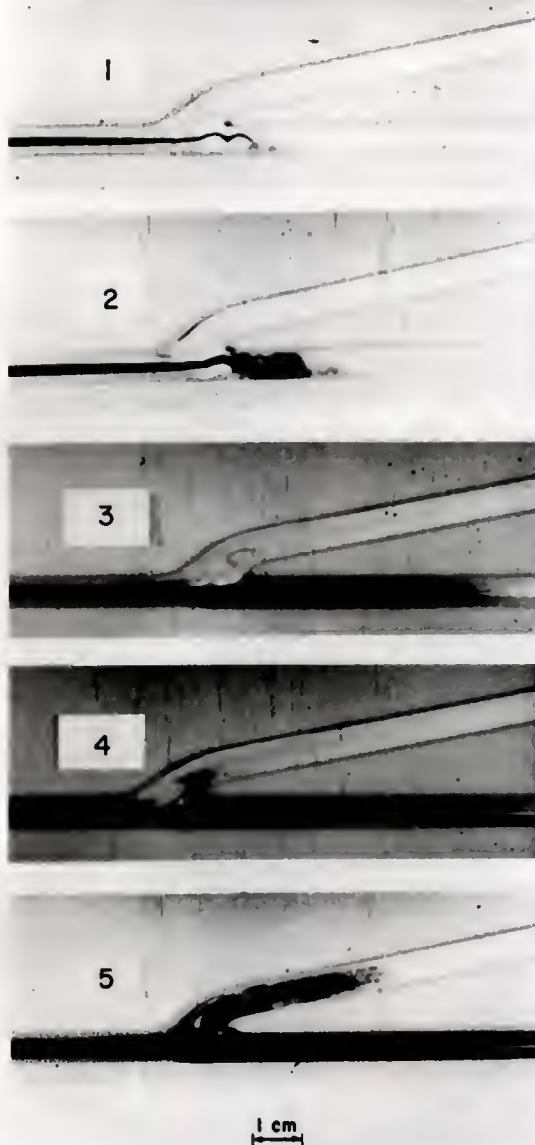


Figure 1. Dye-streamline experiment (Evans Blue in water) by Krovetz for steady flow through a glass branch. Pronounced secondary flow and mixing occur at the branch even though upstream flow is laminar.



Figure 2. Dye-streamline experiment (Evans Blue in water) by Krovetz for steady flow through a plastic branch molded from a dog's artery. Flow channeling and mixing are evident along the medial wall.

numbers up to 10,000. In addition to observing helical flow, he also observed cavitation (which he attributed to air dissolved in the stream) at the highest Reynolds numbers in the regions of boundary-layer separation along the outer walls. Fox and Hugh considered open-channel flows and used aluminum powder sprinkled on the flowing surface to trace disturbances in branched configurations. They postulated that the boundary-layer separation and stasis along the outer branch walls are contributing factors for the deposition of atheromatous plaque there.

## SECTION II

### THEORETICAL CONSIDERATIONS

In this section, we present the basic fluid-dynamic and optical theory underlying the birefringence technique used and derive the macroscopic balances of mass and momentum for a "generalized" branching-flow system. Although the intent here is primarily to develop those mathematical relations needed later for analyzing the flow photographs, a brief discussion of flow birefringence, together with a review of certain previous studies employing this technique, has been included.

#### A. Fundamental Equations

We start by considering the equations of continuity and motion in their Lagrangian form<sup>8</sup>:

$$\frac{D\rho}{Dt} = -\rho \nabla \cdot \underline{v} \quad \text{continuity} \quad (1)$$

$$\rho \frac{D\underline{v}}{Dt} = -\nabla P - \nabla \cdot \underline{\underline{\tau}} + \rho \underline{g} \quad \text{motion} \quad (2)$$

Here,  $\rho$  is the fluid density,  $\underline{v}$  the fluid velocity,  $P$  the pressure,  $\underline{\underline{\tau}}$  the shear-stress tensor and  $\underline{g}$  the vector sum of body forces per unit mass acting on the fluid.  $D/Dt$  is the substantial

derivative defined as  $\frac{\partial}{\partial t} + \underline{v} \cdot \nabla$ .

It is well known that these equations apply in general for any continuous medium and in Lagrangian form apply specifically to elements of fluid moving with the flow.

We wish to consider the set of equations resulting from (1) and (2) for flow through a uniform cylindrical tube of inside radius  $R$ . Anticipating the experimental flow conditions to be encountered later, we use the cylindrical coordinates  $r$ ,  $\theta$  and  $z$  and impose the following assumptions upon Equations (1) and (2).

1.  $\frac{\partial \underline{v}}{\partial t} = \underline{0}$  steady flow
2.  $\rho = \text{constant}$  incompressible flow
3.  $v_\theta = 0, \underline{\tau} = \begin{vmatrix} \tau_{rr} & 0 & \tau_{rz} \\ 0 & 0 & 0 \\ \tau_{rz} & 0 & \tau_{zz} \end{vmatrix}, \frac{\partial \underline{\tau}}{\partial \theta} = \underline{0}$  angularly-symmetric flow
4.  $\frac{\partial v_z}{\partial z} = 0, \frac{\partial \underline{\tau}}{\partial z} = \underline{0}$  fully-developed flow
5.  $\underline{g} = \underline{0}$  no body forces

The symmetry of the stress tensor is recognized in assumption 3, as is the possible existence of normal stresses (such as would occur in a Stokesian fluid).

From the continuity equation (1), we have by assumption 2 that  $\nabla \cdot \underline{v} = 0$ . That is, in cylindrical coordinates

$$\frac{1}{r} \frac{\partial (rv_r)}{\partial r} + \frac{1}{r} \frac{\partial v_\theta}{\partial \theta} + \frac{\partial v_z}{\partial z} = 0 \quad (3)$$

Since the second term of Equation (3) is zero by assumption 3 and the third term zero by assumption 4, the continuity equation becomes simply

$$\frac{\partial (rv_r)}{\partial r} = 0 \quad (4)$$

Integrating Equation (4) directly, we obtain

$$rv_r = G \quad (5)$$

where the function of integration  $G$  is independent of  $r$ .

If Equation (5) is solved for  $v_r$ , then it becomes apparent that  $G$  must be zero on the physical basis that the velocity component  $v_r$  cannot be infinite along the axis  $r = 0$ . We therefore conclude that  $v_r$  itself is zero and that the above assumptions describe a parallel flow with  $v_z$  the only remaining velocity component.

The components of the equation of motion (2) in accordance with assumptions 1 through 5 are

$$\frac{\partial P}{\partial r} = -\frac{1}{r} \frac{\partial(r\tau_{rr})}{\partial r} \quad \text{r-component} \quad (6)$$

$$\frac{\partial P}{\partial \theta} = 0 \quad \text{\theta-component} \quad (7)$$

$$\frac{\partial P}{\partial z} = -\frac{1}{r} \frac{\partial(r\tau_{rz})}{\partial z} \quad \text{z-component} \quad (8)$$

Equation (7) shows that the pressure  $P$  is independent of  $\theta$  and therefore dependent only on  $r$  and  $z$ .

If Equation (6) is differentiated partially with respect to  $z$  and the order of differentiation interchanged on the right-hand side, one has

$$\frac{\partial}{\partial z} \frac{\partial P}{\partial r} = -\frac{1}{r} \frac{\partial}{\partial r} \frac{\partial(r\tau_{rr})}{\partial z} \quad (9)$$

Since the right side of (9) is zero by assumption 4, it follows that

$$\frac{\partial}{\partial z} \frac{\partial P}{\partial r} = 0 \quad (10)$$

That is, the radial pressure gradient is independent of axial position. Because the cross partial derivatives of  $P$  are equal, it follows that

$$\frac{\partial}{\partial r} \frac{\partial P}{\partial z} = 0 \quad (11)$$

That is, the axial pressure gradient is independent of radial position.

According to Equation (8), the axial pressure gradient must also be independent of both  $\theta$  and  $z$ , since differentiation of that equation with respect to either  $\theta$  or  $z$  and interchanging the order of differentiation on the right side renders the right side zero by virtue of either assumption 3 or assumption 4 above. Thus,  $-\frac{\partial P}{\partial z}$  is independent of all three coordinates, and we have the important result that the axial pressure gradient is constant.

Equation (8) may now be integrated directly to give

$$r\tau_{rz} = - \left(\frac{\partial P}{\partial z}\right) \frac{r^2}{2} + F \quad (12)$$

where the function  $F$  is independent of  $r$ .

Solving Equation (12) for  $\tau_{rz}$  and noting that  $\tau_{rz}$  cannot be infinite at  $r = 0$  leads to the conclusion that  $F$  must be zero, and therefore

$$\tau_{rz} = - \left(\frac{\partial P}{\partial z}\right) \frac{r}{2} \quad (13)$$

That is, the shear stress  $\tau_{rz}$  is a linear function of radial position.

Equation (13) represents the starting point for the isochromatic shear-stress calibration to be discussed in Section V. There we shall find it convenient to drop the subscripts on  $\tau_{rz}$  and to consider Equation (13) in terms of the wall stress  $\tau_w$  as follows:

$$\tau = \tau_w \frac{r}{R} \quad (14)$$

$$\text{where } \tau_w = - \left( \frac{\partial P}{\partial z} \right) \frac{R}{2}$$

The preceding derivation involved integrating the equations of continuity and motion over an arbitrary cross section of a circular tube. We now consider the more general problem of integrating these equations over an arbitrary volume in space to obtain the so-called macroscopic balances of mass and momentum.

This problem has been treated by Bird<sup>7</sup> for a system consisting of a "generalized" chemical plant having a single inlet flow and a single outlet flow. We consider the equivalent problem for a "generalized" branching-flow system in which no chemical reactions are occurring but which may have any number of inlet and outlet streams.

The arbitrary region of interest consists of that volume  $V$  bounded laterally by the walls of the branch and bounded at the inlets and outlets by imaginary control surfaces which are assumed fixed in space and time and oriented perpendicular to the direction of mean flow through the inlet or outlet.

It is convenient to start from the equations of continuity and motion in Eulerian form:

$$\frac{\partial \rho}{\partial t} = - \nabla \cdot \rho \underline{v} \quad \text{continuity} \quad (15)$$

$$\frac{\partial \rho \underline{v}}{\partial t} = - \nabla \cdot \rho \underline{v} \underline{v} - \nabla P - \nabla \cdot \underline{\underline{T}} + \rho \underline{g} \quad \text{motion} \quad (16)$$

These equations are easily derived from the corresponding Lagrangian relations (1) and (2), but when written in the above form, they apply to stationary elements of volume.

Integrating the continuity equation over  $V$  we have formally

$$\iiint_V \frac{\partial \rho}{\partial t} dV = - \iiint_V \nabla \cdot \rho \underline{v} dV \quad (17)$$

By an extension of the Leibnitz rule for differentiating an integral,<sup>8</sup> the left side of (17) may be written as

$$\iiint_V \frac{\partial \rho}{\partial t} dV = \frac{d}{dt} \iiint_V \rho dV - \iint_S \rho \underline{v}_S \cdot \underline{n} dS \quad (18)$$

where  $S$  refers to the surface bounding the branch,  $\underline{v}_S$  is the velocity of this surface at any point and  $\underline{n}$  is the outwardly directed unit vector normal to the surface. Note that  $\underline{v}_S$  is zero for a rigid branch, but would not be so in the cardiovascular system.

By the Gauss divergence theorem, the right-hand integral of (17) becomes

$$\iiint_V \nabla \cdot \rho \underline{v} dV = \iint_S \rho \underline{v} \cdot \underline{n} dS \quad (19)$$

where the surface integral is again taken over the bounding surface  $S$ , and  $\underline{v}$  is the velocity of the fluid.

Substituting Equations (18) and (19) into (17) and rearranging terms gives

$$\frac{d}{dt} \iiint_V \rho \, dV = - \iint_S \rho (\underline{v} - \underline{v}_S) \cdot \underline{n} \, dS \quad (20)$$

The left side of Equation (20) is the time rate of change of the total mass  $M$  within the branch. The integrand on the right side vanishes on all solid surfaces, and  $\underline{v}_S$  vanishes on the control surfaces at all inlets and outlets. If we now assume that the density  $\rho$  does not vary across the inlet and outlet surfaces, and note that the normal  $\underline{n}$  is opposite in sense to  $\underline{v}$  for inlet streams but in the same sense as  $\underline{v}$  for the outlet streams we may carry out the above integration to obtain

$$\frac{dM}{dt} = \sum_{\text{IN}} \rho_i \bar{v}_i S_i - \sum_{\text{OUT}} \rho_j \bar{v}_j S_j \quad (21)$$

where the first summation is taken over all inlet streams and the second over all outlet streams. The subscripts  $i$  and  $j$  refer to the  $i$ th inlet stream and  $j$ th outlet stream respectively.  $S_i$  and  $S_j$  are the cross-sectional areas of these streams, and the average velocity  $\bar{v}$  is by definition

$$\bar{v} = \frac{\iint_S v \, dS}{\iint_S dS}$$

where  $v$  is the magnitude of  $\underline{v}$  at the cross section of interest.

If we now define the difference operator  $\Lambda$  as meaning the sum over all inlet streams minus the sum over all outlet streams, then Equation (21) may be conveniently rewritten as

$$\frac{dM}{dt} = -\Lambda(\rho \bar{v} S) \quad (22)$$

Equation (22) is the macroscopic or over-all unsteady-state mass balance for the branching-flow system. Under steady-flow conditions,  $\frac{dM}{dt} = 0$ .

Integrating the equation of motion we have

$$\iiint_V \frac{\partial(\rho \underline{v})}{\partial t} dV = -\iiint_V (\nabla \cdot \rho \underline{v} \underline{v}) dV - \iiint_V (\nabla P) dV - \iiint_V (\nabla \cdot \underline{\tau}) dV \quad (23)$$

$$+ \iiint_V (\rho \underline{g}) dV$$

The left side of this expression may be transformed as before to give

$$\iiint_V \frac{\partial(\rho \underline{v})}{\partial t} dV = \frac{d}{dt} \iiint_V (\rho \underline{v}) dV - \iint_S (\rho \underline{v}) \underline{v}_S \cdot \underline{n} dS \quad (24)$$

The first three integrals on the right side of (23) may be transformed to surface integrals by modifications of the divergence theorem<sup>7</sup> as follows:

$$\iiint_V (\nabla \cdot \rho \underline{v} \underline{v}) dV = \iint_S (\rho \underline{v}) \underline{v} \cdot \underline{n} dS \quad (25)$$

$$\iiint_V (\nabla P) dV = \iint_S P \underline{n} dS \quad (26)$$

$$\iiint_V (\nabla \cdot \underline{\tau}) dV = \iint_S \underline{\tau} \cdot \underline{n} dS \quad (27)$$

Substituting Equations (24) through (27) into (23) and rearranging terms we have

$$\begin{aligned} \frac{d}{dt} \iiint_V \rho \underline{v} dV = & - \iint_S \rho \underline{v} (\underline{v} - \underline{v}_s) \cdot \underline{n} dS - \iint_S P \underline{n} dS \\ & - \iint_S (\underline{r} \cdot \underline{n}) dS + \iiint_V \rho \underline{g} dV \end{aligned} \quad (28)$$

The left side of Equation (28) is the time rate of change of the total momentum  $\underline{P}$  within the branch. Again, the first integrand on the right side vanishes on all solid surfaces, and  $\underline{v}_s$  vanishes at all inlets and outlets. The remaining contribution from this term points in the direction of the flow both at the inlets and outlets. The second term on the right contributes to the influx and efflux of momentum at the inlets and outlets respectively and to the drag force on all solid surfaces. The third term represents the viscous contribution to drag on solid surfaces and gives a usually negligible contribution to momentum transport at flow inlets and outlets. Finally, the last term on the right represents the vector sum of all the body forces  $\underline{F}_{\text{body}}$  acting on the fluid.

Using the previously defined  $\Lambda$  notation, we may write the macroscopic momentum balance for the branching-flow system as

$$\frac{d\underline{P}}{dt} = - \Lambda (\rho \overline{v^2} \underline{S} + P\underline{S}) - \underline{F}_{\text{drag}} + \underline{F}_{\text{body}} \quad (29)$$

where the vector  $\underline{S}$  has a magnitude equal to the cross-sectional area of the inlet or outlet of interest, but points in the direction of the flow.  $\underline{F}_{\text{drag}}$  and  $\overline{v^2}$  are defined as follows:

$$\underline{F}_{\text{drag}} = \iint_{S_{\text{solid}}} P \underline{n} dS + \iint_{S_{\text{solid}}} \underline{\tau} \cdot \underline{n} dS$$

$$\overline{v^2} = \frac{\iint_S v^2 dS}{\iint_S dS}$$

Again, for steady-flow conditions  $\frac{dP}{dt} = 0$ .

### B. Flow Birefringence

According to Jerrard,<sup>23</sup> "the first published observations on flow birefringence were made in 1873, when Mach<sup>30</sup> observed double refraction in extremely viscous substances such as strong metaphosphoric acid and Canada balsam, when poured into a beaker." Soon thereafter, Maxwell<sup>31</sup> reported that he had experimented with birefringence as early as 1866 and had devised a concentric-cylinder apparatus for studying the phenomenon in Canada balsam. Since that time, flow birefringence (also called streaming birefringence and flow double refraction) has been observed in many liquids, and numerous theories of flow birefringence have been proposed. From the extensive reviews of these theories presented by Jerrard<sup>23</sup> and by Cerf and Scheraga,<sup>9</sup> it is evident that no single theory has been successful in predicting

all birefringence phenomena for liquids.

Though most of the early studies of flow birefringence were directed toward using this as a technique for investigating molecular size and shape, within the last forty years, many investigators have reported using birefringence techniques to study the properties of flows themselves. Attinger's recent studies<sup>3,4</sup> of eddy formation and flow disturbances both in distensible tubes and in rigid tubes of circular and elliptical cross section, are typical examples of the qualitative use of flow birefringence. The most significant quantitative work has been that by Prados<sup>41</sup> and Prados and Peebles,<sup>40</sup> who showed that the birefringence technique could be used to determine shear-stress distributions and velocity profiles for flows through various types of flat channels. They used aqueous suspensions of Milling-Yellow dye and obtained good agreement between the flow rates calculated from birefringence measurements and the experimentally determined values. Essentially no quantitative work has been attempted for three-dimensional flow systems, and, apparently, the first attempt to use flow birefringence for studying unsteady or pulsatile flow was the 1957 work of Thurston and Hargrove cited by Prados and Peebles.<sup>40</sup> It is probable that the present study represents the first attempt to use flow birefringence for studying pulsatile flows in branches.

As is the case for photoelastic solids, flow birefringence in liquids results from the optical anisotropy induced by a shearing field. The phenomenon is most pronounced in solutions or suspensions containing asymmetric particles, although it has been observed at high shear rates

in pure liquids (and Newtonian fluids), where the anisotropy presumably arises because of molecular deformation rather than molecular reorientation.

A typical flow-birefringence experiment requires that an incident beam of plane-polarized light (from the polarizer) be passed through the flowing liquid in a direction perpendicular to the direction of flow. The observer then "analyzes" the emerging light by viewing this light through a second polarizer (the analyzer) which is oriented so that its plane of polarization is crossed  $90^\circ$  with respect to that of the incident light. It is found that when the liquid is at rest, the incident beam of polarized light emerges unchanged from the liquid and is extinguished by the analyzer. Thus, the entire field appears dark to the observer under zero-flow conditions. However, when the liquid is set in motion, the observer sees a series of interference bands distributed through the flow field. These bands appear dark when monochromatic light is used and colored when white light is used, and their presence indicates that only under certain conditions does the incident beam emerge unchanged from the flowing liquid.

Although the above description pertains to the use of plane-polarized light, a similar set of results is obtained when circularly polarized light is used. An incident beam of circularly polarized light can be produced by inserting a quarter-wave plate between the polarizer and the liquid such that the optic axis of the quarter-wave

plate makes an angle of  $45^\circ$  with the plane of polarization of the polarizer. The effect of this quarter-wave plate is to decompose the incident plane-polarized vibration into two components vibrating at right angles to one another and  $90^\circ$  out of phase. These are precisely the properties of circularly polarized light. When circularly polarized light is used, it is also necessary to insert a quarter-wave plate between the fluid and the analyzer. This plate is oriented so that its optic axis is crossed  $90^\circ$  with respect to that of the first quarter-wave plate. If a light beam emerges unchanged from the fluid (that is, circularly polarized), the second quarter-wave plate changes the vibration back to a single plane-polarized beam vibrating perpendicular to the plane of polarization of the analyzer. The beam is then extinguished. Regardless of the type of polarized light used, it is true that the observer will see an interference band in the flow field only at positions where the incident light emerges unchanged from the liquid.

The effects of passing beams of plane and circularly polarized light through doubly refracting materials and the conditions under which such beams will emerge unchanged have been treated analytically by Rosenberg.<sup>43</sup> Basically, if a beam of plane-polarized light enters a birefringent liquid, this beam will be decomposed into two component vibrations, one vibrating parallel to the optic axis of the fluid and the other perpendicular to this axis. Initially, these two vibrations

are in phase and may be represented by

$$x = a \cos \left( 2\pi \frac{t}{T} \right) \quad (30)$$

$$y = b \cos \left( 2\pi \frac{t}{T} \right) \quad (31)$$

where  $x$  is the displacement of the component vibration parallel to the optic axis of the fluid,  $y$  the displacement of the component vibration perpendicular to this axis,  $a$  the amplitude of the  $x$ -vibration,  $b$  the amplitude of the  $y$ -vibration, and  $T$  is the period of vibration.

Owing to the optical anisotropy of the flowing liquid, these two vibrations will in general propagate through the liquid at different speeds and will emerge out of phase by an amount dependent upon the path difference (or relative retardation)  $\delta$  between them. The emerging vibrations may therefore be expressed as

$$x = a \cos \left( 2\pi \frac{t}{T} \right) \quad (32)$$

$$y = b \cos 2\pi \left( \frac{t}{T} + \frac{\delta}{\lambda} \right) \quad (33)$$

where  $\lambda$  is the wavelength of the incident beam.

If the emerging components are now recombined by eliminating  $t$ , the resulting equation is

$$\frac{x^2}{a^2} + \frac{y^2}{b^2} - \frac{2xy \cos \left( 2\pi \frac{\delta}{\lambda} \right)}{ab} = \sin^2 \left( 2\pi \frac{\delta}{\lambda} \right) \quad (34)$$

Since Equation (34) describes an ellipse, the emerging beam will in general be elliptically polarized. However, if one compares Equation (34) with Equations (30) and (31), it is apparent that under the following conditions the beam will emerge unchanged

$$\delta = N\lambda, \quad N = 0, 1, 2, \dots \quad (35)$$

$$a = 0 \quad \text{or} \quad b = 0 \quad (36)$$

The first of these conditions governs the appearance of the so-called isochromatic bands (or isochromatics), while the second condition specifies the appearance of the so-called isoclinics. Thus, when plane-polarized light is used, dark fringes can appear at the analyzer from both isochromatics and isoclinics.

Equations (35) and (36) show that the isochromatic bands are related to the magnitude of the path difference  $\delta$ , while the isoclinics appear only when the incident plane-polarized vibration is parallel ( $b = 0$ ) or perpendicular ( $a = 0$ ) to the optic axis of the fluid. It has been found experimentally that the path difference  $\delta$  is dependent upon the length of the light path and upon the average shearing stress along this path while the orientation of the optic axis is dependent upon the direction of shearing stress along the light path. Thus, it is clear that the isochromatics are related to both the magnitude of the shearing stress and the length of the light path, while the isoclinics are related

to the direction of shearing stress along the light path.

The analysis is similar for circularly polarized light. However, since circularly polarized light consists of two mutually perpendicular vibrations which are of equal amplitude but  $90^\circ$  out of phase, each of these vibrations will be decomposed into components vibrating parallel and perpendicular to the optic axis of the fluid. When the appropriate contributions from the incident beam are added, the components propagating through the fluid may be represented by

$$x = a \cos 2\pi \frac{t'}{T} \quad (37)$$

$$y = a \sin 2\pi \frac{t'}{T} \quad (38)$$

where  $a$  is the amplitude of the incident beam,  $T$  the period of vibration and  $t' = t + \frac{T\epsilon}{2\pi}$  with  $\epsilon$  being the angle of rotation between the abscissa describing the incident beam and the optic axis of the fluid.

Again, these components will undergo a relative retardation resulting in a corresponding phase change. Upon emerging from the fluid the components can be represented by

$$x = a \cos 2\pi \frac{t'}{T} \quad (39)$$

$$y = a \sin 2\pi \left( \frac{t'}{T} + \frac{\delta}{\lambda} \right) \quad (40)$$

Equations (39) and (40) can be combined by eliminating  $t'$  to give

$$x^2 + y^2 - 2xy \sin(2\pi \frac{\delta}{\lambda}) = a^2 \cos^2(2\pi \frac{\delta}{\lambda}) \quad (41)$$

Equation (41) also describes an ellipse, and, hence, when circularly polarized light is used, the emerging beam will in general be elliptically polarized. However, comparison of Equation (41) with Equations (37) and (38) shows that the circularly polarized beam will emerge unchanged only if  $\delta = N\lambda$ . Therefore, when circularly polarized light is used, only the isochromatic bands can appear in the flow field.

It has been shown that the condition  $\delta = N\lambda$  corresponds to constructive interference of the emerging vibrations for both plane and circularly polarized light. Since the two vibrations are known to travel at different speeds through the fluid, constructive interference also implies that the difference between the number of waves of each vibration in the fluid is an integer  $N$ . Because the difference in wave speeds of the two vibrations occurs from changes in wavelength and not changes in frequency,<sup>52</sup> constructive interference requires that

$$(\ell/\lambda_x - \ell/\lambda_y) = N \quad (42)$$

where  $\ell$  is the length of the light path,  $\lambda_x$  the wavelength associated with the vibration parallel to the optic axis and  $\lambda_y$  the wavelength associated

with the vibration perpendicular to the optic axis.

Since the frequency of vibration  $f$  is unchanged in the fluid, the wave speeds must obey the following equations

$$c_x = f\lambda_x \quad (43)$$

$$c_y = f\lambda_y \quad (44)$$

The wave speed of any light ray *in vacuo* is given by

$$c = f\lambda \quad (45)$$

where  $c$  is the speed of light,  $f$  the frequency of vibration and  $\lambda$  the wavelength of the vibration *in vacuo*.

If Equation (45) is now divided by Equations (43) and (44) the following relations are obtained:

$$\lambda/\lambda_x = c/c_x = n_x \quad (46)$$

$$\lambda/\lambda_y = c/c_y = n_y \quad (47)$$

where  $n_x$  and  $n_y$  are by definition the indices of refraction for the two vibrations.

Equation (42) may now be rewritten in terms of the indices of refraction  $n_x$  and  $n_y$  as follows:

$$(n_x - n_y) \ell = N\lambda \quad (48)$$

This expression gives the important relation between the so-called *amount of birefringence* ( $n_x - n_y$ ) and the isochromatic-band order  $N$ . The quantities  $n_x$  and  $n_y$  are known as the *optical path lengths* for vibrations  $x$  and  $y$  respectively.<sup>52</sup>

According to Equation (48) the phase difference in radians between the two vibrations is given by

$$\Delta = \frac{2\pi(n_x - n_y) \ell}{\lambda} \quad (49)$$

This is the result given without derivation by Jerrard.<sup>23</sup>

The quantitative application of flow birefringence begins with Equation (48). The usual assumption employed states that the amount of birefringence ( $n_x - n_y$ ) is a linear function of the average shear stress  $\tau(\text{avg})$  along the light path. The results obtained by Prados<sup>40</sup> indicate that this is a good assumption for suspensions of Milling-Yellow dye. This assumption may be stated mathematically as

$$(n_x - n_y) = M\tau(\text{avg}) \quad (50)$$

where the coefficient  $M$  is known as the Maxwell constant.

If the assumption given by Equation (50) is substituted into Equation (48) one has

$$N\lambda = M\ell\tau(\text{avg}) \quad (51)$$

Defining  $M^*$  as  $M/\lambda$ , and rewriting Equation (51) in terms of the

isochromatic-band order  $N$  we have finally

$$N = M * l\tau(\text{avg}) \quad (52)$$

This expression represents the starting point for the analysis of the flow photographs to be presented in Section V.

## SECTION III

### EXPERIMENTAL EQUIPMENT

The production of flow-birefringence patterns requires a relatively simple experimental setup. Basically, the birefringent liquid must be caused to flow through a transparent test section located between two crossed polarizing filters (it is common practice to refer to the incident-light filter as the polarizer and to the second filter as the analyzer). A light source, which may or may not be monochromatic, must be oriented such that the incident unpolarized light passes through the polarizer, test section and analyzer respectively. The observer, looking through the analyzer in the direction of the light source, sees optical interference patterns wherever shear stresses are present and a dark field elsewhere.

The experimental setup used in the present study was designed with simplicity and ease of operation in mind and is pictured schematically in Figure 3. For purpose of discussion, this setup may be conveniently subdivided into three major components: A. The fluid-perfusion system, B. The flow test sections and C. The optical system. Where pertinent, the important pieces of peripheral equipment are also discussed.

#### A. The Fluid-Perfusion System

Since flow birefringence occurs under dynamic conditions,

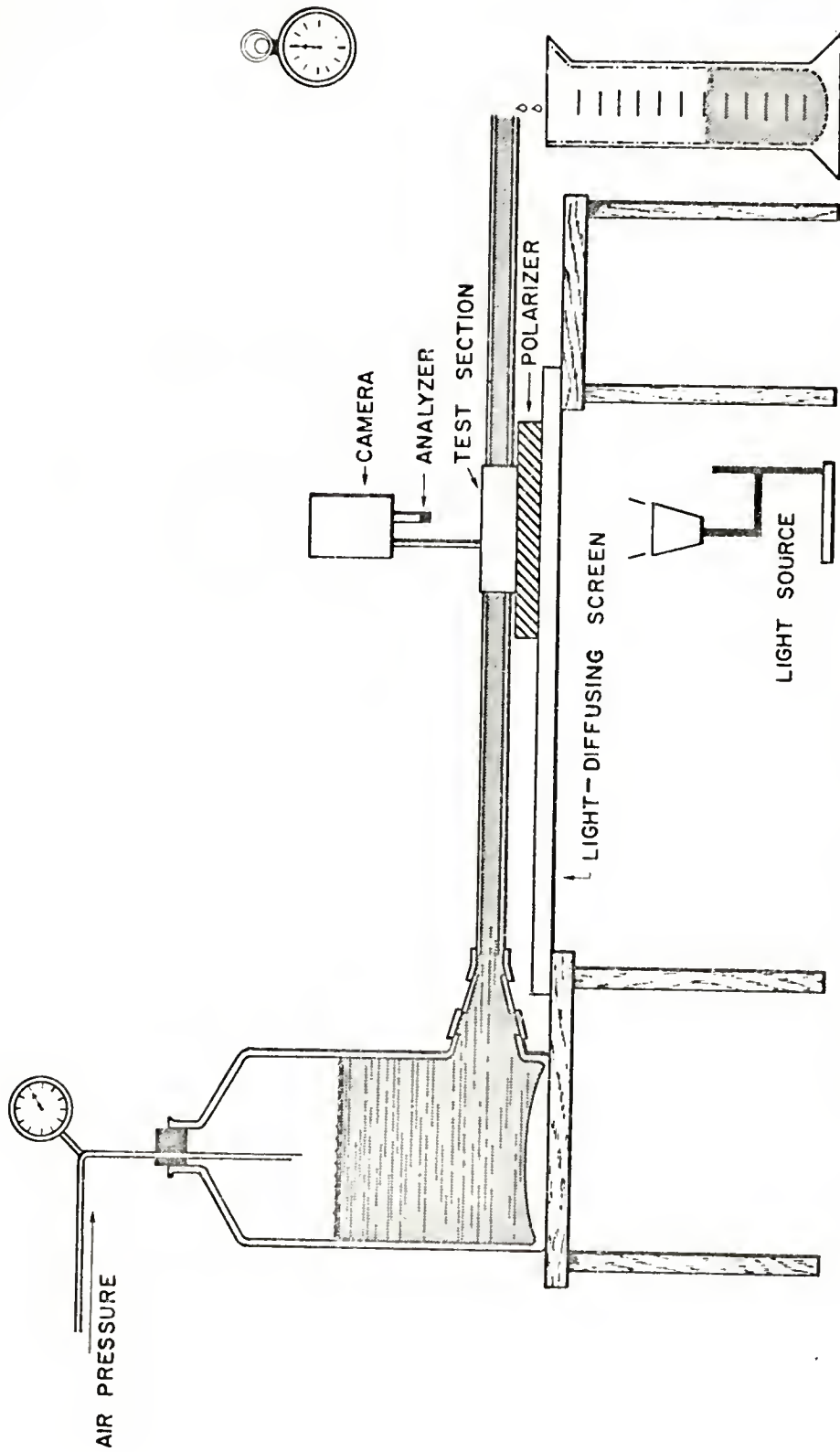


Figure 3. Schematic diagram of the experimental setup. Steady-flow experiments were performed with the apparatus as shown. For pulsatile-flow experiments, the pressurized tank was replaced with a rotary bellows pump.

provision must be made for either recirculating the birefringent fluid through a test section or collecting it after a single pass. It was decided that for branching-flow studies, and in particular for determining branch flow ratios, the best approach was to provide for a single pass through the test sections with fluid collection and metering at the outlets. Direct unobstructed flow metering using graduated cylinders was thus possible, assuring the experimenter that observed flow ratios were due to branch configuration rather than side effects of flow metering. The single-pass approach provided the additional advantage of eliminating the need for a constant-temperature bath to remove viscous heat caused by continuous recirculation. Change in fluid viscosity due to viscous heating was a difficulty reported by Peebles, Prados, and Honeycutt in a previous study.<sup>37</sup>

General requirements were that the fluid-perfusion system be capable of producing both steady and pulsatile flows over the same range of flow rates, that the fluid be maintained at constant temperature and isolated from outside vibration during experimental runs and that the flow system be leveled so as to eliminate gravitational effects in the flow test sections.

Steady flows were generated using the flow system illustrated in Figure 3. This system consisted of a glass tank approximately 30 cm high which could be sealed with a rubber stopper and pressurized using an external compressed-air supply. Though a larger constant-head tank

was available in the laboratory, accurate flow control over a much wider range of flow rates was possible using the pressurized system. A pressure gauge permitted tank air pressure to be monitored to better than 1 mm of mercury over the range 0 to 200 mm of mercury.

The fluid tank was equipped with a tapering outlet nozzle converging to an outside diameter of 9 mm, just sufficient to match the outside diameter of the glass connecting tube joining the fluid tank to the flow test section. This provided for a smooth transition flow from tank to connecting tube. The connecting tube used for all experiments was a 3.00 mm diameter section of precision-bore glass tubing, 96 cm in length. This length was sufficient to insure that fully developed flow entered the test sections.

A tight-fitting rubber sleeve over the nozzle and connecting tube served both as a seal against leaks and a structural support, thus assuring a secure flush connection between nozzle and connecting tube. In addition, this sleeve provided a simple means for adapting the flow system from steady- to pulsatile-flow operation. To do this, it was simply necessary to slide the rubber sleeve off the connecting tube while pinching it to arrest any flow due to fluid in the tank. The glass tube could then be connected directly to the pulsatile-flow source using a section of rubber tubing.

Pulsatile flows simulating heart action were generated using a positive-displacement rotary bellows pump (Model 1000, manufactured by Research Appliance Company, Pittsburgh, Pennsylvania). This pump employed a rotating eccentric cam to displace fluid through a ball valve.

The resulting flow wave was measured independently using a square-wave electromagnetic flowmeter (Model 301, manufactured by Carolina Medical Electronics Company, Winston Salem, North Carolina) and is shown in Figure 4.

Whether operating under steady-or pulsatile-flow conditions, the entire fluid-perfusion system was mounted on sturdy laboratory tables and maintained in an air-conditioned laboratory at a constant ambient temperature of 25°C. External vibration was small but could be minimized by using felt pads for supports and by turning off the air-conditioning system during experimental runs.

#### B. The Flow Test Sections

There are several desirable properties for flow test sections to be used in birefringence work. Among these are that they should be as nearly transparent as possible and of reasonable cost. They should also be easily fabricated from a material in which residual stresses can be removed. If the last requirement is not met, the resulting deformation of crystal planes in the material may render it optically active with respect to polarized light, hence interfering with experimental results.

While there may be no ideal material in every respect, previous studies<sup>40,41</sup> have reported success using Plexiglas test sections. This material can be fabricated with relative ease and is reasonably priced,

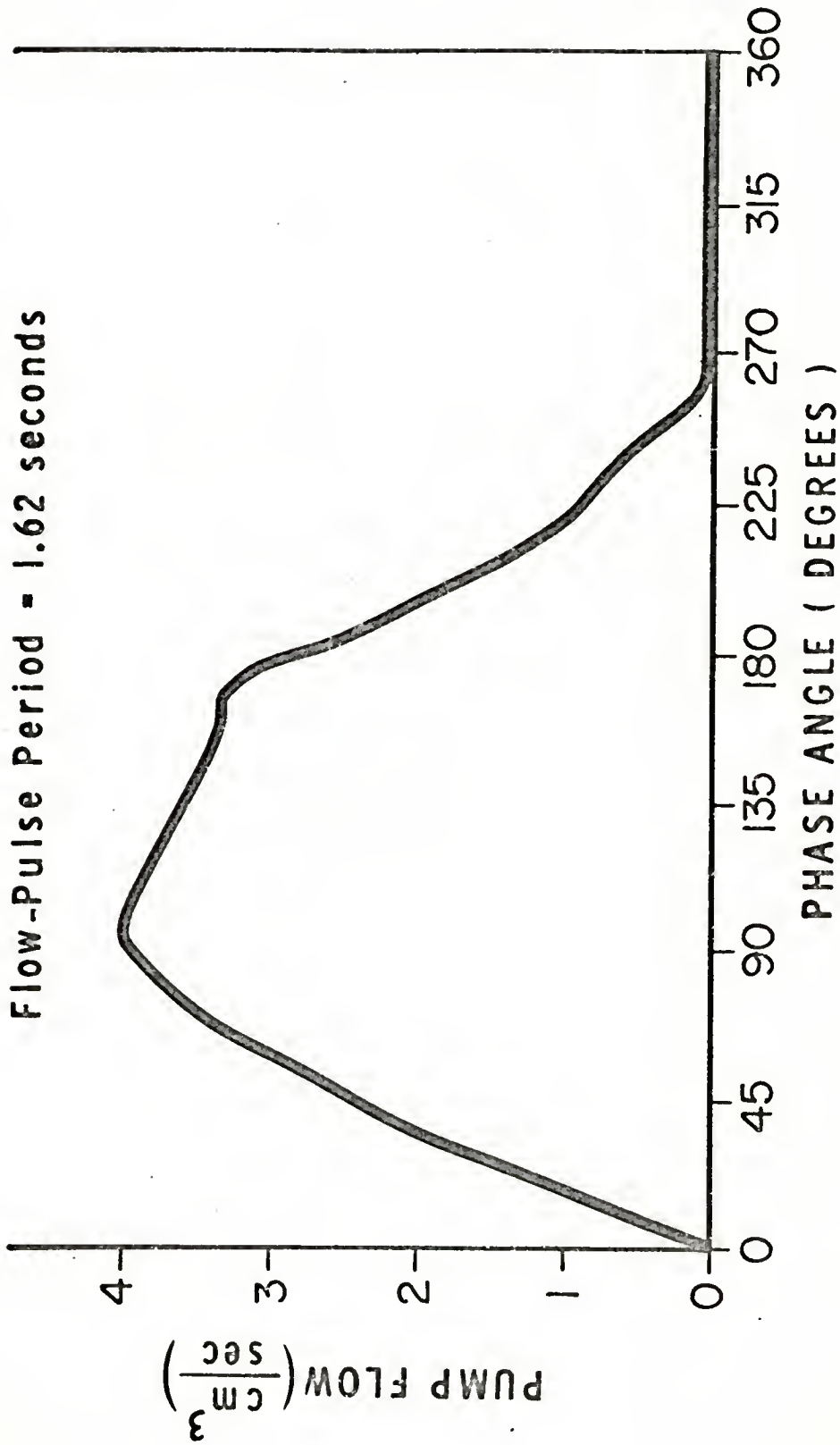


Figure 4. Flow wave generated by the rotary bellows pump used for pulsatile-flow experiments.

although the cost of labor for fabrication may be considerable. Plexiglas is optically active in polarized light when residual stress is present, but this can be removed by proper temperature curing. Such test sections can be polished both inside and out to a high degree of transparency, rendering them ideal from the optical point of view.

The flow test sections used in the present study have been listed in Table 1. With the exception of sections 1, 2 and 7, all test sections were constructed of drilled Plexiglas block and were fabricated in various branched configurations in an attempt to simulate typical branches found in the cardiovascular system.

Fabrication cost imposed a hard limit on the number and variety of branches which could be investigated.

Figure 5 is a photograph of the branched test sections listed in Table 1. Over-all size of these branches was limited by the lengths of the drills available. Test section 7 was milled to a 3 mm wide by 2 mm deep rectangular cross section so that an experimental comparison could be made regarding the effects of internal geometry upon optical and flow-ratio behavior.

Great care was required in drilling the Plexiglas block, as eccentric motion of the drill caused internal burring which could not be removed by later polishing. Care was also necessary to insure that branches met at the proper angles and lay in a plane paralleling that of the broad face of the Plexiglas block.

The upstream faces of all blocks were drilled to a depth of

Table 1

FLOW TEST SECTIONS

<u>No.</u>	<u>Type of Section</u>	<u>Branch Angle</u>	<u>Diameters (mm)</u>			<u>Other Comments</u>
			<u>upstream</u>	<u>main stem</u>	<u>side arm</u>	
1.	Circular Tube	None	3.00	3.00	None	Precision-bore Glass
2.	Square Tube	None	3.0 x 3.0	3.0 x 3.0	None	Precision-bore Glass
3.	Single-side-arm Branch	30°	3.00	3.00	3.00	All branches except Number 7 are of drilled Plexiglas.
4.	Single-side-arm Branch	30°	3.00	3.00	2.00	Longer arms
5.	Single-side-arm Branch	30°	3.00	3.00	1.00	
6.	Single-side-arm Branch	30°	3.17	3.17	3.17	
7.	Single-side-arm Branch	30°	3.0 x 2.0	3.0 x 2.0	3.0 x 2.0	
8.	Single-side-arm Branch	60°	3.00	3.00	3.00	Rectangular cross section (milled)
9.	Single-side-arm Branch	60°	3.17	3.17	3.17	Longer arms
10.	Single-side-arm Branch	90°	3.00	3.00	3.00	
11.	Wye Branch	+45°	3.17	3.17	3.17	Longer arms

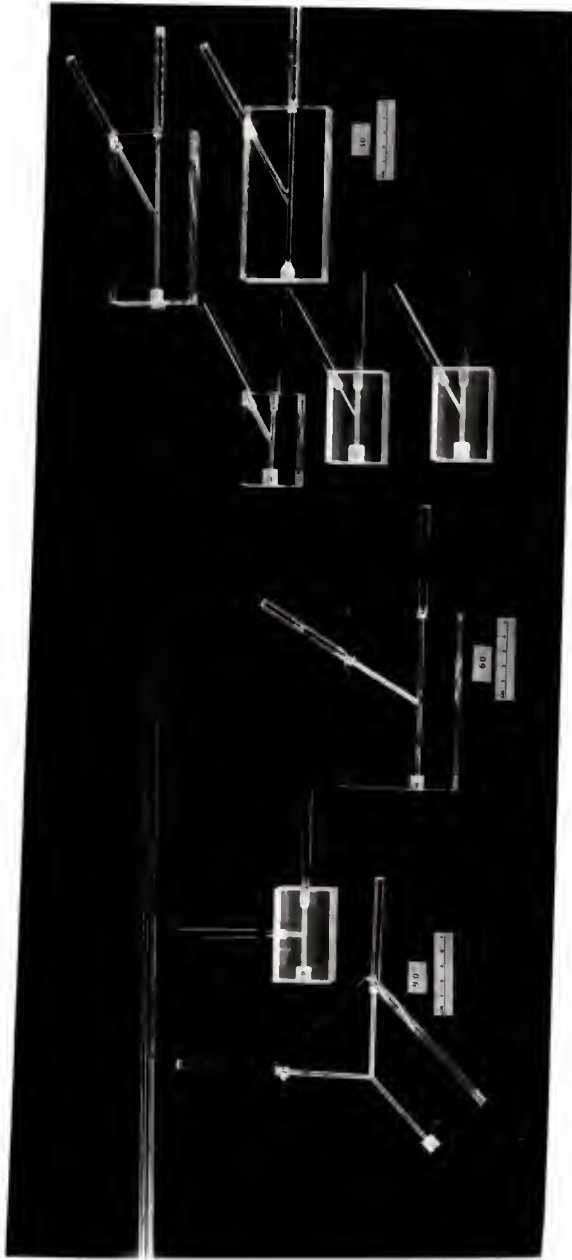


Figure 5. Photograph of the flow test sections. Test sections were fabricated in the form of drilled Plexiglas block. The 30° branch at the top right of the photograph is shown joined to the glass connecting tube and ready for use.

approximately 1 cm on center with the upstream branch stem to accommodate the glass connecting tube with a snug and flush internal fit. Duco cement was used as a leak seal around the connecting tube on the upstream block faces. Figure 5 shows the connecting tube joined to test section 6. Branch outlets were mounted in a similar fashion, and very satisfactory results were obtained using Plexiglas tubing for these.

### C. The Optical System

There are three basic requirements to be considered in designing the optical system. First, this system must be oriented such that the light path is perpendicular to the direction of flow being studied. Secondly, it should be possible to produce incident circularly polarized light as well as plane-polarized light of arbitrary angular orientation. Finally, it should be possible to photograph the resulting birefringence patterns. Figure 3 illustrates the optical scheme adopted.

The light-diffusing screen, consisting of a 60 cm square plate of smoked glass, was mounted horizontally on runners between the two laboratory tables. Mounted in this fashion, the screen provided both a uniformly lighted background and a rigid level support for the polarizer and test sections.

Two Sylvania flood lamps (type R-32, color temperature 3200°K, 375 watt), constituting a white-light source, were mounted on ring stands which rested on the floor. These lamps could be easily raised to compensate for intensity loss due to aging, and heat could be dissipated by a

fan. A white-light source was chosen, because it was felt that the resulting colored bands would be easier to distinguish in the final photographs than the light and dark bands obtained with monochromatic light.

As Figure 3 shows, the polarizer was mounted directly on the light-diffusing screen. Plane-polarized light of various orientations was produced using the edge of the screen as an azimuthal angular reference. A second polarizing filter mounted directly on the camera lens served as the analyzer.

Circularly polarized light could be produced by inserting quarter-wave plates (not shown) between the polarizer and test section and between the test section and analyzer respectively. Again, the edge of the diffusing screen was used as an angular reference for properly inserting these.

The camera used was a Bolex Paillard H-16 (16 mm) Reflex motion-picture camera equipped with a 25 mm lens (1 : 1.4 Switar Rx). This lens in conjunction with 5 mm and 10 mm extension tubes permitted photography from a distance of a few centimeters. The film used was Ektachrome (ER type B) and a Weston light meter (Model 745) was used to check light intensity at the camera. The camera was mounted on a tripod taped securely to the floor. This arrangement permitted easy focusing using the tripod crank. Once focused, the camera could be locked in position and the reflex viewing used to accurately check on proper analyzer orientation by light extinction under zero-flow conditions.

## SECTION IV

### EXPERIMENTAL TECHNIQUE

The experimental work was composed of four parts: A. Preparation and storage of the dye suspension, B. Determination of fluid physical properties, C. Flow regulation and collection and D. Photography.

#### A. Preparation and Storage of the Dye Suspension

The doubly refracting liquid used was a 1.4% aqueous suspension of the aniline dye Milling Yellow (obtained from National Aniline Division, Allied Chemical Company). The suspension was prepared directly from the commercial product, a yellow powder, using the method suggested by Peebles, Garber and Jury.<sup>36</sup>

Distilled water, about 50% in excess of that desired for the final volume, is heating to boiling. To this is added a thick paste of dye powder and distilled water, sufficient to make a 1% suspension by weight. Boiling and agitation are allowed to proceed until excess water has evaporated. Since birefringent sensitivity is markedly affected by dye concentration, the final suspension should contain 1.3 to 1.6% dye for best results. The double-refraction property may be tested during evaporation by withdrawing a small sample into a test tube, cooling to room temperature and observing whether or not interference patterns are produced when the

tube is agitated between illuminated crossed polarizing plates.

After the dye suspension was prepared in sufficient quantity, it was stored in sealed polyethylene tanks until needed for use. It was found that suspensions stored in this fashion were very stable with respect to particle agglutination over a period of two weeks, after which some coagulation occurred.

#### B. Determination of Fluid Physical Properties

To date, the most extensive physical-property studies of Milling-Yellow suspensions are those of Peebles, Prados and Honeycutt<sup>37</sup> establishing the birefringent and rheological behavior. Their studies have shown that viscosity data for Milling-Yellow suspensions are accurately correlated by the Powell-Eyring equation for pseudo-plastic materials. Little work has been done to establish other physical properties for such suspensions.

The physical properties required for the present study were viscosity, density and static refractive index of a 1.4% dye suspension at 25°C.

Viscosity data were obtained by using the 96 cm length of precision-bore 3 mm glass tubing as a capillary viscometer. The dye suspension was permitted to flow through the tube under steady-flow conditions for several different but known pressure gradients. The corresponding flow rates were then measured and the Hagen-Poiseuille equation used to calculate apparent viscosity (that is, the viscosity which a New-

tonian fluid would have flowing through the tube at the same flow rate under the same pressure gradient). Typical experimental results are listed in Table 3, Appendix B, and Figure 6 shows apparent viscosities and the corresponding Reynolds numbers plotted as functions of flow rate  $Q$  in the 3 mm diameter tube. These data are in strong agreement with the data reported by Peebles, Prados and Honeycutt.<sup>37</sup>

Fluid density was determined by weighing 25 ml aliquots of the dye suspension at 25°C. The density was found to be 1.00 gm/cm<sup>3</sup>.

Static-refractive-index measurements were made using a Bausch and Lomb refractometer. The static refractive index at 25°C was found to be 1.338 for the 1.4% suspension. Static refractive index, however, should not be confused with the indices of refraction associated with the ordinary and extraordinary rays when the fluid is in motion. It is not clear just what relationship the static index bears to these two, though Peterlin and Stuart<sup>38</sup> have taken it to be the mean value of the dynamic indices.

### C. Flow Regulation and Collection

The procedure for steady-flow experiments was as follows: Prior to filling the pressure tank with fluid, short rubber tubes were fitted over each flow outlet and clamped to prevent flow. During the experiments, these tubes were unclamped and served to divert outlet flows to large collecting beakers without altering flow distributions in the test sections.

# 1.4 % MILLING-YELLOW SUSPENSION - 3mm DIAMETER TUBE

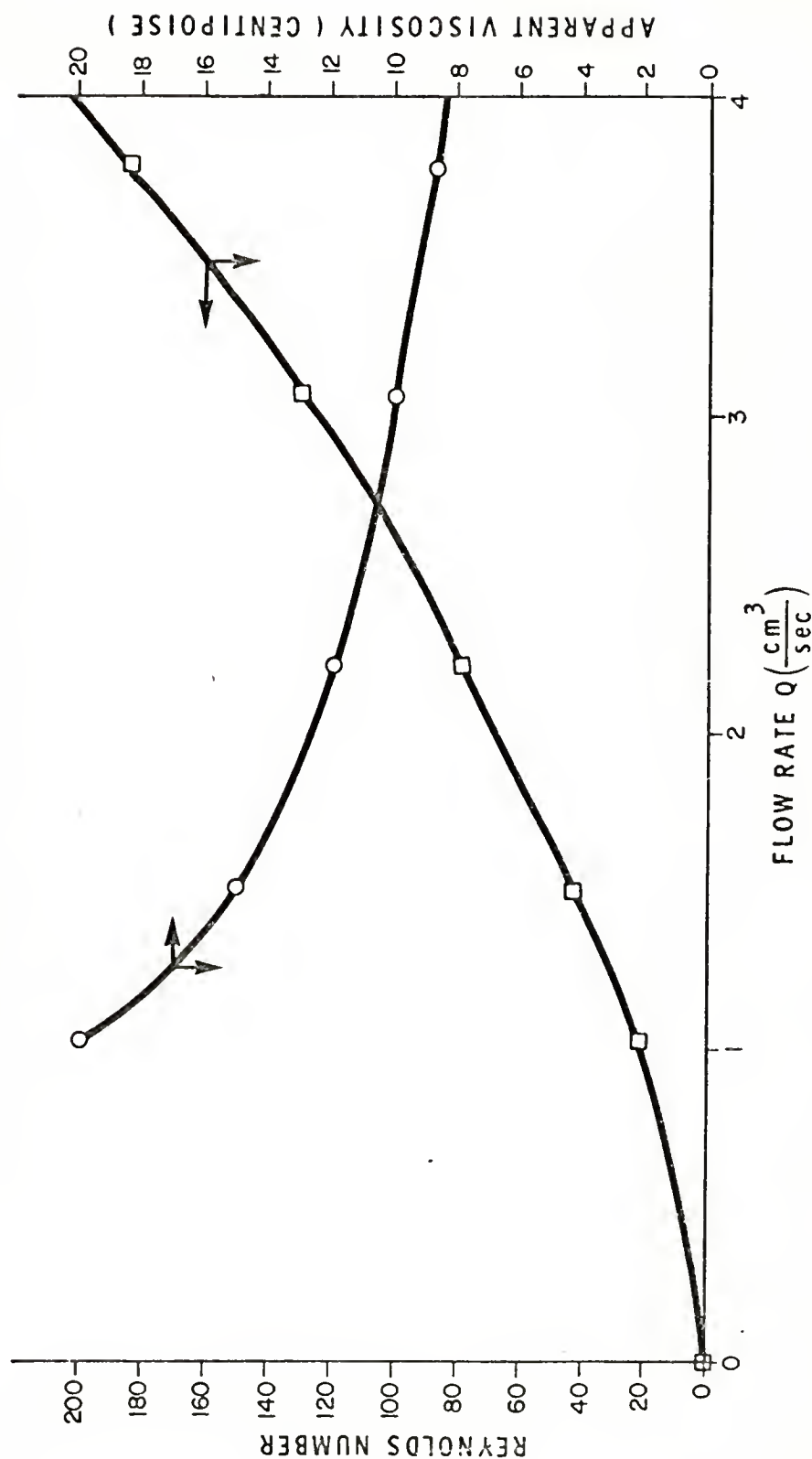


Figure 6. Apparent viscosity and Reynolds number as functions of flow rate for 1.4% Milling-Yellow dye. Decreasing viscosity with increasing flow rate indicates non-Newtonian behavior.

The pressure tank and test section were positioned for photography and the tank filled to a depth of 20 cm with the Milling-Yellow-dye suspension. The laboratory compressed-air supply was then connected to the tank via a three-way valve opened initially to the atmosphere. The pressure gauge in series between the valve and tank permitted tank air pressure to be monitored directly.

For an experimental run, the outlet flows were opened and the valve partially closed until the desired driving pressure was registered on the pressure gauge. Successive experimental runs were made by incrementing the driving pressure in steps of 10 mm of mercury. Before and after each run, the three-way valve was opened to the atmosphere, thus reducing excess tank pressure and lowering the outlet flows. This also permitted the liquid level in the tank to be returned to the 20 cm level. Depending upon the flow rate, experimental runs lasted for 30 seconds or 1 minute. However, the tank was of sufficient capacitance that the liquid level did not drop more than a few millimeters during any experimental run. Outlet flows were measured with graduated cylinders.

For the pulsatile-flow experiments, the pressure tank was replaced by the bellows pump described previously. Since the flow output of this pump was limited to the flow wave already shown in Figure 4, no flow regulation was possible here.

#### D. Photography

Prior to actually photographing the experimental birefringence patterns it was necessary to standardize several important photographic

variables such as light intensity, framing speeds, exposures, depth of field, the film used and processing.

Several preliminary runs were made to test these factors using a color standard made from strips of Kodak red, green and yellow Wratten filters. It was found that Ektachrome film (ER type B) with a corresponding light source having a color temperature of 3200°K gave very good color reproduction when proper exposures were used. All films were processed by the same company so as to minimize any differences due to processing.

Experimental birefringence patterns were photographed with the camera shooting down at the test section mounted in the horizontal plane. After the test section was positioned, the desired exposure and depth of field were set and the lights turned on. The camera was then focused and locked into position. The reflex viewing was used to assure that polarizer and analyzer were crossed by checking for maximum light extinction under zero-flow conditions. Light intensity was checked at the camera using a Weston light meter (Model 745).

The flow was started, and after the desired flow conditions were achieved, the resulting birefringence pattern was photographed. Steady flows were photographed at 16 frames/sec and pulsatile flows at 64 frames/sec.

The pertinent photographic data for the flow photographs appearing in the next section have been listed in Table 4, Appendix C.

## SECTION V

### THE ANALYSIS OF FLOW-PATTERN PHOTOGRAPHS AND EXPERIMENTAL RESULTS

In this section, selected frame enlargements of the 16 mm film are presented together with experimental data obtained from flow measurements and frame-by-frame analysis of the film.

The section is divided into three parts. In Part A, the isochromatic-band pattern obtained for a fully developed, angularly symmetric laminar flow through a tube of circular cross section is considered, and a method is proposed for calibrating this pattern against shearing stress, including the effects of curved boundaries and differences in refractive index in the analysis. In Part B, steady-flow data and isochromatic photographs are presented, and birefringence theory together with the calibration of Part A is applied to estimate shear-stress distributions for flows around a cardiac catheter and through a 90° branch. Experimental results are then compared with results from the medical literature concerning wall trauma and atherosclerotic disease at sites of branching in arteries. In Part C, branch-entrance-length data for the pulsatile-flow experiments are presented, and discussion is focused on the areas of stasis, boundary-layer separation and increased shear readily observed in the films.

### A. Isochromatic Shear-Stress Calibration for Laminar Tube Flow

The problem of isochromatic calibration in flow-birefringence work is that of associating an appropriate value of shear stress with any given isochromatic band in the flow field. In general, this requires that a birefringence experiment be run under conditions of known geometry, shear-stress distribution and isochromatic-band distribution. A correspondence or calibration may then be drawn between the shear field and isochromatic field and this calibration used to determine the shear field in geometries where only the isochromatic field is known.

It will be recalled from Section II that previous studies have demonstrated experimentally that fringe order  $N$  is directly proportional to the product of  $\tau(\text{avg})$ , the average shear stress along the light path, and  $l$ , the length of this path in the fluid. According to Equation (52) that relationship was given as  $N = M^* \tau(\text{avg})$  where  $M^*$  is a characteristic of the particular fluid. Although  $M^*$  is not constant for all fluids, the data of Prados<sup>41</sup> show that this is the case for Milling-Yellow suspensions.

It is evident from Equation (52) that for a three-dimensional flow system in which the light-path length (fluid depth)  $l$  associated with a given band  $N$  is constant, the shear stress  $\tau(\text{avg})$  associated with this band will also be constant. However, if this light-path length varies along the band, then the corresponding shear stress will vary inversely as the path length, and there will no longer be only one appropriate shear stress associated with the given band. A reasonable

approach for this situation would be to establish some reference point along the band (perhaps upstream from the position of interest), and to refer the stress at other positions on the band to the value at this point. This, of course, requires that the light-path length be known at the downstream position.

Previous experimentalists utilizing flow birefringence were able to avoid this difficulty associated with test sections of varying depth by using essentially two-dimensional systems (such as high-aspect-ratio channels).

As will be seen in Part B, the isochromatic bands obtained in the present study represent a combination of the above two cases, with the undisturbed upstream state corresponding to constant light-path length in the fluid and the distorted downstream state to variable length. For this reason, we shall establish the upstream-flow condition as a reference state for branching flows and turn now to the problem of calibrating the isochromatic-band distribution obtained for laminar tube flow.

We consider a steady, incompressible, fully developed laminar flow through a cylindrical tube. A typical isochromatic-band distribution observed for such a flow is that shown in Figure 7 for test section 1. The flow here is from left to right at a Reynolds number of 50 (based on apparent viscosity and inside tube diameter), and the incident light is plane polarized perpendicular to the axis of the tube. It is



Figure 7. Isochromatic-band distribution for fully developed laminar flow through a circular tube (I.D. = 3.00 mm). Plane-polarized light,  $Re = 50$ ,  $\tau_w = 90$  dynes/cm<sup>2</sup>. Note that the bands are not displaced from their original radial position.

seen that the bands parallel the direction of flow and are not displaced from their original radial position as they pass downstream.

In seeking to associate a characteristic value of shear stress with each band, the observer must remember two things: First, successive bands seen in the flow photograph are the net result of viewing the flow through a curved wall, and, hence, through varying liquid depths in the radial direction. Second, since curved boundaries are involved, it is necessary to consider the possibility of optical distortion arising in the flow photograph due to differences in refractive index between the different media involved.

A cross-sectional representation of the over-all situation is shown in Figure 8. For convenience, the coordinate origin  $O$  has been chosen at the center of the tube with lines  $O-N_1$  and  $O-N_2$  representing normals to the tube surface at points  $B$  and  $C$  respectively. Each of the three media involved is characterized optically by a static index of refraction ( $n_1, n_2, n_3$ ). The path of a typical light ray as it enters the fluid from below and passes to the observer is indicated by line  $DCBA$ , and it will be noted that with the exception of the ray passing through the center of the tube, all rays seen by the observer pass obliquely from one medium to the next, thereby undergoing refraction. This refraction is characterized by the angles  $\theta_1, \theta_2, \theta_3$  and  $\theta_4$  which are predictable from geometrical considerations and Snell's law of refraction. These relationships will be considered presently. The

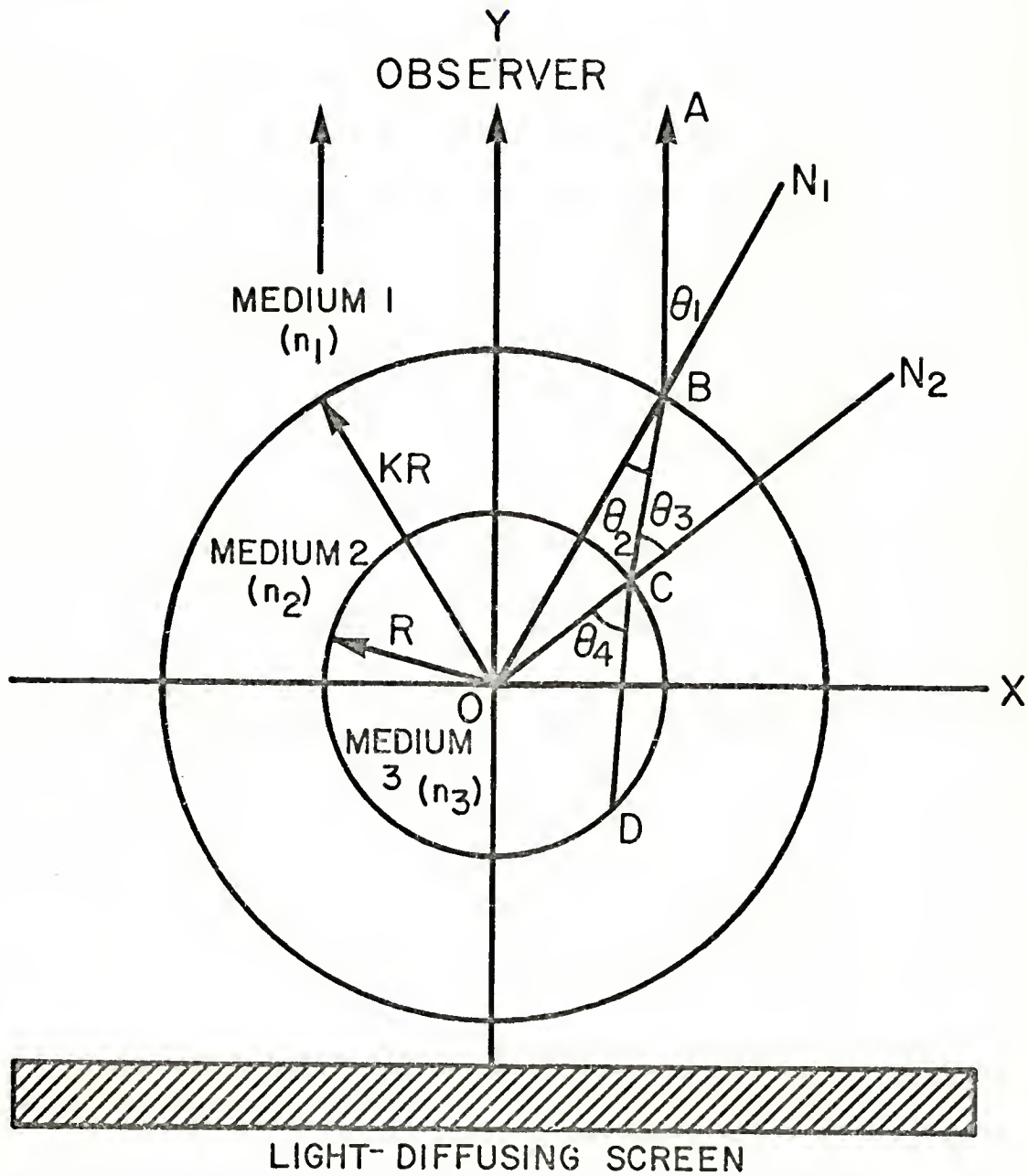


Figure 8. Schematic cross section of a circular tube, illustrating the refraction of a typical light ray passing from the fluid to the observer. Light path DCBA is characterized by angles  $\theta_1$ ,  $\theta_2$ ,  $\theta_3$ , and  $\theta_4$ . These angles are determined by the parameter K and Snell's law of refraction.  $n_1$ ,  $n_2$  and  $n_3$  are indices of refraction.  $N_1$  and  $N_2$  are normals.

observer (camera) viewing from above sees only those light rays emerging parallel to the y-axis, and this implies that chords such as DC, which are the light paths in the fluid corresponding to isochromatic bands seen in the flow photograph, will not in general be parallel to the y-axis.

For the present analysis, we shall choose chord DC as being a typical chord associated with an isochromatic band seen at point A in the photograph and shall identify this chord by its perpendicular displacement from the origin. The lateral displacement from the y-axis of the band at point A is, of course, dependent on the chord's displacement from the origin, and this dependence will now be established by considering the above-mentioned relationships.

It should be mentioned that there is some question as to the justification for using Snell's law of refraction for a doubly refracting material, since it is known that the ordinary ray obeys this law but the extraordinary ray does not. In addition, each of these rays has its own dynamic index of refraction, so the use of the static index must also be justified. Actually, these questions pose no difficulty here, because both rays travel the same path, and, as Peterlin and Stuart have pointed out,<sup>38</sup> the difference between the three indices is very small. Therefore, for the purpose of determining the light path, the static index and Snell's law may be used.

Referring again to Figure 8, one may write the following relations between angles  $\theta_1$ ,  $\theta_2$ ,  $\theta_3$  and  $\theta_4$ :

$$n_1 \sin \theta_1 = n_2 \sin \theta_2 \quad \text{by Snell's law} \quad (53)$$

$$n_2 \sin \theta_3 = n_3 \sin \theta_4 \quad \text{by Snell's law} \quad (54)$$

$$R \cos(\theta_3 - \theta_2) + \overline{BC} \cos \theta_2 = KR \quad \text{Geometry} \quad (55)$$

$$R \sin(\theta_3 - \theta_2) = \overline{BC} \sin \theta_2 \quad \text{Geometry} \quad (56)$$

If  $\theta_1$  is considered the independent variable (this can be done because of the principle of optical reversibility<sup>52</sup>), then these equations may be solved simultaneously to give

$$\theta_2 = \sin^{-1} \left( \frac{n_1}{n_2} \sin \theta_1 \right) \quad (57)$$

$$\theta_3 = \sin^{-1} \left( K \frac{n_1}{n_2} \sin \theta_1 \right) \quad (58)$$

$$\theta_4 = \sin^{-1} \left( K \frac{n_1}{n_3} \sin \theta_1 \right) \quad (59)$$

where the parameter  $K$  is simply (outside diameter)/(inside diameter).

For the special case of a hole drilled parallel to a flat face of a Plexiglas block, these equations still apply providing  $K$  is given a numerical value of unity and  $n_1$  is replaced by  $n_2$ . This is equivalent to immersing the observer in the Plexiglas, since perpendicular viewing would create no refraction at the air-block interface.

One notes from Equation (59) that the angle  $\theta_4$  is completely independent of medium 2 (that is  $n_2$ ). This is a well-known result in optics. Another interesting and important observation is that the diameter ratio  $K$  plays a central role in determining how much of the flow field is actually visible to the observer. This fact may be appreciated by considering the following relationships, which may be

deduced from equations (57) through (59) and the fact that in this study  $n_2 > n_3 > n_1$ .

IF	THEN
$K = 1.0$ and $n_1 = n_2$ (Plexiglas-block case)	$\theta_4 > \theta_1 = \theta_3 = \theta_2$ (60)
$1 < K < \frac{n_3}{n_1}$	$\theta_1 > \theta_4 > \theta_3 > \theta_2$ (61)
$K = \frac{n_3}{n_1}$	$\theta_4 = \theta_1 > \theta_3 > \theta_2$ (62)
$\frac{n_3}{n_1} < K < \frac{n_2}{n_1}$	$\theta_4 > \theta_1 > \theta_3 > \theta_2$ (63)
$K = \frac{n_2}{n_1}$	$\theta_4 > \theta_1 = \theta_3 > \theta_2$ (64)
$K > \frac{n_2}{n_1}$	$\theta_4 > \theta_3 > \theta_1 > \theta_2$ (65)

These relationships show that with the exception of the second case (61),  $\theta_4$  is always greater than or equal to  $\theta_1$ . This is important, because as shown in Figure 8, the magnitude of  $\theta_4$  must range from 0 to 90° if the observer is to see the entire flow field. At the same time, it will be noted that  $\theta_1$  physically can be no greater than 90°. If case (61) holds, that is, if  $K$  falls between 1.0 and  $n_3/n_1$ , then  $\theta_4$  will be less than  $\theta_1$ , and the observer will not be able to see the entire flow field but only the part of it for which  $\theta_4$  ranges from  $-\sin^{-1}(K \frac{n_1}{n_3})$  to  $+\sin^{-1}(K \frac{n_1}{n_3})$  as dictated by Equation (59). Thus, an experimenter conducting

flow-birefringence experiments employing circular tubes and wishing to visualize the entire flow field must consider the geometrical range  $1 < K < n_3/n_1$  a forbidden zone when choosing experimental test sections.

For the flow pictured in Figure 7, the appropriate numerical values are  $K = 3.0$ ,  $n_1 = 1.00$ ,  $n_2 = 1.5$  and  $n_3 = 1.338$ . Since this value of  $K$  is greater than  $n_3/n_1$ , one is assured that the entire flow field is visible in that photograph. In fact, the entire flow field is visible in all photographs appearing in this study. For the branching-flow figures the appropriate numerical values are  $K = 1.0$ ,  $n_1 = n_2 = 1.55$  and  $n_3 = 1.338$ .

It can be seen from Figure 8 that the perpendicular displacement of the typical chord DC from the origin is given by  $R \sin \theta_4$ , and that the lateral displacement of the corresponding band at point A is  $KR \sin \theta_1$ . Defining a *distortion ratio* as (band displacement)/(chord displacement), one obtains a distortion ratio of  $K \frac{\sin \theta_1}{\sin \theta_4}$ . From Equation (59) the value of  $\sin \theta_1 / \sin \theta_4$  is  $n_3/Kn_1$ . Substituting this above gives a distortion ratio of  $n_3/n_1$ . Thus, our analysis shows that for circular geometry the distortion ratio is constant and independent of both the dimensions and the material of medium 2 (the tube). Furthermore, this distortion represents a magnification effect with the distortion ratio  $n_3/n_1$  as the magnification factor. In the present study, this factor has the value 1.338 for the glass tubes; but since  $n_1$  must be replaced by  $n_2$  for the Plexiglas-block studies, the factor becomes 0.865.

for them. In either case, the only optical distortion arising from curvature is magnification or shrinking of the original image by a constant known factor. We can use this information to obtain one more important result. Let the band displacement at point A be denoted by "b" and the corresponding chord displacement by "a". Then, according to the above discussion,  $b = an_3/n_1$ . The displacement b will have its maximum value b(max) when a has its maximum value a(max) = R. Thus,  $b(\text{max}) = Rn_3/n_1$ . If both displacements are now made dimensionless by normalizing them to their maximum values and the *fractional displacements* "β" and "α" defined as  $\beta = b/b(\text{max})$  and  $\alpha = a/a(\text{max})$ , we obtain the important result that  $\beta = (an_3/n_1)/(Rn_3/n_1) = a/R = \alpha$ . This means that the fractional displacement (dimensionless radius) of an isochromatic band measured in the flow photograph is precisely equal to that of the corresponding chord (light path) measured inside the tube.

Now, having related the geometrical properties of the band in the flow photograph to those of the corresponding light path in the fluid, we are in a position to derive the expression relating the fractional displacement α (or β) to the average shear stress along the chord DC.

Up to this point, no mention has been made of the nature of the shear stress distribution in the fluid. From here on, however, it will be assumed that the flow field in the tube is angularly symmetric, which implies that the stress field is also angularly symmetric. The assumption of angular symmetry was verified experimentally for the band distribution

shown in Figure 7.

In Section II it was shown that for the steady, incompressible, angularly symmetric and fully developed flow being considered here the equations of motion could be integrated to give the shear-stress field as a linear function of radial position  $r$ . That function was given by

$$\tau = \tau_w \frac{r}{R}, \quad (66)$$

where the wall stress  $\tau_w$  is  $-\left(\frac{\partial P}{\partial z}\right) \frac{R}{2}$ .

The problem of determining the average value of  $\tau$  over the light path DC can be considerably simplified by taking advantage of the angular symmetry.

Consider the enlarged view of the flow cross section shown schematically in Figure 9. Though the light path DC might in general occupy a position such as that indicated by the position vector  $\vec{r}$ , the assumption of angular symmetry permits this chord to be rotated about the origin to an arbitrary new position without in any way altering the shear-stress distribution along the chord. In particular, if one chooses to rotate chord DC to the position D'C' parallel to the  $y$ -axis, then the average stress from D' to C' is the same as the average stress from  $y = 0$  to  $y = y^*$ , owing to symmetry with respect to reflection in the  $x$ -axis. Thus, the average shear stress along the chord can be obtained by integrating  $\tau$  from  $y = 0$  to  $y = y^* = (R^2 - a^2)^{\frac{1}{2}}$ , where

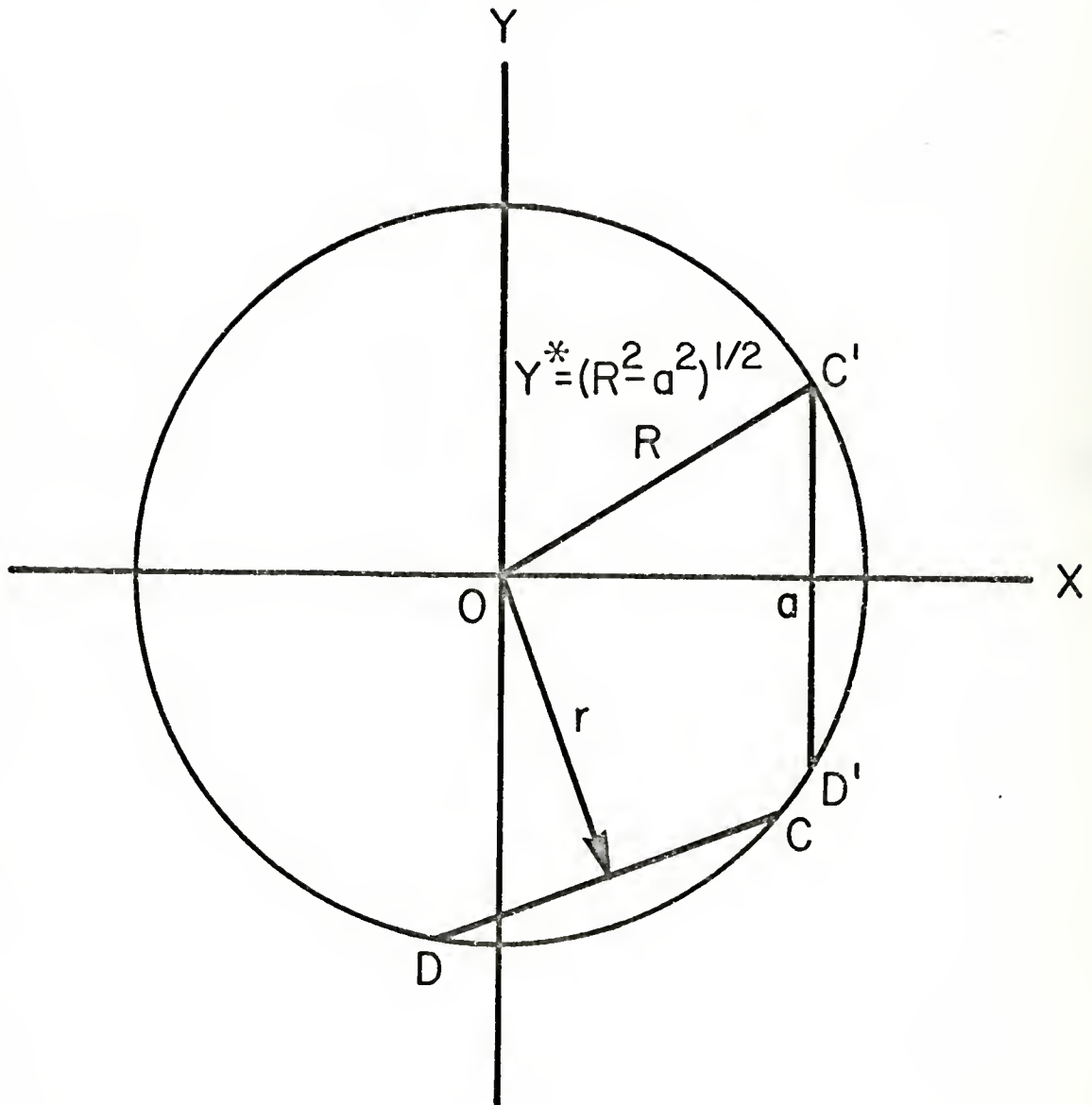


Figure 9. Schematic flow cross section, illustrating a typical light path along which the average shear stress is required. For angularly symmetric flow, the average stress along light path  $DC$  is equal to that along path  $D'C'$ .

the parameter  $a$  is the perpendicular displacement of the chord from the origin.

Along the path D'C', Equation (66) takes the form

$$\tau = \tau_w \frac{(a^2 + y^2)^{\frac{1}{2}}}{R} \quad (67)$$

and the average shear stress  $\tau(\text{avg})$  is given by

$$\tau(\text{avg}) = \frac{\int_0^{y^*} \tau dy}{\int_0^{y^*} dy}, \quad y^* = (R^2 - a^2)^{\frac{1}{2}} \quad (68)$$

Substituting  $\tau$  from Equation (67) into Equation (68) and performing the indicated integrations gives

$$\tau(\text{avg}) = \frac{\tau_w}{2} \left\{ 1 + \frac{a^2}{R(R^2 - a^2)^{\frac{1}{2}}} \ln \left[ \frac{(R^2 - a^2)^{\frac{1}{2}} + R}{a} \right] \right\} \quad (69)$$

If we now define the dimensionless variable  $\phi$  as  $\tau(\text{avg}) / \tau_w$  and rewrite Equation (69) in terms of the fractional displacement  $\alpha$ , we obtain finally

$$\phi = \frac{\tau(\text{avg})}{\tau_w} = \frac{1}{2} \left\{ 1 + \frac{\alpha^2}{(1 - \alpha^2)^{\frac{1}{2}}} \ln \left[ \frac{(1 - \alpha^2)^{\frac{1}{2}} + 1}{\alpha} \right] \right\} \quad (70)$$

This equation gives the desired average shear stress along the light path as a fraction of the wall stress in the tube. On the basis of physical intuition, one would expect  $\phi$  to converge to the values of

0.5 and 1.0 for  $\alpha = 0$  and  $\alpha = 1$  respectively. Although inspection of Equation (70) shows that  $\phi$  is indeterminate at both endpoints, a single application of L'Hospital's rule is sufficient to demonstrate that  $\phi$  does indeed converge to the expected values.

The length  $l$  of the chord D'C' (or DC) may be written in terms of  $\alpha$  by considering the geometry of Figure 9. The relationship between  $l$  and  $\alpha$  is

$$l/2R = (1 - \alpha^2)^{\frac{1}{2}} \quad (71)$$

The right side of Equation (71) thus gives the light-path length in the fluid as a fraction of the inside tube diameter, and, as expected, this length has a value of one diameter for  $\alpha = 0$  and zero for  $\alpha = 1$ .

Numerical results from Equations (70) and (71) have been summarized in Table 2. The first column in the table represents either the fractional displacement of the light path from the center of the tube or the fractional displacement of an isochromatic band as measured in the flow photograph. The second column gives the length of the corresponding light path in the fluid in diameters, and the third column gives the average shear stress along the light path as a fraction of the wall stress in the tube.

As an example of the use of this table, consider the green band which was seen in Figure 7. In the photograph, the center of this band is displaced 10.4 mm from the center of the tube. The edge of the birefringence pattern is displaced 13.0 mm from the center. The fractional

Table 2

LIGHT-PATH LENGTH AND AVERAGE SHEAR STRESS  
ALONG THIS PATH AS DIMENSIONLESS FUNCTIONS  
OF FRACTIONAL DISPLACEMENT IN THE FLUID MEDIUM\*

<u>Fractional</u> <u>Displacement, (<math>\alpha</math> or <math>\beta</math>)</u>	<u>Dimensionless</u> <u>Path Length, (<math>\ell/2R</math>)</u>	<u>Dimensionless</u> <u>Average Shear Stress, <math>\phi</math></u>
0.000	1.000	0.500
0.050	0.999	0.505
0.100	0.995	0.515
0.150	0.989	0.529
0.200	0.980	0.547
0.250	0.968	0.567
0.300	0.954	0.588
0.350	0.937	0.612
0.400	0.917	0.637
0.450	0.893	0.663
0.500	0.866	0.690
0.550	0.835	0.718
0.600	0.800	0.747
0.650	0.760	0.777
0.700	0.714	0.807
0.750	0.661	0.838
0.800	0.600	0.870
0.850	0.527	0.902
0.900	0.436	0.934
0.950	0.312	0.967
1.000	0.000	1.000

- \*NOTES: a. This calibration applies only for fully developed angularly symmetric laminar flow in a circular tube.  
 b. Fractional displacement  $\alpha$  measures the perpendicular displacement between the center of the tube and the chord representing the light path. Fractional displacement  $\beta$  measured in the flow photograph for the corresponding isochromatic band is exactly equal to  $\alpha$ .  
 c.  $\ell/2R$  is calculated from Equation (71).  
 d.  $\phi$  is calculated from Equation (70).

displacement of this band is therefore  $\beta = 10.4/13.0 = 0.8$ . Consulting Table 2, one finds that the light-path length in the fluid corresponding to this displacement is 0.600 diameters. Since the tube is known to have an inside diameter of 3.00 mm, the light path is 1.80 mm long. Finally, from Table 2, the average shear stress associated with this band is 0.870 times the known wall stress of 90 dynes/cm<sup>2</sup>. Therefore, the shear stress associated with the green band is 78.3 dynes/cm<sup>2</sup>.

It should be emphasized that the calibration given by Table 2 applies only to isochromatic bands obtained for tubes of circular-cylindrical geometry under the steady laminar-flow conditions described earlier. These are the upstream conditions prevailing in the steady-flow experiments of this study.

The problem of determining the shear stress at downstream entrance-flow positions in terms of the upstream conditions will be considered in Part B with numerical examples for flows around a cardiac catheter and through a 90° branch.

### B. Steady-Flow Experiments

To facilitate discussion of the following figures, it would be appropriate to discuss first the conventions which have been followed regarding the orientation of the flow photographs and general terminology.

The photographs appearing in this section show typical isochromatic-band patterns for flows through both straight and branched test sections. The observer should keep in mind that for each photograph

the flow is steady and from left to right and for branched test sections this flow is such as to impinge on the bifurcation (that is, all branched flows are of the diverging type).

The convention followed in labeling branches is that side arms have been designated "B" and downstream main stems "A", with the term "upstream" referring to the pre-branch segment.

All Reynolds numbers have been based on apparent viscosity and the pertinent tube diameter as a characteristic length (for the single branch of rectangular cross section, this length has been taken as four times the hydraulic radius, defined as the cross-sectional area of the stream divided by the wetted perimeter).

The term "flow ratio" applies only to branched test sections and is defined as the ratio of the volumetric flow rate in the side arm to that for the downstream main stem (i.e.,  $Q_B/Q_A$ ). Similarly, the term "area ratio" is defined as the ratio of the cross-sectional area of the stream in the side arm to that for the downstream main stem (i.e.,  $A_B/A_A$ ).

Unless otherwise noted, the values of wall stress and Reynolds number given in the figures refer to the upstream (pre-branch) values of these quantities. In each case, upstream wall stress has been experimentally determined as the negative of the pressure gradient multiplied by half the inside radius at the upstream position.

Finally, all entrance-length measurements have been expressed in

dimensionless form by normalizing them to the diameter of the branch for which they apply (i.e., side-arm entrance lengths have been normalized with respect to side-arm diameter and main-stem entrance lengths with respect to main-stem diameter).

Prior to the actual branching studies, it was decided to employ the birefringence technique to obtain isochromatic patterns for steady flows around various needles and cardiac catheters inserted radially and axially into a circular tube. Since the birefringence technique had not been used previously for this purpose, it was hoped that useful information would be obtained regarding the creation and propagation of flow disturbances caused by these devices.

Figure 10 shows an isochromatic-band distribution for steady flow around a catheter (O.D. = 1.67 mm) inserted axially into a cylindrical tube (I.D. = 3.00 mm). Here, plane-polarized light has been used with the plane of polarization perpendicular to the axis of the tube. The upstream Reynolds number for the experiment was 10, and the wall stress was 75 dynes/cm<sup>2</sup>.

In the upstream region, the bands are distributed much as they were for the fully developed flow in Figure 7, but as they encounter the catheter, these bands become noticeably displaced toward the tube wall. The flow-interference front caused by the catheter extends approximately one diameter upstream, and the region between the catheter and the tube wall is recognized as one of accelerated flow owing to the restriction of flow area. The band crowding seen in this region is typical of the

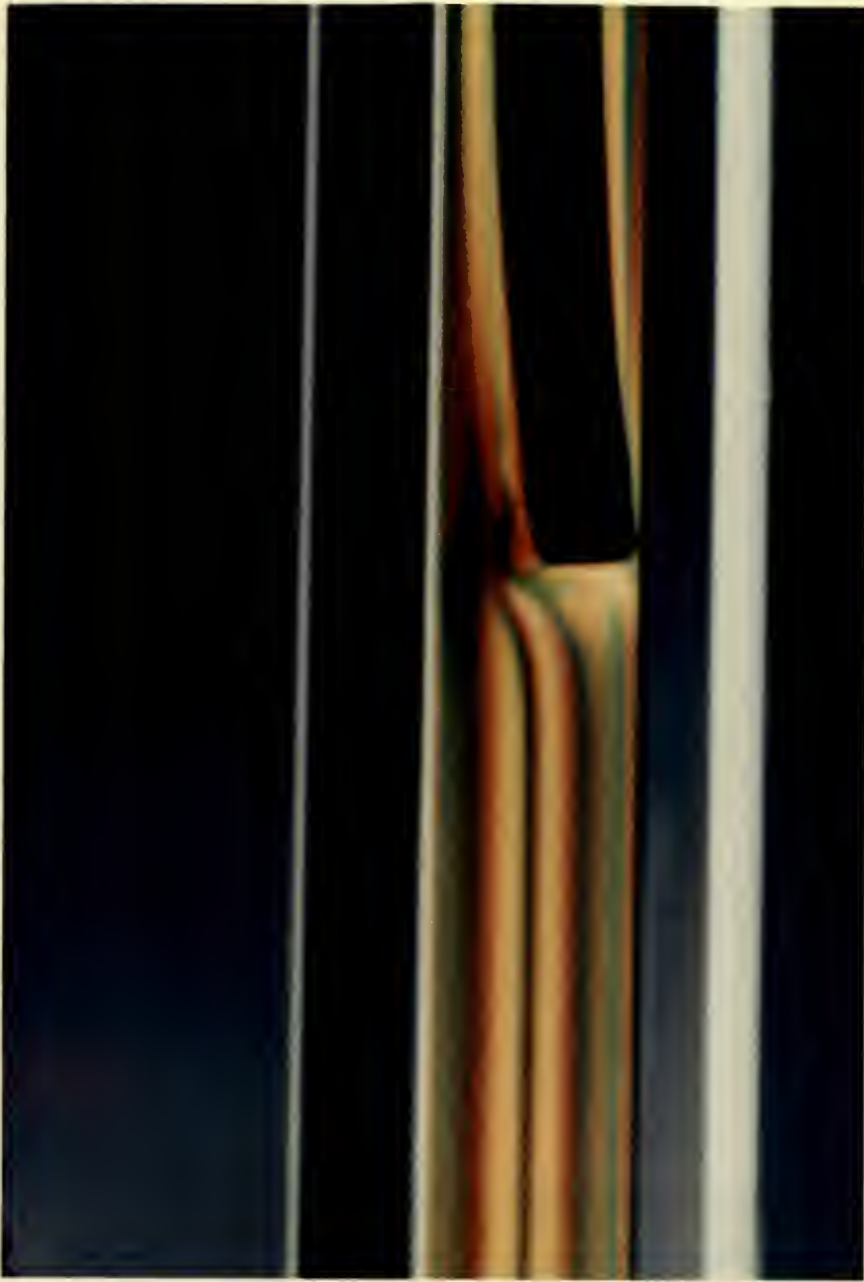


Figure 10. Isochromatic-band distribution for steady flow past a cardiac catheter (O.D. = 1.67 mm) inserted axially into a circular tube (I.D. = 3.00 mm). Plane-polarized light,  $Re = 10$ ,  $\tau_w = 75 \text{ dynes/cm}^2$ . The displacement of bands between the catheter and the tube wall indicates that this is a region of increased shear.

patterns seen for regions of accelerated flow and will also be seen in photographs of branching flows. This crowding of bands provides a clue to areas where one would expect to find increased velocity gradients and shearing stress.

It is apparent from Figure 10 that the flow in the entrance region surrounding the catheter does not correspond to the fully developed flow discussed in Part A. This means that the shear-stress calibration given by Equation (70) in Part A cannot be applied directly to calculate the stress distribution for the entrance region. In fact, since the light-path length varies along the bands in this region, there is no unique stress which can be associated with any band. However, it was intimated in Part A that the fundamental Equation  $N = M*\ell\tau(\text{avg})$  could be used to relate the stress distribution in the entrance region to that in the upstream region of fully developed flow, where the calibration of Part A does apply. In particular, since the coefficient  $M^*$  has been found to be independent of shear rate for Milling-Yellow suspensions, one can apply the above equation to an upstream and downstream point on the same band (or on two different bands of the same order  $N$ ) to obtain

$$\tau(\text{avg, down}) = \frac{\ell \text{ (up)}}{\ell \text{ (down)}} \tau(\text{avg, up}) \quad (72)$$

From Equation (72) it is evident that the average shear stress along the light path at the downstream position can be calculated from

the upstream value for the given band providing that the light-path length at each of the two points is known.

It was shown in Part A that for flow through tubes the light-path length  $l$  is related directly to the observed dimensionless displacement  $\beta$  of the isochromatic band at the point in question by Equation (71),  $l/2R = (1-\beta^2)^{\frac{1}{2}}$ , where we have used the fact that  $\beta = \alpha$ . Since this equation was derived solely from geometrical considerations, it may be applied accurately to both upstream and downstream positions and Equation (72) written as

$$\tau(\text{avg, down}) = \frac{(1-\beta^2(\text{up}))^{\frac{1}{2}}}{(1-\beta^2(\text{down}))^{\frac{1}{2}}} \tau(\text{avg, up}) \quad (73)$$

Here  $\beta(\text{up})$  and  $\beta(\text{down})$  are the dimensionless displacements of the isochromatic band measured in the flow photograph at the upstream and downstream points respectively.

Rewriting Equation (73) in terms of the upstream wall stress  $\tau_w(\text{up})$  and the dimensionless average shear stress  $\phi(\text{up})$  one has

$$\tau(\text{avg, down}) = \frac{(1-\beta^2(\text{up}))^{\frac{1}{2}}}{(1-\beta^2(\text{down}))^{\frac{1}{2}}} \phi(\text{up}) \tau_w(\text{up}) \quad (74)$$

All the quantities on the right side of Equation (74) are known, either from the birefringence experiment or from the shear-stress calibration of Part A. The quantities  $\phi(\text{up})$ ,  $(1-\beta^2(\text{up}))^{\frac{1}{2}}$  and  $(1-\beta^2(\text{down}))^{\frac{1}{2}}$  can be obtained either from Table 2 in Part A for the appropriate value of  $\beta$  or by direct calculation.

As an example, consider the dark band appearing upstream in the center of the tube shown in Figure 10. Encountering the catheter, this band is displaced from its original position,  $\beta = 0$ , through intermediate values of  $\beta$  to a final position,  $\beta = 0.5$ , between the tip of the catheter and the tube wall. Choosing this point as the downstream point of interest and consulting Table 2, one finds the following:

$$\beta(\text{up}) = 0, (1-\beta^2(\text{up}))^{\frac{1}{2}} = 1.000 \text{ and } \phi(\text{up}) = 0.500$$

$$\beta(\text{down}) = 0.5, (1-\beta^2(\text{down}))^{\frac{1}{2}} = 0.866$$

The known wall stress for this experiment is given in Figure 10 as 75 dynes/cm<sup>2</sup>. Inserting these values in Equation (74) gives

$$\tau(\text{avg, down}) = (1.000/0.866) (0.500) (75) = 43.3 \text{ dynes/cm}^2.$$

For comparison, the average shear stress corresponding to this band in the upstream position is

$$\tau(\text{avg, up}) = \phi(\text{up}) \tau_w(\text{up}) = (0.500) (75) = 37.5 \text{ dynes/cm}^2.$$

As expected, the region of accelerated flow is also one of higher shear.

It should be emphasized that the above calculation gives only the average shear stress along the light path at a single downstream position and applies only when the reference (upstream) flow is fully developed as described earlier. By repeating this calculation for bands

falling close to the wall of the tube, one can obtain an estimate of the shear stress acting on the wall.

Figure 11 shows another experiment in which a beveled needle (shank diameter = 0.92 mm) has been inserted through the wall of the cylindrical tube (I.D. = 3.00 mm) and oriented with the bevel facing upstream. The Reynolds number for this experiment was 40, and the upstream wall stress was  $80 \text{ dynes/cm}^2$ . Again, plane-polarized light has been used with the plane of polarization perpendicular to the axis of the tube.

The photograph has been underexposed to emphasize the two distinct vortex patterns seen trailing behind the needle. These patterns persist for approximately two diameters downstream where the disturbance becomes damped out because of fluid viscosity. The region of disturbed flow extends less than one diameter upstream.

Though the vortex patterns are similar in size and shape in this photograph, motion pictures reveal that when the needle is rotated  $90^\circ$ , the lower vortex disappears almost entirely while the upper one remains essentially unchanged. This is evidence that the edge of the bevel creates far less disturbance than does the face. When the needle is rotated further until the bevel faces downstream, the lower vortex reappears but is not as prominent as the upper one. The same experiment using a cylindrical needle having no bevel produces only a single vortex pattern which appears in the center of the tube and is much more streamlined than those in Figure 11. This disturbance also

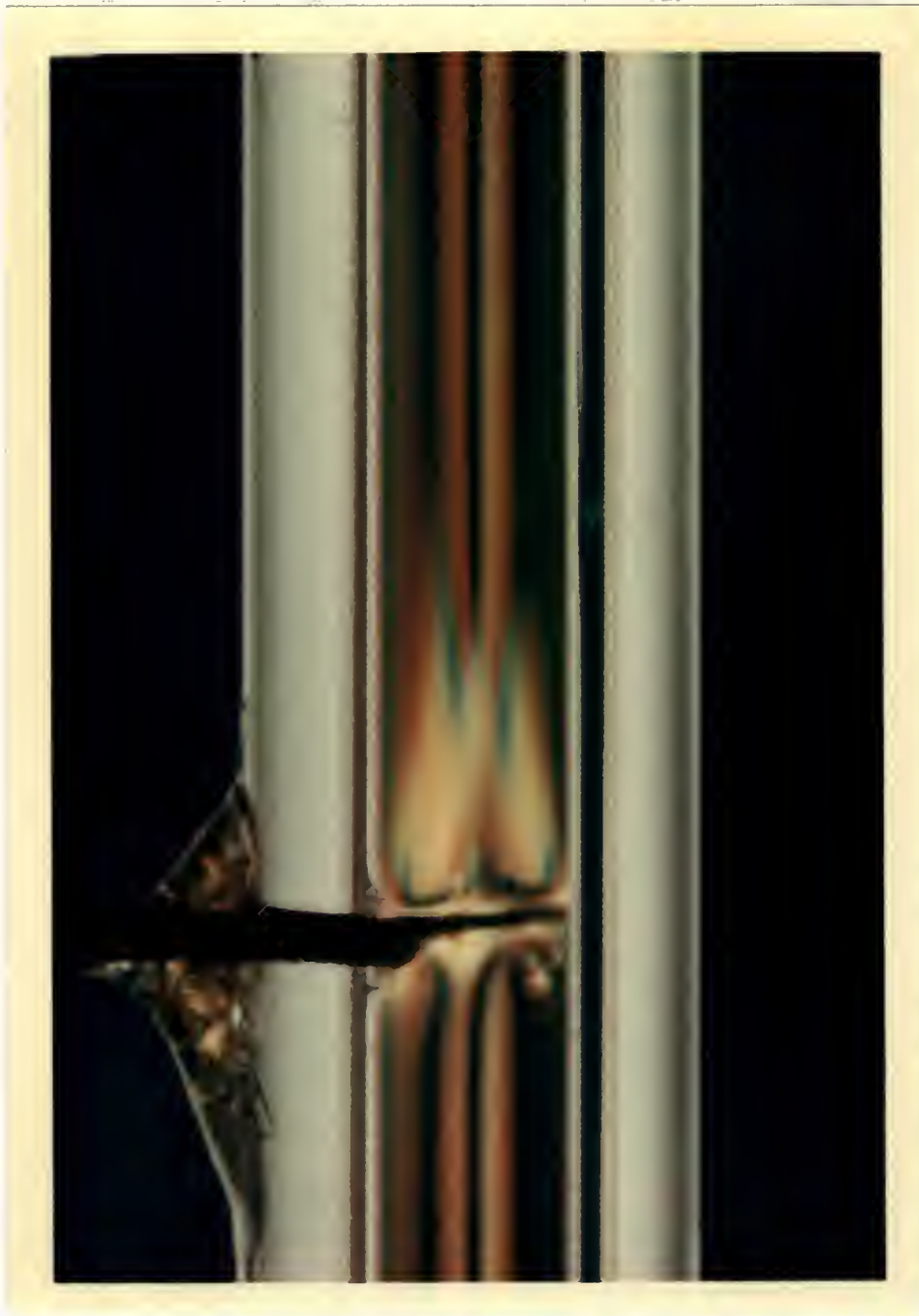


Figure 11. Isochromatic-band distribution for steady flow past a beveled needle (O.D. = 0.92mm) inserted radially through the wall of a circular tube (I.D. = 3.00 mm). Plane-polarized light,  $Re = 40$ ,  $\tau_w = 80 \text{ dynes/cm}^2$ . This distorted birefringence pattern resumes a parallel undisturbed form when the needle is withdrawn to a position flush with the inner wall of the tube.

persists downstream about two diameters.

The most significant finding from these experiments was that when the needles were withdrawn to a position flush with the wall of the tube no disturbances could be seen in the birefringence patterns. This strongly suggests that lateral pressure measurements could be made in small-diameter models as well as *in vivo* without appreciably disturbing the flow.

Figure 12 shows an isochromatic-band distribution obtained using circularly polarized light for the first of the branching-flow experiments. The branch shown (test section 6) has a branching angle of  $30^\circ$  and an area ratio of unity (the side arm and main downstream stem both having an inside diameter of 3.17 mm). The upstream Reynolds number for this experiment was 116 with a corresponding wall stress of  $110 \text{ dynes/cm}^2$ .

Although the bands are parallel to the axis of the tube in the upstream segment, they tend to converge toward the inner walls and distribute themselves concavely about the bifurcation point in the entrance-flow region. This region of disturbed flow extends downstream for a few diameters in both arms until the bands return to the parallel distribution indicative of laminar flow. The fact that the bands tend to be distributed concavely about a stagnation point, such as the point of bifurcation, is helpful in locating zones of stasis at other positions in a flow test section. This will be more apparent in later photographs. The displacement of bands toward the inner walls of the



Figure 12. Isochromatic-band distribution for steady flow through a 30° branch of circular cross section (area ratio = 1.0). Circularly polarized light,  $Re = 116$ ,  $\tau_w = 110$  dynes/cm<sup>2</sup>. The displacement of bands toward the medial walls indicates increased shear in this region.

branch indicates that the regions directly adjacent to the bifurcation represent areas of accelerated flow and increased shearing stress, while the absence of bands toward the outer walls indicates boundary-layer separation in those areas. Aside from the regions immediately adjacent to the bifurcation, there is no evidence for increased stress at any other site in this branch.

Figure 13 gives a comparison of the flow-distribution characteristics for three different  $30^\circ$  branches. Here, flow ratio ( $Q_B/Q_A$ ) has been plotted against upstream Reynolds number with area ratio ( $A_B/A_A$ ) as a parameter. The upper curve applies to the branch just discussed, and the lower two apply to branches having side-arm diameters of 2 mm and 1 mm respectively.

From the over-all decrease of flow ratio with increasing Reynolds number shown by all three branches, it is evident that the upstream flow increasingly favors a straight path into the main downstream stem A as the upstream fluid momentum per unit volume increases. The marked separation between successive pairs of curves in Figure 13 simply verifies that reducing the side-arm diameter is an effective means of controlling side-arm flow over the entire range of upstream Reynolds numbers. It will be seen later that this control is much better than that achieved by increasing the branching angle. The disproportionate increase of flow ratio which occurs below the Reynolds number of 25 is undoubtedly a manifestation of wall attachment by the flow, similar to that observed by Fox and Hugh<sup>14</sup> in their experiments with open-channel

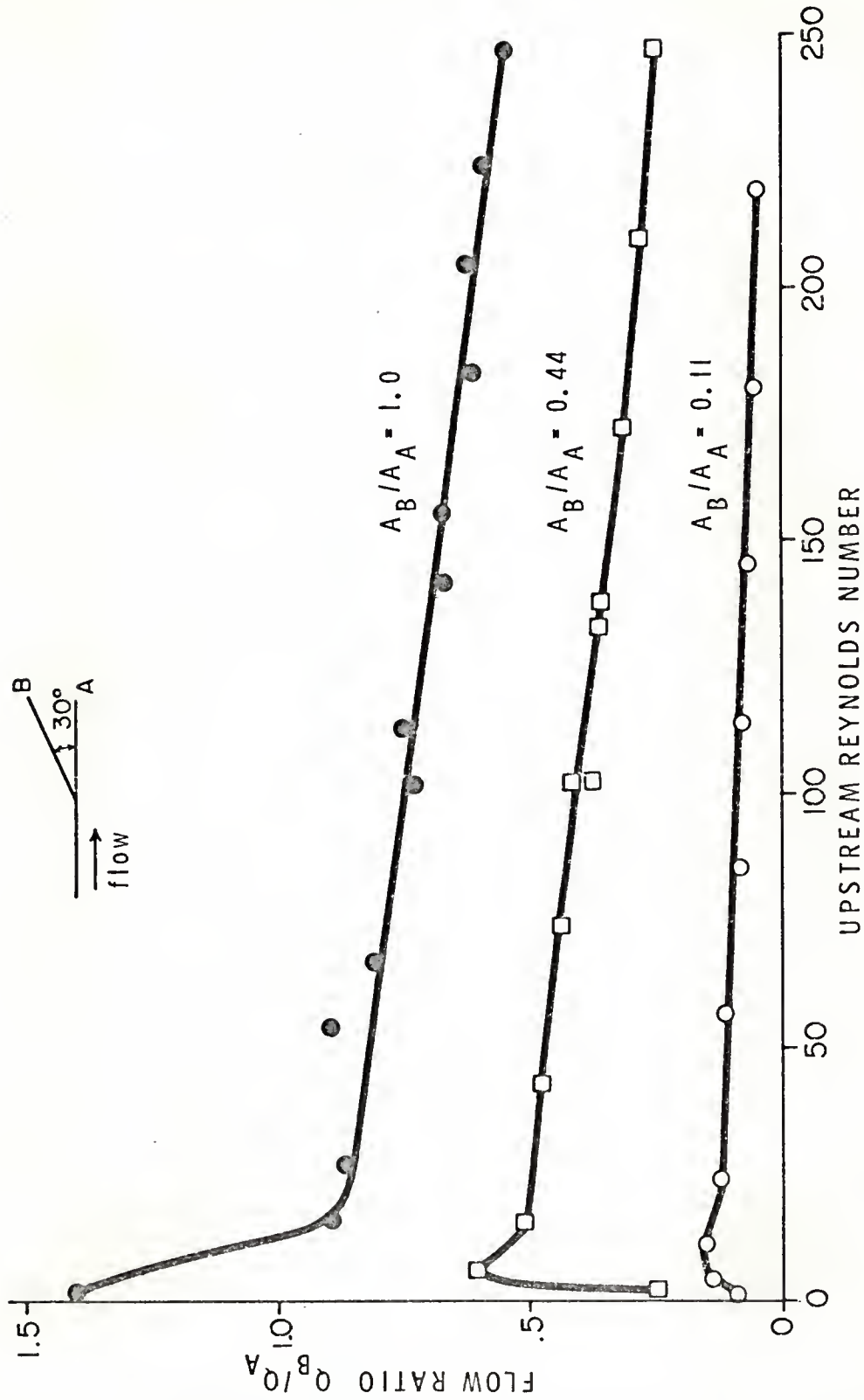


Figure 13. Flow ratio versus upstream Reynolds number, with area ratio as a parameter, for 30° branches of circular cross section. These data indicate that below a certain Reynolds number wall attachment causes side-arm flow  $Q_B$  to exceed main-stem flow  $Q_A$  if the branch area ratio approaches unity.

flows. The data of Figure 13 indicate that for  $30^\circ$  branches wall attachment can cause the side-arm flow to greatly exceed the main-stem flow, but only if the branch area ratio approaches unity and only below a certain upstream Reynolds number.

The phenomenon of wall attachment (sometimes called the Coanda effect) is known to arise because of a low-pressure region generated along the outer side-arm wall owing to fluid moving along curved streamlines concave toward this wall. In branches, this low-pressure region tends to divert a greater fraction of the incoming flow into the side arm until the upstream momentum forces can overcome the pressure forces causing the attachment. At still higher flow rates, the boundary layer separates from the outer wall and a vortex is generated there. The data of Knox<sup>24</sup> indicate that there is a sharp drop in pressure associated with this vortex and a corresponding rise of pressure in the main stem due to the exchange of incoming fluid kinetic energy for pressure energy there.

It has been found that very reliable fluid amplifiers and fluidic digital-logic devices can be produced by carefully designing branches with control ports at the vortex regions. Fluid can be introduced through these ports to destroy a given low-pressure zone, thus causing the main flow to switch from one arm of the branch to the other. Unfortunately, very little has been published concerning the branching-flow characteristics of fluidics devices, since most of this information has been considered proprietary.

It was decided to investigate further the flow-distribution characteristics of the  $30^\circ$  branch shown in Figure 12 by repeating the above experiment with pure water as the working fluid and to compare these results with those for the equivalent experiment with Milling-Yellow dye (the upper curve of Figure 13).

Figure 14 shows the experimental results obtained. Three things are immediately apparent from this figure. First, both the dye and water show an inverse dependence of flow ratio on upstream Reynolds number. Second, though these curves have the same general shape and apply to the same branch, they are separated by a decided jump. Third, though wall attachment causes the dye stream to exceed a flow ratio of unity only for Reynolds numbers below 25, the same effect occurs in water at much higher Reynolds numbers; and, in fact, below a Reynolds number of 250 in water the wall-attachment forces are sufficiently strong so that no flow enters the main downstream stem (that is, complete main-stem cutoff occurs).

These differences can be best understood by comparing the two fluids on the basis of upstream momentum per unit volume rather than on the basis of upstream Reynolds number. Since the Reynolds number reflects viscous forces as well as momentum forces, the reduction in dye viscosity with increasing flow rate affects the lower flow-ratio curve in Figure 14 while no such effect occurs with water. Recalling that over the flow range covered by these experiments the dye suspension had a viscosity from ten to fifteen times that of the water, then when the Reynolds

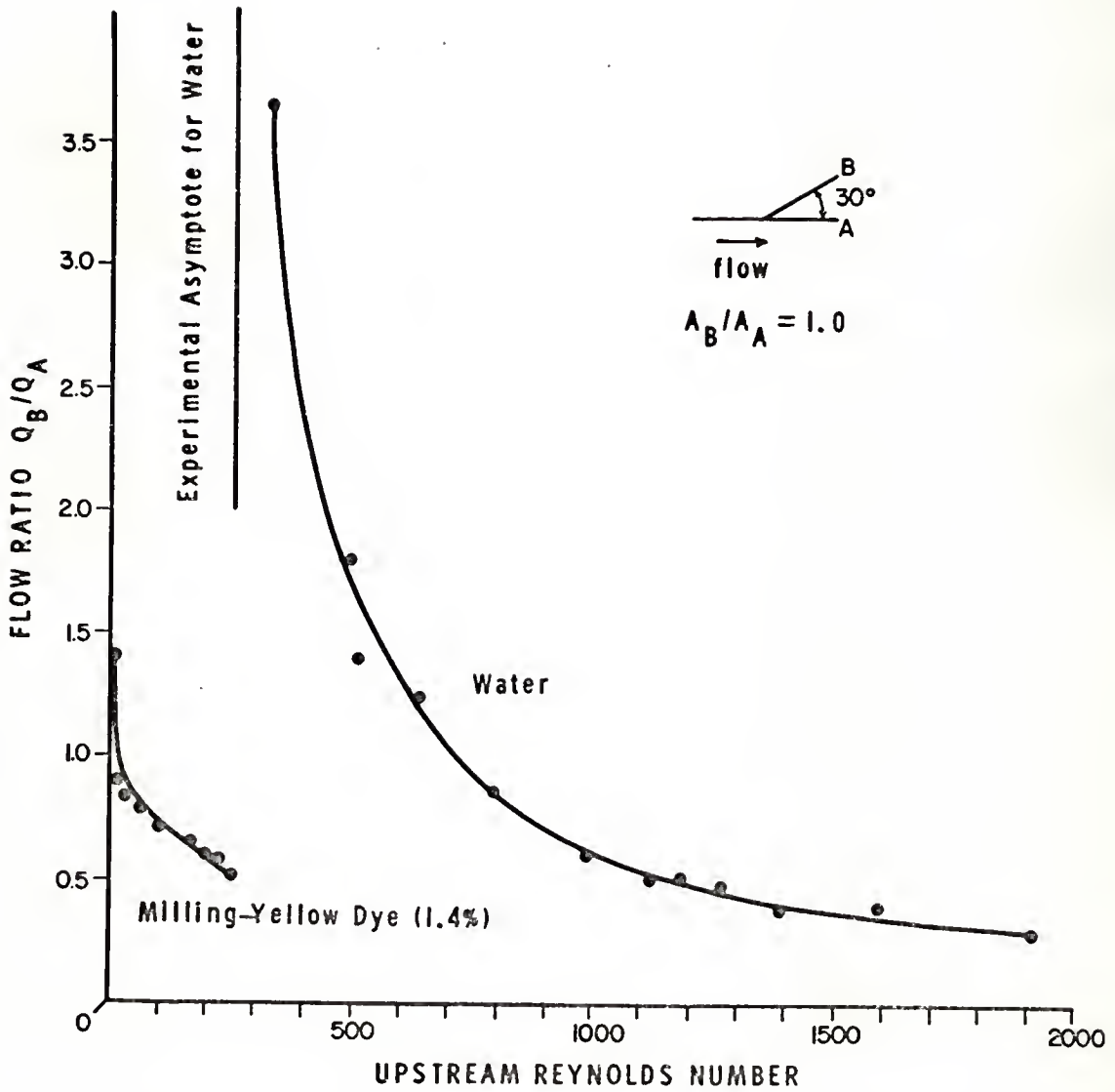


Figure 14. Flow ratio versus upstream Reynolds number for Milling-Yellow dye and water in a 30° branch of circular cross section (area ratio = 1.0). Between the flow ratios of 1.0 and 0.5, the dye and water differ greatly in Reynolds number but differ little in momentum per unit volume. Note that the water also exhibits wall attachment with complete main-stem cutoff occurring for Reynolds numbers below 250.

numbers of dye and water were equal, the dye must also have had a momentum per unit volume from ten to fifteen times that of water. One would expect, therefore, that the greater momentum per unit volume of the entering dye would carry the dye preferentially into the main downstream stem resulting in a lower flow ratio for the dye at any given Reynolds number. This is the case according to Figure 14.

The role of upstream momentum per unit volume becomes even clearer if one compares the two curves in Figure 14 at the same flow ratio rather than at the same Reynolds number.

As an example, imagine a horizontal line intersecting the two curves at a flow ratio of 0.85. At this flow ratio, the corresponding upstream Reynolds numbers are 50 and 800 for the dye and water respectively. That is,

$$\left(\frac{D\bar{v}\rho}{\mu}\right)_{\text{water}} = 800 \quad (75)$$

$$\left(\frac{D\bar{v}\rho}{\mu}\right)_{\text{dye}} = 50 \quad (76)$$

Since the characteristic length  $D$  is the same in each case, the ratio of upstream momentum per unit volume of water to that for the dye is given by

$$\frac{(\rho\bar{v})_{\text{water}}}{(\rho\bar{v})_{\text{dye}}} = \frac{800}{50} \frac{\mu_{\text{water}}}{\mu_{\text{dye}}} = 16 \frac{\mu_{\text{water}}}{\mu_{\text{dye}}} \quad (77)$$

According to the viscosity data given in Figure 6, the apparent viscosity

of the dye at a Reynolds number of 50 is approximately 16 centipoises. Since the viscosity of water may be taken constant at 1.0 centipoise, Equation (77) indicates that at the flow ratio of 0.85 in Figure 14 the upstream momentum per unit volume of the two liquids is the same, even though their Reynolds numbers differ by a factor of 16.

From the above calculation, it would appear that the momentum per unit volume of the incoming stream is the primary factor determining flow distribution in branches. Unfortunately, the comparison obtained for other flow ratios is not as satisfactory. For example, the same calculation for a flow ratio of 0.5 in Figure 14 shows that the upstream momentum per unit volume of the water is only 60% of that for the Milling-Yellow dye. It would seem reasonable to attribute such discrepancies, at least in part, to the presence of secondary flows at the higher Reynolds numbers. However, even with these discrepancies, branching flow ratios for different fluids show a much stronger correlation with upstream momentum per unit volume than with upstream Reynolds number.

Krovetz, Crowe and Santi<sup>25</sup> have shown that, regardless of branching angle, branches in general serve to disturb an entering flow by creating spiral secondary flows in the branch arms. Since these disturbances are also indicated by a corresponding distortion of flow-birefringence patterns, we shall characterize the entrance-flow region for branches by defining a *branch entrance length* for each arm as the distance downstream from the intersection of the branch axes that the distorted birefringence pattern persists. As we shall show in Part C, it is possible by using

frame-by-frame analysis to trace the propagation of such disturbances in time for nonsteady flow as well.

Figure 15 shows the entrance-length data obtained for a series of steady flows through the  $30^\circ$  branch of Figure 12. Here, the advice of Atabek<sup>2</sup> has been followed inasmuch as downstream Reynolds number has been used as the independent variable rather than the upstream Reynolds number used by Knox.<sup>24</sup> The generally accepted correlation<sup>8,44</sup> for entrance flow into cylindrical tubes has also been given in Figure 15 for comparison.

It is apparent that for Reynolds numbers less than 10, the entrance lengths in both arms of the branch increase at a much sharper rate than does the corresponding entrance length in a straight tube. This is undoubtedly due to the asymmetry of the branch. In this Reynolds-number range, the isochromatic patterns show a smooth transition of bands from the upstream segment into the arms, and no band displacement is seen. This indicates that boundary-layer separation has not yet occurred. Between the Reynolds numbers of 10 and 50, both branch entrance lengths show no increase, which indicates that though more kinetic energy enters the branch, this energy is consumed in building an increased disturbance at the bifurcation rather than in propagating the existing disturbance downstream. The data of Figure 15 together with the birefringence films show that this behavior represents the onset of boundary-layer separation. At still higher Reynolds numbers, these disturbances propagate downstream, but the fact that the branch entrance

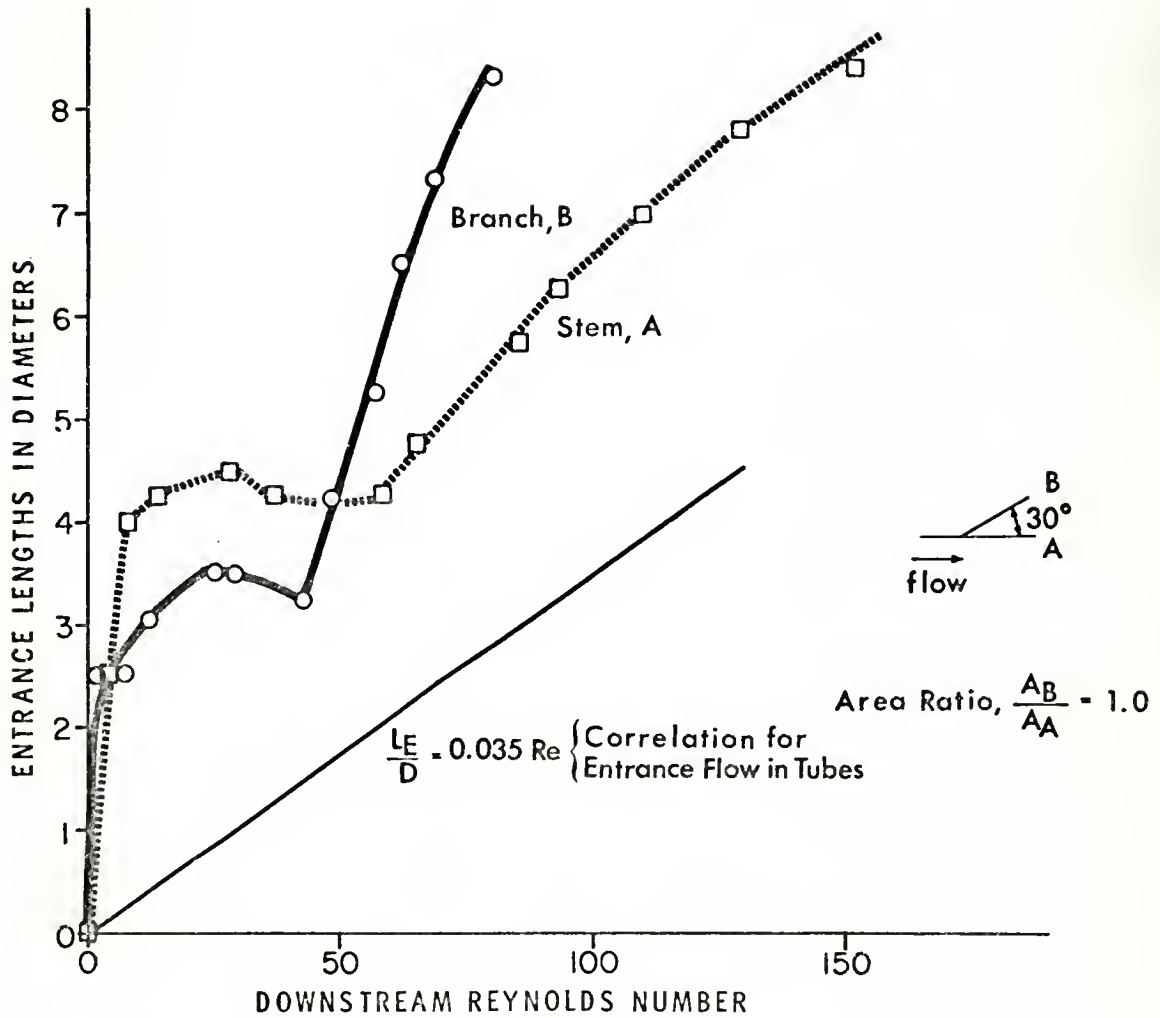


Figure 15. Branch entrance lengths versus downstream Reynolds number for steady flow through a 30° branch of circular cross section (area ratio = 1.0).

lengths taper off shows that some of the additional kinetic energy is spent in creating the secondary flows seen in the films for this flow range. Here the side-arm entrance lengths are considerably greater than those for the main stem at a given Reynolds number, which agrees with the results obtained by Knox.<sup>24</sup>

Basically, Figure 15 shows that there are three phases associated with the propagation of flow disturbances in a  $30^\circ$  branch: 1. the propagation downstream of an initial disturbance associated with the readjustment of the incoming laminar profile, 2. the onset of boundary-layer separation with a corresponding intensification of disturbed flow at the bifurcation and 3. the propagation of this latter disturbance downstream with a corresponding development of secondary flow in the arms of the branch. It will be seen shortly that similar entrance-length patterns are also found for flows in  $60^\circ$  and  $90^\circ$  branches.

Prior to investigating branches having branch angles other than  $30^\circ$ , it was felt that the birefringence patterns and flow-distribution characteristics obtained for the circular branch of Figure 12 should be compared with those obtained for an equivalent branch having a rectangular cross section. The reason for this was twofold: first, to determine whether qualitative differences in the birefringence patterns would occur owing to any optical distortion not accounted for in the analysis of Part A, and, second, to test whether a significant change in internal geometry without a change in branch angle would produce corresponding differences in the dependence of branch flow ratio upon upstream Reynolds number.

Figure 16 shows the isochromatic-band distribution obtained with the  $30^\circ$  rectangular branch (test section 7) for an upstream Reynolds number of 120, which is comparable to the value of 116 for the  $30^\circ$  circular branch shown in Figure 12. In both experiments, the incident light was circularly polarized and the area ratio was unity (the side arm and main downstream stem of the rectangular branch each had a width of 3.00 mm and a depth of 2.00 mm).

Qualitatively, the band distributions in Figures 12 and 16 are similar, and the films indicate that this similarity in birefringence patterns prevails over the entire range of Reynolds numbers studied. The bands in each branch are displaced toward the inner walls at the bifurcation, indicating increased shear in this area, but neither branch shows increased shear at any other point. A well-defined stagnation point is visible along the outer side-arm wall in the rectangular branch (Figure 16), and it is seen that the isochromatic bands tend to distribute themselves concavely about this point. Though the corresponding point in Figure 12 is not as noticeable, both photographs show that this is a region of separated flow. Less well-defined stagnation points can also be seen in these branches on the outer wall of the main stem directly across from the point of bifurcation.

Figure 17 shows the flow-distribution characteristics of the circular and rectangular  $30^\circ$  branches. It is apparent from these data that the marked change in internal geometry has little effect on the flow ratio at a given Reynolds number. The flow-ratio data for the



Figure 16. Isochromatic-band distribution for steady flow through a 30° branch of rectangular cross section (area ratio = 1.0). Circularly polarized light,  $Re \approx 120$ . Note the concave distribution of bands about a well-defined stagnation point (dark spot) along the outer side-arm wall. This is also a point of boundary-layer separation.

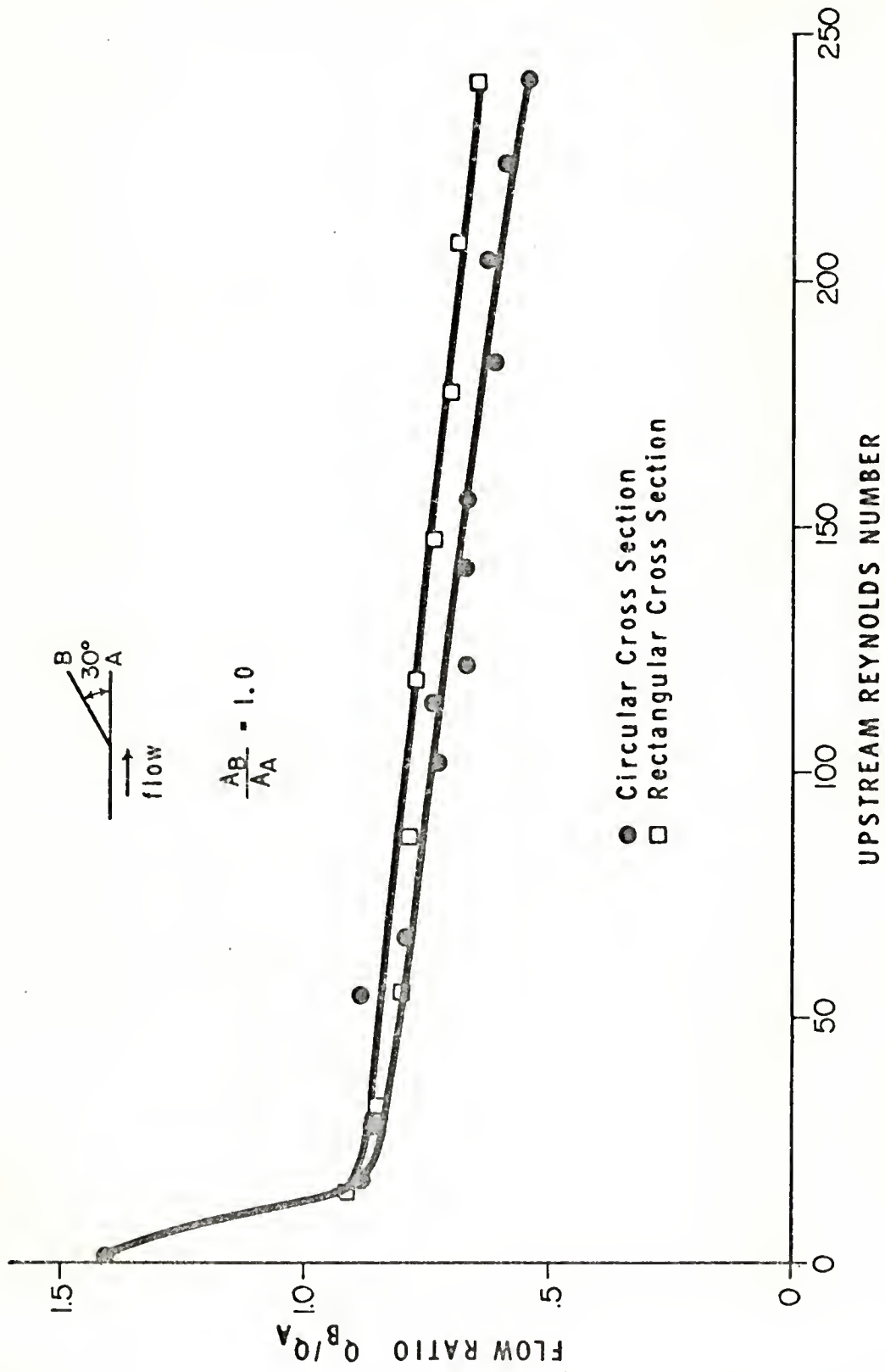


Figure 17. Flow ratio versus upstream Reynolds number for 30° branches of circular and rectangular cross section (area ratios = 1.0). The change in internal geometry appears to have little effect on the flow distribution characteristics of these branches.

rectangular branch do tend to fall slightly higher than those for the circular branch, but this is probably due to the fact that this branch possessed a smoother transition from the upstream segment to the side arm.

Figure 18 shows an isochromatic-band distribution obtained for a low-Reynolds-number flow through a circular  $60^\circ$  branch. The upstream Reynolds number for this experiment was 10, and the wall stress was  $75 \text{ dynes/cm}^2$ . The incident light was circularly polarized.

Unlike the patterns seen at higher Reynolds numbers, this birefringence pattern is characterized by a very smooth and symmetric transition from the upstream segment into the downstream branches. There is no displacement of bands toward the inner walls, and the entrance lengths for each arm are less than two diameters. As mentioned previously, this is typical of the patterns seen in all the branches at very low Reynolds numbers. The lack of band displacement toward the inner walls in Figure 18 together with the symmetrical band distribution indicates that the flow has not yet separated. As the upstream Reynolds number is steadily increased, this pattern becomes more and more distorted with the bands being displaced toward the inner walls such as seen in Figures 12 and 16.

Figure 19 shows the entrance-length data for the  $60^\circ$  branch. The only major difference between these data and those obtained for the  $30^\circ$  branches is that the boundary-layer-separation and secondary-flow phases begin at a Reynolds number of 30 in the  $60^\circ$  branch rather than at 50 as in the  $30^\circ$  branches. The entrance-length data in



Figure 18. Isochromatic-band distribution for steady flow through a 60° branch of circular cross section (area ratio = 1.0). Circularly polarized light,  $Re = 10$ ,  $\tau_w = 75$  dynes/cm<sup>2</sup>. The symmetry of the band distribution and lack of band displacement toward the inner walls indicates that boundary-layer separation has not yet occurred.

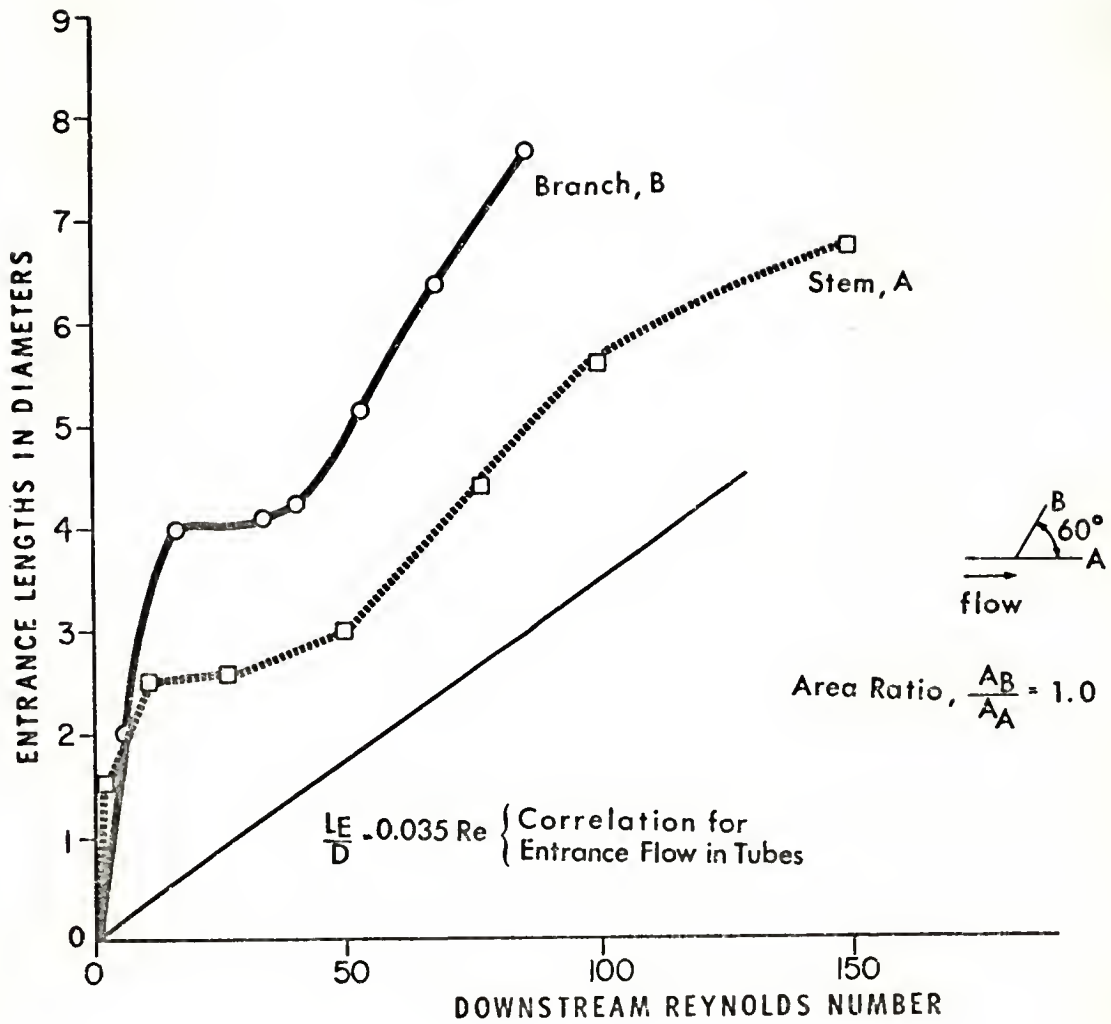


Figure 19. Branch entrance lengths versus downstream Reynolds number for steady flow through a 60° branch of circular cross section (area ratio = 1.0).

length data in Figure 19 show the same three-phase character described for the 30° branch.

Figure 20 shows an isochromatic-band distribution obtained using plane-polarized light for steady flow through a 90° branch of circular cross section. In this experiment, the upstream Reynolds number was 155, the corresponding wall stress 125 dynes/cm<sup>2</sup> and the plane of polarization of the incident light was perpendicular to the main stem of the branch.

This birefringence patterns is also remarkably different from those seen for lower upstream Reynolds numbers. A stagnation point is visible on the outer wall of the side arm directly across from the bifurcation point, and, more importantly, the displacement of bands toward the inner walls shows that localized areas of increased shear occur along both inner walls approximately one diameter downstream from the bifurcation. It should be mentioned that similar areas were also observed at the highest Reynolds numbers in the 60° branch but were not seen in the 30° branches for the Reynolds-number range studied. These observations confirm Fry's speculation<sup>16</sup> regarding sites of locally increased shear in branches.

The shear stress acting on the inner downstream walls at the points of maximum band displacement in Figure 20 can be estimated from Equation (74). However, in Figure 20 the first-order green band adjacent to the inner walls does not extend into the upstream segment, and so the calculation must be based on the displacement of the corresponding first-order



Figure 20. Isochromatic-band distribution for steady flow through a 90° branch of circular cross section (area ratio = 1.0). Plane-polarized light,  $Re = 155$ ,  $\tau_w = 125$  dynes/cm<sup>2</sup>. Increased stress occurs on the inner side-arm wall approximately one diameter downstream from the bifurcation, and flow stagnation occurs along the outer side-arm wall.

green band appearing in the upstream segment. That band has a fractional displacement of  $\beta(\text{up}) = 0.4$ , while the fractional displacement of the downstream band is  $\beta(\text{down}) = 0.85$  for both the main stem and the side arm. The following quantities appearing on the right side of Equation (74) may then be obtained from Table 2:

$$\beta(\text{up}) = 0.4, \quad (1-\beta^2(\text{up}))^{\frac{1}{2}} = 0.917 \text{ and } \phi(\text{up}) = 0.637$$

$$\beta(\text{down}) = 0.85, \quad (1-\beta^2(\text{down}))^{\frac{1}{2}} = 0.527$$

Since the upstream wall stress for this calculation is  $125 \text{ dynes/cm}^2$ , Equation (74) gives

$$\tau(\text{avg, down}) = (0.917/0.527) (0.637) (125) = 139 \text{ dynes/cm}^2,$$

That is, for an upstream Reynolds number of 155, the estimated wall stress at the downstream positions in the  $90^\circ$  branch actually exceeds the upstream wall stress by approximately 11%.

Figure 21 shows the entrance-length data for the  $90^\circ$  branch of Figure 20. Although the side arm of this branch was too short to follow the flow disturbances any farther than four diameters downstream, the data for the main stem do indicate that these disturbances propagate in three phases just as for the  $30^\circ$  and  $60^\circ$  branches. The data for the main stem of the  $90^\circ$  branch show a more pronounced taper at higher Reynolds numbers than do those for the other branches, which indicates

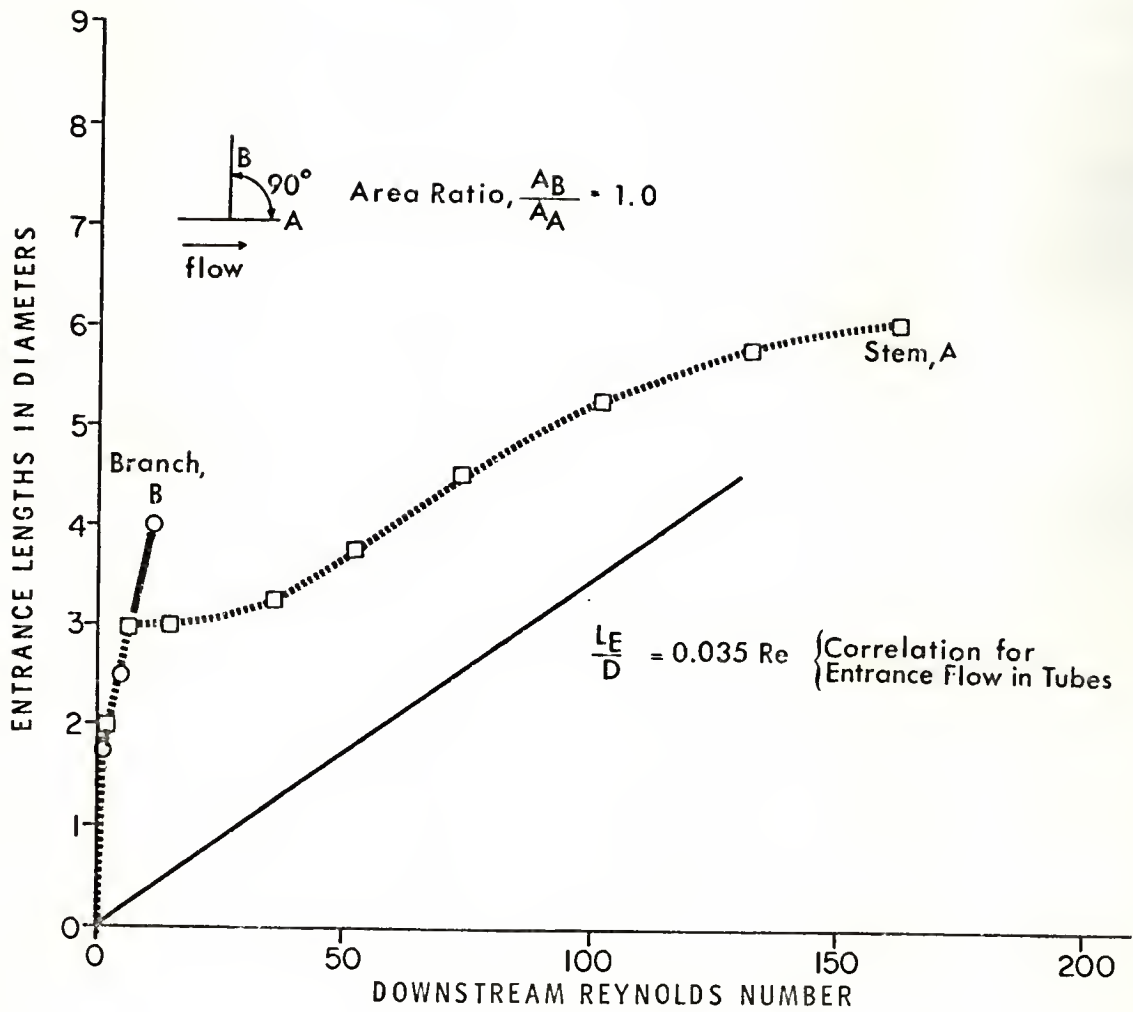


Figure 21. Branch entrance lengths versus downstream Reynolds number for steady flow through a 90° branch of circular cross section (area ratio = 1.0).

that secondary flow in the  $90^\circ$  branch is also more pronounced at higher Reynolds numbers. This secondary flow is characterized by a twisting of the birefringence patterns which can be seen in the corresponding photographs.

Figures 22 and 23 respectively show the band patterns for unseparated and separated flow through a  $\pm 45^\circ$  wye branch of circular cross section. In each of these experiments, the incident light was plane polarized and oriented perpendicular to the downstream stem appearing horizontally in the photographs. The upstream Reynolds number for the unseparated flow of Figure 22 was 10, while that for the separated flow of Figure 23 was 100.

As was the case for the  $60^\circ$  branch shown in Figure 18, the unseparated-flow pattern of Figure 22 is marked by a smooth transition of bands from the upstream segment into the downstream arms, with correspondingly small entrance lengths. On the other hand, the birefringence pattern of Figure 23 exhibits the typical band displacement and twisting indicative of secondary flow, and the flow disturbances persist a number of diameters downstream. The twisting of the birefringence patterns seen in Figure 23 was most pronounced in the  $90^\circ$  and wye branches but was also seen in the  $60^\circ$  branch at the highest Reynolds numbers.

Figure 24 shows the flow-distribution characteristics of all the branches which have been discussed. Here, branching flow ratio has been plotted versus the upstream Reynolds number, with branching angle as a parameter.



Figure 22. Isochromatic-band distribution for steady unseparated flow through a  $\pm 45^\circ$  wye branch of circular cross section (area ratio = 1.0). Plane-polarized light,  $Re = 10$ ,  $\tau_w = 75 \text{ dynes/cm}^2$ . This birefringence pattern shows no evidence of secondary flow.



Figure 23. Isochromatic-band distribution for steady separated flow through a  $+45^\circ$  wye branch of circular cross section (area ratio = 1.0). Plane-polarized light,  $Re = 100$ ,  $\tau_w = 107$  dynes/cm<sup>2</sup>. A twisted birefringence pattern characteristic of secondary flow can be seen in each arm of the branch.

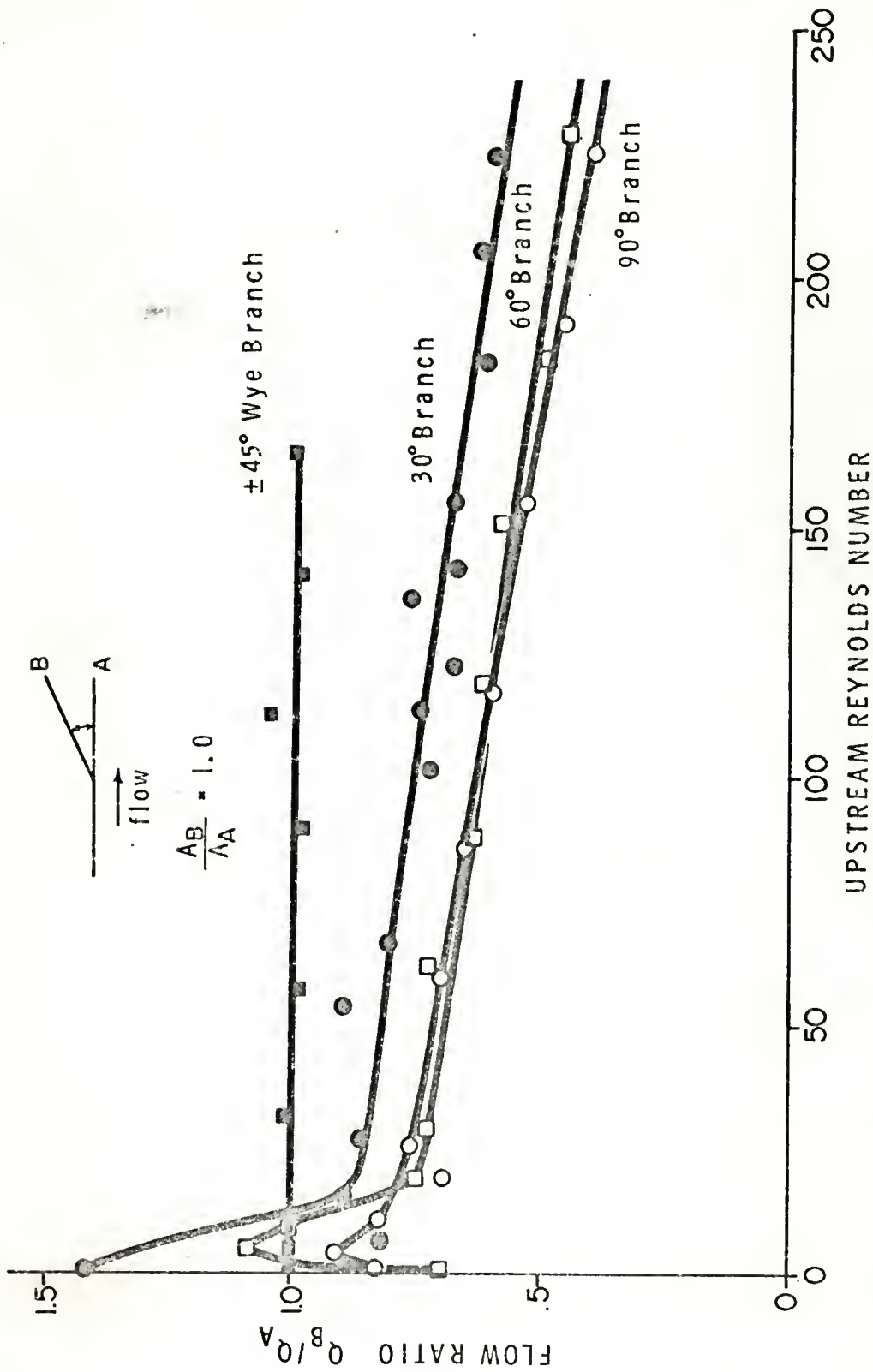


Figure 24. Flow ratio versus upstream Reynolds number, with branching angle as a parameter, for branches of circular cross section (area ratios = 1.0). These data compared with those of Figure 13 indicate that increasing branching angle is not nearly as effective as decreasing area ratio in reducing the flow ratio at a given Reynolds number.

These data show clearly that at any given Reynolds number the flow ratio of single-side-arm branches is only slightly reduced by increases in branching angle. If the data of Figure 24 are compared with those of Figure 13, it is apparent that variations in area ratio produce much greater variations in flow ratio than do variations in branching angle for the same Reynolds number. Figure 24 also shows that in the low-Reynolds-number range, wall attachment can cause the flow ratio to exceed unity even for a 60° branch. This effect was not observed for the 90° branch. In contrast to the single-side-arm branches, the wye branch showed an equal distribution of flow to the downstream arms over the entire Reynolds-number range studied.

Finally, the results of the above experiments suggest that there are two basic physical mechanisms for the initiation of wall trauma and atherosclerotic disease at sites of branching in the arterial system. According to the first mechanism, the formation of atheromatous plaque would be initiated *directly* by a process of deposition from the blood in regions of local flow stasis. According to the second mechanism, atheromatous plaque would be formed *indirectly* through erosion of the arterial intima at points of locally increased shear followed by the fibroblastic proliferation and deposition of mucoid ground substance described by Enos, Beyer and Holmes.<sup>13</sup>

The results of this study and that by Fox and Hugh<sup>14</sup> indicate that if atherosclerosis results from the flow-stasis mechanism, the disease would occur initially along the outer walls of branches. On the

other hand, if wall erosion is responsible for initiating the disease, early plaque deposits would be found along the inner walls.

Although several studies have noted that atherosclerosis shows a general predilection for formation at branches, few attempts have been made to determine those sites where the disease is *initiated*. This is important from a mechanistic point of view, since once deposits are formed, the entire geometric character of the branch is changed. Of those studies reporting on the distributions of early lesions, the great majority concur with the findings of Texon<sup>47</sup> and Texon, Imparato and Lord<sup>49</sup> who have shown experimentally that the point of bifurcation in branches is usually remarkably free of disease, while the medial-crotch zones or inner walls usually show early involvement. Their results suggest that the wall-erosion mechanism is involved.

Further evidence for the shear-stress mechanism is offered by the results of Enos, Beyer and Holmes.<sup>13</sup> Reporting a study of 300 coronary arteries taken from soldiers killed in Korea, they disclosed that the earliest lesions were distributed in spiral fashion and that the medial-crotch walls were involved a short distance downstream from the point of bifurcation. The spiral patterns depicted by them are remarkably similar to the twisted birefringence patterns seen at higher Reynolds numbers in the present study.

The question naturally arises as to whether shear stresses occurring in the cardiovascular system are of sufficient magnitude to erode the vessel walls, even at sites of locally increased shear. Fry<sup>16</sup>

has determined experimentally that a shear stress of  $379 \pm 85(\text{sd})$  dynes/cm<sup>2</sup> is sufficient to erode the arterial wall in dogs with exposures for as little as one hour. However, a similar "critical" value is not available for human arterial tissue.

A rough estimate of the maximum wall stress in any artery can be obtained by neglecting the contribution from time-varying flow and assuming that this stress is given by the maximum value of the quantity  $-(\frac{\partial P}{\partial z}) \frac{R}{2}$ . As an example, consider the calculation for the femoral artery of a dog. McDonald<sup>32</sup> has measured the pressure gradient for this artery, and, according to his data, the typical maximum value of  $-(\frac{\partial P}{\partial z})$  is 3 mm Hg/cm. The typical inside radius for this artery is 0.15 cm. Substitution of these quantities above and converting units gives an estimated maximum wall stress of 300 dynes/cm<sup>2</sup>. Since the stress at points of increased shear would exceed this value, it would appear that at least during part of the cardiac cycle the wall stress at these points would be well within the critical range reported by Fry. From the pathologic data discussed above, it would seem reasonable to say that an analogous situation applies to branches in the human arterial tree.

### C. Pulsatile-Flow Experiments

The purpose of the pulsatile-flow experiments was twofold: First, a comparison was sought between the qualitative results for steady branching flows and those for a type of flow more representative of that in the arterial system. Second, it was desired to investigate the possibility of

using flow birefringence to study quantitatively the propagation of time-varying disturbances.<sup>10</sup>

As mentioned previously, the pump used in these experiments had the output flow wave shown in Figure 4, and experimental data were obtained from frame-by-frame analysis of the motion-picture films.

For each branch studied, no qualitative differences could be found between the pulsatile- and steady-flow birefringence patterns for corresponding upstream flow rates. Typically, as the initial part of the flow pulse entered the test sections, the optical field brightened, and symmetrical band distributions appeared. These were similar to the distributions shown in Figures 18 and 22 for low-Reynolds-number steady flows. Successive frames revealed that the bands were then rapidly displaced toward the inner walls of the branches as regions of flow stasis and boundary-layer separation were evidenced along the outer walls. As was the case for steady flows, the regions of flow stasis appeared directly across the lumen from the point of bifurcation. For those branches having branching angles greater than  $30^\circ$ , the patterns of displaced bands were followed by patterns of twisted bands similar to that shown in Figure 23. Again, this behavior was most pronounced in the  $90^\circ$  and wye branches. The succession of optical phenomena was exactly reversed for the descending portion of the flow pulse.

Significantly, it was found that the points of maximum band displacement did not move with the incoming flow pulse but remained centered approximately one diameter downstream from the point of bifurcation.

The regions of flow stagnation also remained stationary throughout the pulse cycle. There was no evidence to indicate that any disturbances were propagated back upstream.

Figures 25, 26 and 27 summarize the pulsatile-flow entrance-length data for all the branches which have been discussed. In these figures, branch entrance lengths have been plotted versus flow-pulse phase angle (time), and the flow pulse itself (unlabeled dotted curve) has been superimposed on the data as a phase reference. In Figure 25, data for  $30^\circ$  branches of circular cross section are compared, with area ratio as a parameter. In Figure 26, the comparison is among circular branches having an area ratio of unity, with branching angle as a parameter. The data of Figure 27 apply to branches having an area ratio of unity, with internal geometry and type of branch as parameters.

It is apparent from Figures 25 and 26 that area ratio influences the propagation of flow disturbances much more than does branching angle. In particular, Figure 25 shows that when the area ratio was decreased from unity, side-arm entrance length decreased and remained constant over more of the pulse cycle, while that for the main stem increased and tended to follow the input flow wave more closely. On the other hand, Figure 26 shows that when the branching angle was increased, side-arm entrance length decreased only slightly over the pulse cycle, while that for the main stem increased slightly. These observations are consistent with the fact that flow ratio decreases markedly with decreasing area ratio but is relatively insensitive to changes in branching angle.



Flow-Pulse Period = 1.62 sec.  
Main-Stem Diameter = 3.00 mm

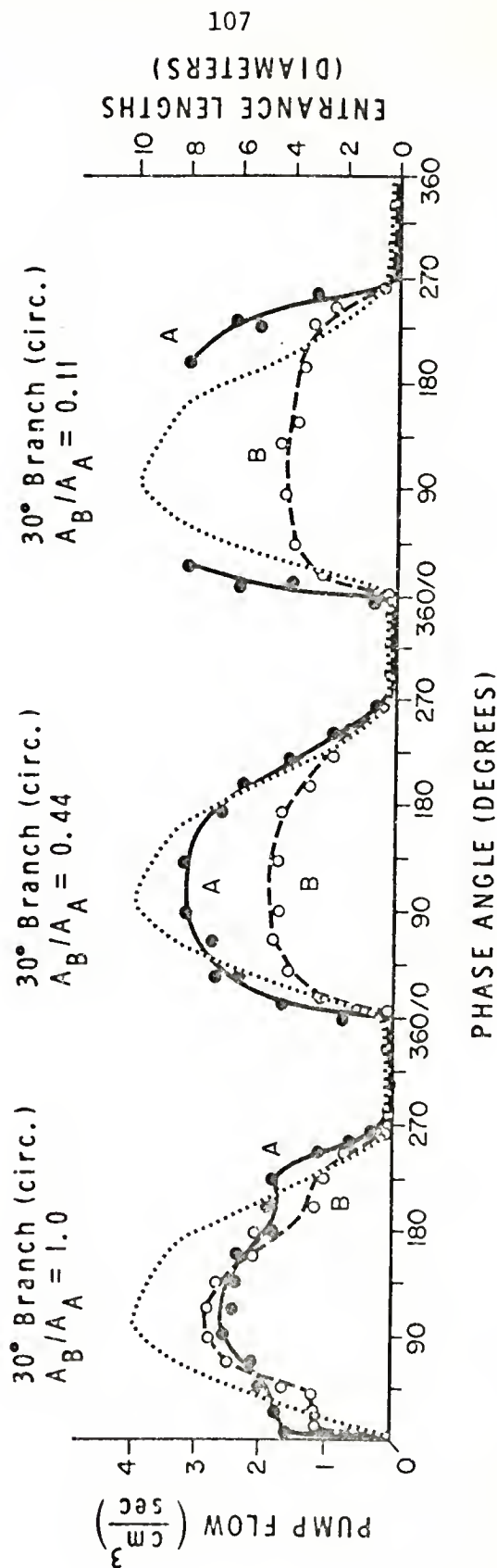


Figure 25. Branch entrance lengths versus flow-pulse phase angle (time), with area ratio as a parameter, for pulsatile flow through 30° branches of circular cross section. As branch area ratio decreases, side-arm entrance length tends to decrease and remain constant over more of the pulse cycle, while that in the main stem increases and tends to follow the input flow wave (unlabeled dotted curve) more closely.

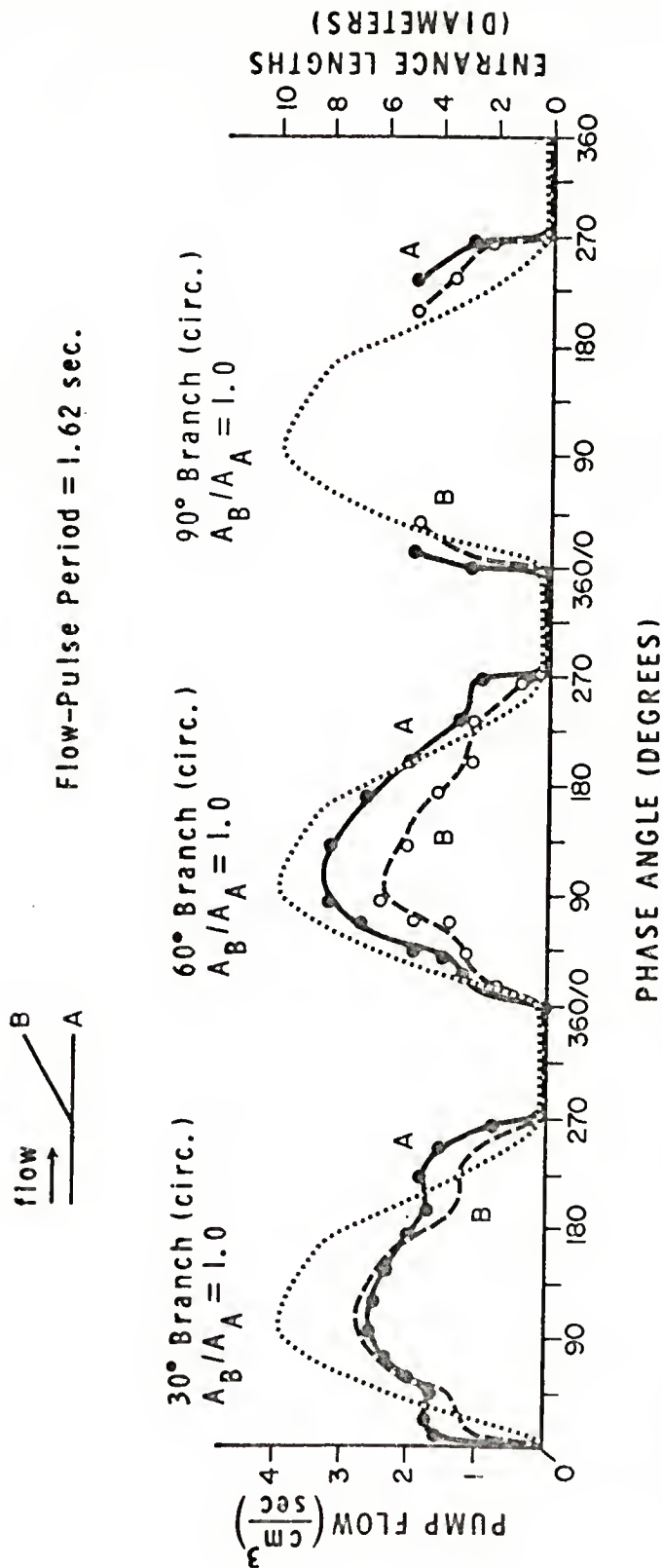


Figure 26. Branch entrance lengths versus flow-pulse phase angle (time), with branching angle as a parameter, for pulsatile flow through branches of circular cross section (area ratios = 1.0). As branching angle increases, side-arm entrance length tends to decrease slightly over the whole pulse cycle, while that for the main stem increases slightly. Again, these changes are not as pronounced as those in Figure 25 where the branch area ratio is varied.

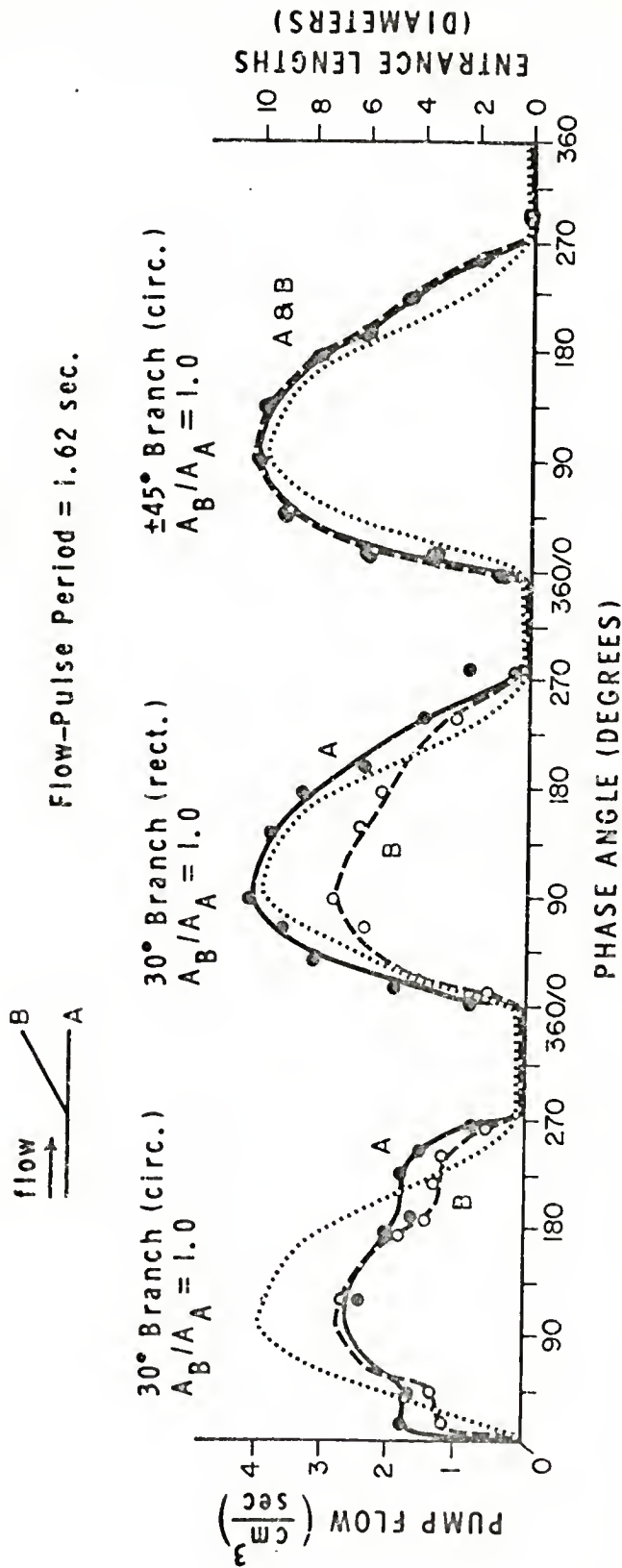


Figure 27. Branch entrance lengths versus flow-pulse phase angle (time), with internal geometry and type of branch as parameters, for pulsatile flow through branches having an area ratio of unity. Though the flow distribution characteristics of the two 30° branches are similar, these data show that disturbances propagate farther in the rectangular branch. Disturbances also propagate farther in the wye branch than they do in branches of the single-side-arm type.

Figure 27 shows that changing the internal branch geometry from a circular to a rectangular cross section increased the entrance lengths for flow disturbances. This could be expected to occur for any branch in which the cross sections of the arms are not angularly symmetric. It is also seen that flow disturbances propagated equal distances in the arms of the wye branch over the whole pulse cycle, and that these disturbances propagated farther than in circular branches of the single-side-arm type. This may be attributed to the fact that secondary flow was more pronounced in the wye branch, particularly at lower flow rates.

## SECTION VI

### CONCLUSIONS AND RECOMMENDATIONS

The technique of flow birefringence has been used to investigate steady and pulsatile flows through several model branches simulating those of the arterial system. Qualitative and quantitative results concerning both the initiation and propagation of branching-flow disturbances and the local distribution of shearing stress for such flows have been presented. In addition, flow-distribution data for steady branching flows have been discussed.

The results of this study support the following conclusions:

1. Regions of locally increased shear, where stresses can exceed the upstream wall stress, occur along the inner walls of single-side-arm branches when the following conditions are met: 1. the upstream Reynolds number exceeds 150, 2. the branching angle is greater than  $30^\circ$  and 3. the downstream arms of the branch are of approximately the same diameter. When the flow is pulsatile, these regions do not move with the pulse but remain centered approximately one diameter downstream from the point of bifurcation. These conclusions are supported by photographic evidence showing marked lateral displacement of isochromatic bands and by calculations based on flow-birefringence theory.

2. Regions of local flow stasis and boundary-layer separation occur along the outer walls of single-side-arm branches for upstream Reynolds numbers between 20 and 50 depending on the branching angle. When the flow is pulsatile, these regions do not move with the pulse but remain centered directly across the lumen from the point of bifurcation. These conclusions are supported by photographic evidence showing stagnation points characterized by concave distributions of isochromatic bands.
3. On the basis of conclusions 1 and 2 above and from data reported in the medical literature,<sup>13,17,22,47,48,49,50,54,55</sup> it is concluded that locally increased shear stress on the arterial intima at sites of branching represents the most probable physical mechanism for initiating the wall trauma associated with atherosclerotic disease. This contention is supported by the fact that the maximum wall stress estimated from McDonald's pressure-gradient data<sup>32</sup> for the femoral artery of a dog falls within the "critical" range reported by Fry.<sup>16</sup>
4. Flow birefringence is a convenient and useful technique for studying the initiation and propagation of flow disturbances in any geometry. Experiments with flows around needles and through branches have shown that flow disturbances can be characterized by entrance lengths based on distorted birefringence patterns. In particular, it has been shown that needles mounted flush

- with the inner wall of a tube create no disturbance to flow.
5. As the upstream Reynolds number is increased from zero, flow disturbances in branches are generated and propagated by three processes: 1. the readjustment of the initial laminar velocity profile, 2. the onset of boundary-layer separation and 3. the onset of secondary flow. This conclusion is supported by entrance-length data for both steady and pulsatile flows.
  6. For a given fluid and geometric configuration, the flow distribution in branches is determined dynamically by upstream fluid momentum per unit volume and not by upstream Reynolds number. Geometrically, the branch area ratio is a much more significant parameter than is branching angle. These conclusions are supported by experiments with Milling-Yellow dye and water in the upstream-Reynolds-number range from 0 to 2100.
  7. Wall attachment of flow occurs in branches of the single-side-arm type to the extent that side-arm flow will exceed that in the main downstream stem providing that 1. the upstream Reynolds number is below a certain value which is dependent on the fluid, 2. the branching angle is less than  $60^\circ$  and 3. the downstream arms of the branch are of approximately the same diameter.

Several recommendations can be made on the basis of the above results and conclusions. In particular:

1. The effect of artificially changing the pressure pulse *in vivo* upon the incidence and distribution of atherosclerotic lesions should be investigated thoroughly. Specifically, if the shear-stress mechanism is responsible for initiating this disease, it would be expected that drugs effecting reductions in pressure gradient while maintaining the same net flow would reduce both the peak wall stress and the incidence of atherosclerotic lesions at branches in the arterial system.
2. The use of micro probes employing heated thermistors, such as that developed by Ling and Atabek,<sup>29</sup> should be investigated for measuring velocity gradients near the walls of branches. Such measurements could provide an independent check on the presence of locally increased shear stress and could be made *in vivo*.
3. The measurement of pressure distributions for branching flows would be a logical extension of the present study. Such experiments should include the measurement of angular pressure variations as well as axial variations. These results would be of particular importance in the field of fluidics.
4. Further studies of the fluid dynamics of branching should incorporate digital computation of the pressure and velocity distributions for both two-dimensional and three-dimensional branching flows. The results of such computations could not only be compared with the flow-distribution data of the present study but would provide greater insight into the

problem of branching flows in general. The Marker and Cell technique developed by Welch, Harlow, Shannon and Daly<sup>53</sup> is ideally suited for this purpose.

5. Both theoretical and experimental studies of flow birefringence should be continued. At the present time, laser light appears to offer the most promising investigative tool for such studies.

## APPENDICES

## APPENDIX A

### THE STEWART-HAMILTON TECHNIQUE

In this section we present a brief discussion of the Stewart-Hamilton indicator-dilution technique<sup>19,57</sup> and derive the commonly used working equation for determining cardiac output by this technique. We demonstrate that this equation applies only to a sampling catheter under three conditions; namely that the indicator used is well mixed with the blood between injection and sampling sites, that blood withdrawal rate through the sampling catheter is constant and that recirculation is eliminated. The first assumption bears a direct relation to results of the present study regarding secondary flow at branches. The second assumption, though implied in the literature, is seldom stated; and so a distinction is made here between the more general equation including variable withdrawal and the special case used in practice.

Consider a system of branching tubes stemming initially from some source trunk such as indicated in Figure 28 below. The object of the Stewart-Hamilton technique is to determine the flow rate at point A (the source) by rapidly injecting a known quantity of indicator (say indocyanine-green dye) at this point and then sampling the concentration of this indicator as a function of time at an *arbitrary* point i downstream. It is shown below that the time integral of this function may be used to evaluate the flow rate at point A. We wish to determine those conditions under which such a measurement accurately reflects the

flow rate at point A.

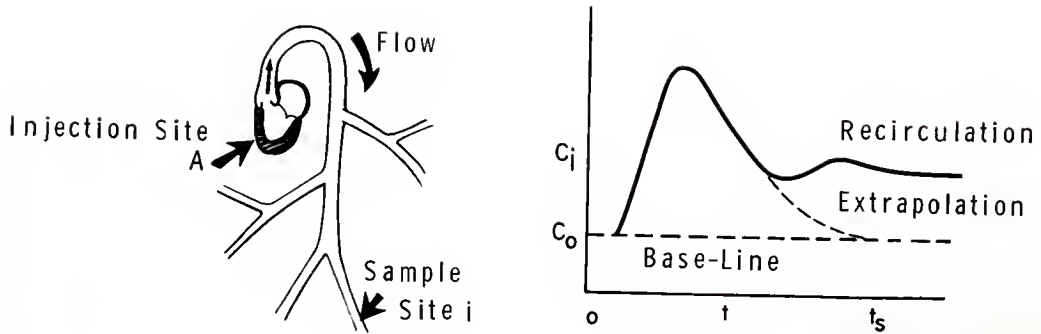


Figure 28. The Stewart-Hamilton experiment, illustrating a typical indicator-dilution curve. Indicator is injected at point A and sampled at point i. Indicator concentration at point i as a function of time is shown as the solid curve at the right.

In practice, indicator is injected and sampled using cardiac catheters, and point A, the injection site, is located in or near the heart. This assures that the resulting flow calculation is a reflection of cardiac output as opposed, for instance, to flow in a major artery.

There are some complications resulting from the fact that the cardiovascular system is a closed-loop system. First, since several injections may be made during the course of a single cardiac-catheterization procedure, account must be made for the presence of any indicator

due to previous injections. This indicator is reflected in the base-line concentration level  $C_0$  shown in the figure. The situation is further complicated by the fact that commonly used indicators are degraded by certain organs of the body and consequently exhibit a half-life. This half-life, approximately twenty minutes, is considerably greater than the sampling time  $t_s$ , which is of the order of twenty seconds; so the associated base-line shifting does not lead to appreciable error in cardiac-output calculations. Secondly, typical indicator-dilution curves, such as that pictured in the figure, exhibit a recirculation hump owing to indicator having traversed the loop and making a second pass. Thus, for accurate results, these curves must be extrapolated in such a way as to disallow any contribution from recirculation. An exponential extrapolation is a common and accurate way of doing this.

Fortunately, these complications can be easily accounted for during an actual procedure; and, in fact, an analog-computer program has been developed<sup>26</sup> which automatically does this as well as providing immediate cardiac outputs.

Referring again to Figure 28, we now wish to derive the working equation of the Stewart-Hamilton technique and to consider the assumptions involved in obtaining this relation.

It is assumed in this derivation that indicator concentration at point  $i$  is measured along the extrapolated dilution curve. This is tantamount to assuming that injected indicator passing point  $i$  makes only a single pass, or that recirculation has been eliminated.

Let us now assume that a known amount of indicator (say A mg) is rapidly injected at point A. This indicator simultaneously mixes with the blood flowing past point A, diffuses and is convected downstream. Since axial diffusion is negligible compared to axial convection, the amount of indicator which passes any arbitrary downstream point  $i$  in the time interval  $dt$  may be expressed as

$$dA_i = Q_i C_i dt \quad (A1)$$

where:  $Q_i$  = volumetric flow rate at point  $i$ , (l/sec)  
 $C_i$  = indicator concentration at point  $i$ , (mg/l)

If time is measured starting with the injection at time zero, then the total amount of indicator which passes point  $i$  from  $t = 0$  to  $t = t_s$  is

$$A_i = \int_0^{t_s} Q_i C_i dt \quad (A2)$$

where the sampling time  $t_s$  is sufficiently great to allow all indicator pursuing this particular route to pass point  $i$ . It should be mentioned that an equation analogous to Equation (A2) has been given previously by Cropp and Burton.<sup>12</sup> However, their expression replaces the left side of Equation (A2) with the total amount of indicator injected and is therefore only applicable to a non-branching system. They did not discuss a branched system, which is clearly of much more interest.

We now make the first major assumption. It is assumed that the indicator injected at point A becomes well mixed over the imaginary

surface perpendicular to the flow streamlines at this point and subsequently remains well mixed over all such surfaces throughout the flow field between injection and sampling sites. This is to say that over any surface in the flow field which is everywhere perpendicular to the flow streamlines, indicator concentration depends only on time and not on position. In particular, this assumption is meant to apply at branches. For the special case of parallel flow in a circular tube, this is equivalent to neglecting any angular or radial concentration gradients but not axial ones.

The above assumption might be justified in practice due to a combination of factors such as mixing produced in the ventricles of the heart, secondary flow at branches and a resultant "flat" velocity profile due to the pulsatile nature of the flow. At best, however, it represents an approximation. A study by Bassingthwaighe, Edwards and Wood<sup>6</sup> has shown that there is good agreement between cardiac outputs determined simultaneously from central and peripheral sites in dogs. Their results lend support to the assumption of well-mixed indicator, but only for the larger vessels.

Note that axial concentration gradients still exist in the cardiovascular system, as is evident from the nature of a typical dilution curve; thus, the assumption of well-mixed indicator is meant *only* in the sense discussed above. This point has not been clearly made in the literature.

Since the assumption of well-mixed indicator infers that indicator

injected at point A uniformly tags the blood over the above-mentioned imaginary surfaces from this point on, it is implied that the total amount of indicator entering any downstream branch from  $t = 0$  to  $t = t_s$  is directly proportional to the fraction of the total flow past A which enters that branch in the same interval. Stating this mathematically, the assumption of well-mixed indicator implies the following:

$$A_e = K \frac{\int_0^{t_s} Q_i dt}{\int_0^{t_s} Q_A dt} \quad (A3)$$

where:  $A_e$  = total amount of indicator (mg) which enters the downstream branch in which point i is located in the time interval from  $t = 0$  to  $t = t_s$

$K$  = constant of proportionality

$Q_i$  = volumetric flow rate at point i, ( l/sec.)

$Q_A$  = volumetric flow rate at point A, ( l/sec )

To evaluate the constant of proportionality  $K$ , let the experiment be conducted in an unbranched tube. For this case,  $Q_i = Q_A$  and  $A_e = A$ , the total amount of indicator injected. Thus, the proportionality constant is equal to  $A$ , and the total amount of indicator entering the arbitrary downstream branch becomes

$$A_e = A \frac{\int_0^{t_s} Q_i dt}{\int_0^{t_s} Q_A dt} \quad (A4)$$

Since there is no net accumulation of indicator in this arbitrary branch, one may set the total amount of indicator which enters according to Equation (A4) equal to the total amount which passes point  $i$  according to Equation (A2) to obtain

$$A \frac{\int_0^{t_s} Q_i dt}{\int_0^{t_s} Q_A dt} = \int_0^{t_s} Q_i C_i dt \quad (A5)$$

If one defines an integral mean of the quantity  $Q$  as

$$Q(\text{mean}) = \frac{\int_0^t Q(t) dt}{\int_0^t dt} \quad (A6)$$

then the left side of Equation (A5) can be rewritten in terms of mean flow rates for the interval  $t = 0$  to  $t = t_s$  by dividing numerator and denominator by  $t_s$ . Thus,

$$A \frac{Q_i(\text{mean})}{Q_A(\text{mean})} = \int_0^{t_s} Q_i C_i dt \quad (A7)$$

Since the quantity of interest in the Stewart-Hamilton experiment is  $Q_A(\text{mean})$ , we solve Equation (A7) to obtain

$$Q_A(\text{mean}) = \frac{A Q_i(\text{mean})}{\int_0^{t_s} Q_i C_i dt} \quad (A8)$$

This is a general form of the Stewart-Hamilton working equation for determining cardiac output, and it applies for time-varying flow and concentration at *any* downstream sampling site. The assumptions involved in this expression are well-mixed indicator in the sense discussed previously and the absence of recirculation.

It is evident that to apply Equation (A8) rigorously to a downstream site (such as the femoral artery) one would need to know not only concentration  $C_i$  but also flow rate  $Q_i$  as functions of time at this site. Unfortunately, this information is generally unavailable from catheterization data; and, in fact, since concentration is always measured externally by withdrawing blood through a sampling catheter and transducer, neither concentration nor flow rate is actually measured at point  $i$ .

This apparent difficulty may be overcome in the following way: Since Equation (A8) applies to any downstream sampling site, it may be taken to apply in particular at the transducer site in the withdrawal catheter where concentration actually is measured. If Equation (A8) is applied in this way, then flow rate  $Q_i$  becomes the blood withdrawal rate through the sampling catheter, which may be controlled externally, and  $C_i$  is the properly scaled output of the transducer. In particular, if blood is withdrawn at a *constant* rate, then  $Q_i$  is constant and identically equal to  $Q_i(\text{mean})$ . The resulting simplification of Equation (A8) gives the working equation for determining cardiac output as it is usually employed. That is

$$Q_A(\text{mean}) = \frac{A}{\int_0^{t_s} C_i dt} \quad (\text{A9})$$

It is important to note that Equation (A9) applies to the withdrawal catheter and is only valid for constant withdrawal rate, in addition to being subject to the assumptions of well-mixed indicator and no recirculation. If withdrawal rate is not constant or if flow and concentration measurements actually are made at a point  $i$  in the cardiovascular system, then the more general equation (A8) must be used.

# APPENDIX B

## Table 3

APPARENT-VISCOSITY AND REYNOLDS-NUMBER DATA  
FOR 1.4% MILLING-YELLOW DYE

$$\tau_w = \frac{\Delta PR}{2L} \quad \mu_{app} = \frac{\pi \Delta PR^4}{8QL} \quad Re = \frac{D \bar{v} \rho}{\mu_{app}}$$

$Q(\text{cm}^3/\text{sec})$	$\tau_w$ (dynes/cm <sup>2</sup> )	$\mu_{app}$ (gm/cm sec)	Re
0.0	0.0	--	0.0
1.02	77.0	0.20	21.7
1.495	84.6	0.15	42.4
2.21	100.0	0.12	78.3
3.06	115.4	0.10	130
3.78	125.0	0.0875	184
5.30	150	0.075	300

# APPENDIX C

Table 4

## PHOTOGRAPHIC DATA\*

Figure Number	Test Section	Light Intensity	Diaphragm Setting	Extension Tube (mm)	Film Plane-Object (mm)	Depth of Field (mm)	Framing Speed
7	1	250	f/4.0	10	123	2.5	16
10	1	400	f/5.6	10	123	3.5	16
11	1	400	f/8.0	10	123	4.5	16
12	6	400	f/5.6	5	180	11.0	16
16	7	400	f/5.6	5	180	11.0	16
18	9	400	f/5.6	5	180	11.0	16
20	10	400	f/5.6	10	123	3.5	16
22	11	400	f/5.6	5	180	11.0	16
23	11	400	f/5.6	5	180	11.0	16

\*NOTES: a. Light intensity was measured between the test section and the analyzer using a Weston light meter (model 745).

b. The focal length of the lens used was 25 mm.

c. The ASA rating (exposure index) for Ektachrome film (type ER-B) is 125.

d. The camera shutter speed at 16 frames/sec was 1/40 sec and at 64 frames/sec was 1/60 sec

e. Pulsatile flows were photographed at 64 frames/sec and f/4.0 using a light intensity of 400.

## BIBLIOGRAPHY

1. Acrivos, A., Babcock, B.D. and Pigford, R.L., Flow distributions in manifolds. *Chemical Engineering Science* 10: 112-124, 1959.
2. Atabek, H.B., End effects. Chapter 10 In: *Pulsatile Blood Flow*. E. O. Attinger, Editor. New York, New York, McGraw-Hill Book Company, Inc., 201-220, 1964.
3. Attinger, E. O., Flow patterns and vascular geometry. Chapter 9 In: *Pulsatile Blood Flow*. E. O. Attinger, Editor. New York, New York, McGraw-Hill Book Company, Inc., 179-200, 1964.
4. \_\_\_\_\_, Sugawara, H., Navarro, A. and Anne, A., Pulsatile flow patterns in distensible tubes. *Circulation Research* 18: 447-456, 1966.
5. Barnett, C.H. and Cochrane, W., Flow of viscous liquids in branched tubes with reference to the hepatic portal vein. *Nature* 177: 740-742, 1956.
6. Bassingthwaite, J.B., Edwards, A.W.T., and Wood, E.H., Areas of dye-dilution curves sampled simultaneously from central and peripheral sites. *Journal of Applied Physiology* 17: 91-98, 1962.
7. Bird, R.B., The equations of change and the macroscopic mass, momentum, and energy balances. *Chemical Engineering Science* 6: 123-131, 1957.
8. \_\_\_\_\_, Stewart, W.E. and Lightfoot, E.N., *Transport Phenomena*. New York, New York, John Wiley & Sons, Inc., 1960.
9. Cerf, R. and Scheraga, H.A., Flow birefringence in solutions of macromolecules. *Chemical Reviews* 51: 185-261, 1952.
10. Chang, C.C. and Atabek, H.B., The inlet length for oscillatory flow and its effects on the determination of the rate of flow in arteries. *Physics in Medicine and Biology* 6: 303-317, 1961.
11. Copher, G.H. and Dick, B.M., "Stream line" phenomena in portal vein and selective distribution of portal blood in liver. *Archives of Surgery* 17: 408-419, 1928.
12. Cropp, G.J.A. and Burton, A.C., Theoretical considerations and model experiments on the validity of indicator dilution methods for measurements of variable flow. *Circulation Research* 18: 26-48, 1966.

13. Enos, W.F., Jr., Beyer, J.C. and Holmes, R.H., Pathogenesis of coronary disease in American soldiers killed in Korea. *Journal of the American Medical Association* 158: 912-914, 1955.
14. Fox, J.A. and Hugh, A.E., Localization of atheroma: A theory based on boundary layer separation. *British Heart Journal* 28: 388-399, 1966.
15. Frank, O., Die theorie der pulswellen. *Zeitschrift Fur Biologie* 85: 91-130, 1926.
16. Fry, D.L., Acute vascular endothelial changes associated with increased blood velocity gradients. *Circulation Research* 22: 165-197, 1968.
17. Geiringer, E., Intimal vascularization and atherosclerosis. *Journal of Pathology and Bacteriology* 63: 201-211, 1951.
18. Hahn, P.F., Donald, W.D. and Grier, R.C., Jr., The physiologic bilaterality of the portal circulation. *American Journal of Physiology* 143: 105-107, 1945.
19. Hamilton, W.F., Measurement of the cardiac output. Chapter 17 In: *Handbook of Physiology*. Volume I, Section 2, *Circulation*. W.F. Hamilton and P. Dow, Editors. Washington, D.C., American Physiological Society, 551-584, 1962.
20. Helps, E.P.W. and McDonald, D.A., Observations on laminar flow in veins. *Journal of Physiology* 124: 631-639, 1954.
21. \_\_\_\_\_ and \_\_\_\_\_, Streamline flow in veins. *Journal of Physiology* 126: 50-60, 1954.
22. Imparato, A.M., Lord, J.W., Jr., Texon, M. and Helpert, M., Experimental atherosclerosis produced by alterations of blood vessel configuration. *Surgical Forum* 12: 245-247, 1961.
23. Jerrard, H.G., Theories of streaming double refraction. *Chemical Reviews* 59: 345-428, 1959.
24. Knox, C.K., Jr., An experimental investigation of the steady flow of a viscous fluid in circular, branched tubes. M.S. Thesis. Minneapolis, Minnesota, University of Minnesota, 1962.
25. Krovetz, L.J., Crowe, W.J. and Santi, K., Effects of vessel branching on fluid flow. Silent Motion Picture Presented at the 7th International Conference on Medical and Biological Engineering. Stockholm, Sweden, 1967. (Available upon request from the author)

26. \_\_\_\_\_, \_\_\_\_\_, Fairchild, B.T., Gumbar, P.A. and Mitchell, M.B., Automated computation of cardiac output from indicator-dilution curves. Unpublished Paper.
27. \_\_\_\_\_, The effect of vessel branching on fluid flow. Ph.D. Thesis. Minneapolis, Minnesota, University of Minnesota, 1963.
28. \_\_\_\_\_, The effect of vessel branching on haemodynamic stability. *Physics in Medicine and Biology* 10: 417-427, 1965.
29. Ling, S.C. and Atabek, H.B., Measurement of aortic blood flow in dogs by the hot-film technique. Abstract In: *Proceedings of the (19th) Annual Conference on Engineering in Medicine and Biology* 8: 113, 1966. (Available from Institute of Electrical and Electronics Engineers, 345 East 47th Street, New York, New York, 10017)
30. Mach, M.E., *Optisch-Akustische Versuche*. Prague, Czechoslovakia, Calve, 1873.
31. Maxwell, J.C., On double refraction in a viscous fluid in motion. *Proceedings of the Royal Society of London* 22: 46-47, 1873.
32. McDonald, D.A., *Blood Flow in Arteries*. Baltimore, Maryland, Williams & Wilkins, 1960.
33. \_\_\_\_\_, The occurrence of turbulent flow in the rabbit aorta. *Journal of Physiology* 118: 340-347, 1952.
34. Moens, A.I., *Die Pulscurve*. Leiden, Netherlands, E.J. Brill, 1878.
35. Neumaster, T. and Krovetz, L.J., A method for producing transparent models of blood vessels. *Journal of Applied Physiology* 19: 1184-1186, 1964.
36. Peebles, F.N., Garber, H.J. and Jury, S.H., Preliminary studies of flow phenomena utilizing a doubly refracting liquid. In: *Proceedings of the Third Midwestern Conference on Fluid Mechanics*. Minneapolis, Minnesota, University of Minnesota Press, 441-454, 1953.
37. \_\_\_\_\_, Prados, J.W. and Honeycutt, E.H., Jr., Birefringent and rheologic properties of milling yellow suspensions. *Journal of Polymer Science: Part C, Polymer Symposia*, Number 5, *Rheo-optics of Polymers*, 37-53, 1964.

38. Peterlin, A. and Stuart, H.A., Über die bestimmung der größe und form, sowie der elektrischen, optischen und magnetischen anisotropie von submikroskopischen teilchen mit hilfe der künstlichen doppelbrechung und der inneren reibung. *Zeitschrift für Physik* 112: 129-147, 1939.
39. Poisson, S.D., Mémoire sur le mouvement des fluides élastiques dans les tuyaux cylindriques, et sur la theorie des instruments á vent. *Paris Academy of Sciences Memoirs*. Title II, 305-402, 1819.
40. Prados, J.W. and Peebles, F.N., Two-dimensional laminar-flow analysis, utilizing a doubly refracting liquid. *American Institute of Chemical Engineers Journal* 5: 225-234, 1959.
41. \_\_\_\_\_, The analysis of two-dimensional laminar flow utilizing a doubly refracting liquid. Ph.D. Thesis. Knoxville, Tennessee, University of Tennessee, 1957.
42. Rodbard, S., Blood velocity and endocarditis. *Circulation* 27: 18-28, 1963.
43. Rosenberg, B., The use of doubly refracting solutions in the investigation of fluid flow phenomena. Navy Department, David W. Taylor Model Basin, Report 617. Washington, D.C., 1952.
44. Schlichting, H., *Boundary-layer Theory*. Sixth Edition. Translated by J. Kestin. New York, New York, McGraw-Hill Book Company, Inc., 1968.
45. Stehbens, W.E., Turbulence of blood flow. *Quarterly Journal of Experimental Physiology* 44: 110-117, 1959.
46. Strutt, J.W. (Baron Rayleigh), *The Theory of Sound*. Volume 2, Second Edition. New York, New York, Dover Publications, 1945.
47. Texon, M., A hemodynamic concept of atherosclerosis, with particular reference to coronary occlusion. *Archives of Internal Medicine* 99: 418-427, 1957.
48. \_\_\_\_\_, Imparato, A.M. and Helpern, M., The role of vascular dynamics in the development of atherosclerosis. *Journal of the American Medical Association* 194: 1226-1230, 1965.
49. \_\_\_\_\_, \_\_\_\_\_ and Lord, J.W., Jr., The hemodynamic concept of atherosclerosis: The experimental production of hemodynamic arterial disease. *Archives of Surgery* 80: 47-53, 1960.

50. \_\_\_\_\_, \_\_\_\_\_, \_\_\_\_\_ and Helpert, M., Experimental production of arterial lesions. *Archives of Internal Medicine* 110: 50-52, 1962.
51. Wayland, H., Streaming birefringence in hemorrheology. *Bibliotheca Anatomica* 4: 94-101, 1964.
52. Weidner, R.T. and Sells, R.L., *Elementary Classical Physics*. Volume 2. Boston, Massachusetts, Allyn and Bacon, Inc., 1965.
53. Welch, J.E., Harlow, F.H., Shannon, J.B. and Daly, B.J., The mac method: A computing technique for solving viscous, incompressible, transient fluid-flow problems involving free surfaces. U.S. Atomic Energy Commission, Los Alamos Scientific Laboratory, Report LA-3425. Los Alamos, New Mexico, 1966.
54. Wesolowski, S.A., Fries, C.C., Sabini, A.M. and Sawyer, P.N., The significance of turbulence in hemic systems and in the distribution of the atherosclerotic lesion. *Surgery* 57: 155-162, 1965.
55. Wilens, S.L., The experimental production of lipid deposition in excised arteries. *Science* 114: 389-393, 1951.
56. Womersley, J.R., An elastic tube theory of pulse transmission and oscillatory flow in mammalian arteries. U.S. Air Force, Wright Air Development Center, Technical Report TR 56-614. Dayton, Ohio, 1957.
57. Zierler, D.L., Circulation times and the theory of indicator-dilution methods for determining blood flow and volume. Chapter 18 In: *Handbook of Physiology*, Volume I, Section 2, *Circulation*. W. F. Hamilton and P. Dow, Editors. Washington, D.C., American Physiological Society, 585-615, 1962.

## BIOGRAPHICAL SKETCH

William Joseph Crowe, Jr., was born February 28, 1941, in Hartford, Connecticut. He presently resides in Gainesville, Florida, and is married to the former Doreen Ytreoy of Brooklyn, New York.

He attended primary and secondary schools in West Hartford, Connecticut, and received a diploma from Frederick U. Conard High School in June, 1959. In September, 1959, he enrolled at the University of Connecticut at Storrs, where he majored in chemical engineering and graduated in June, 1963, with the degree of Bachelor of Science in Engineering. In September, 1963, he enrolled at the Iowa State University of Science and Technology at Ames and received the degree of Master of Science in August, 1964, with a major in chemical engineering and a minor in nuclear engineering. He enrolled at the University of Florida at Gainesville in September, 1964, and has pursued the Doctor of Philosophy degree since that time with a major in chemical engineering and a minor in mathematics.

Mr. Crowe has held various academic financial awards including a Frank Gannett Newspaperboy Scholarship (1959-1963), Research Assistantship (1963-1964), Engineering College Fellowship (1964-1965), and a National Science Foundation Traineeship (1965-1968).

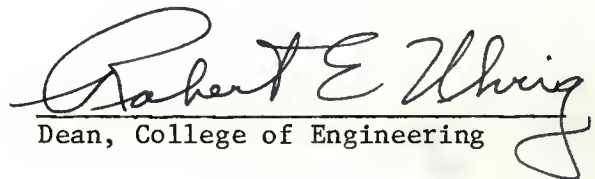
His employment experience includes four summers (1959-1962) as an engineering aide with Alfred Kaehrle Associates, consulting engineers of West Hartford, Connecticut, and one summer (1963) as a technical

exchange student with Van Gelder Zonen Paper Works in Velsen Noord, Netherlands. He has accepted permanent employment in Phoenix, Arizona, with Motorola, Inc., as a Senior Scientist in the Applied Science Department, Semiconductor Products Division.

He is a member of the Honor Society of Phi Kappa Phi and a student member of the American Institute of Chemical Engineers.

This dissertation was prepared under the direction of the chairman of the candidate's supervisory committee and has been approved by all members of that committee. It was submitted to the Dean of the College of Engineering and to the Graduate Council, and was approved as partial fulfillment of the requirements for the degree of Doctor of Philosophy.

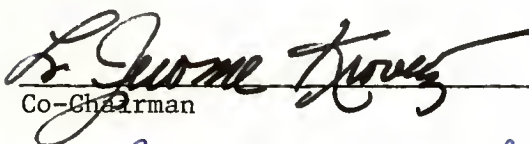
March, 1969

  
Dean, College of Engineering

\_\_\_\_\_  
Dean, Graduate School

Supervisory Committee:

  
Chairman

  
Co-Chairman

